The Effect of Flow Field Design on the Degradation Mechanisms and Long Term Stability of HT-PEM Fuel Cell

Vamsikrishna Bandlamudi

Department of Chemistry

University of the Western Cape

A dissertation submitted to The University of the Western Cape in accordance with the requirements for the degree of Doctor of Philosophy (Ph.D.) in the Department of Chemistry

November 2018

Title: The effect of flow field design on the degradation mechanisms and long term stability of HT-PEM fuel cell

Ph.D. Student: Vamsikrishna Bandlamudi

Supervisor: Sivakumar Pasupathi

Co-supervisor: Piotr Bujlo

Abstract

Fuel cells are long term solution for global energy needs. In current fuel cell technologies, Proton Exchange Membrane (PEM) fuel cells are known for quick start-up and ease of operation compared to other types of fuel cells. Operating PEM fuel cells at high temperature show promising applications for stationary combined heat and power application (CHP). The high operating temperature up to 160°C allows waste heat to be recovered for co-generation or tri-generation purposes. The commercially available PEM fuel cells operating at 160°C can tolerate up to 3% CO without significant loss of performance, making HT-PEM fuel cell viable choice when reformate is used. In reality these advantages convert to very little balance-of-plant compared to Nafion® based fuel cells operating at 60°C.

However, there are some problems that prevent high temperature fuel cells from large scale commercialization. The cathode is said to have sluggish reaction kinetics and high cell potentials and operating temperature during fuel cell start-up may cause severe degradation. The formation of liquid water during the shut-down can cause the phosphoric acid to leach from the cell during operation. Efforts are being made to reduce the cost and increase the durability of fuel cell components (such as catalyst and membrane) at high temperatures. Apart from degradation issues, the problems are related to cost and performance. The performance of the PEM fuel cells depends on a lot of factors such as fuel cell design and assembly, operating conditions and the flow field design used on the cathode and anode plates. The flow field geometry is one important factor influencing the performance of fuel cells. The flow fields have significant effect on pressure and flow distribution inside the fuel cell. A homogeneous distribution of the reactant gases over the active catalyst surface leads to improved electrochemical reactions and thus enhances the performance of the fuel cell. So, the design of flow fields is one of the important issues for performance improvement of PEM fuel cell in terms of power density and efficiency. There are different types of flow fields available for PEM fuel cells such as serpentine, pin, interdigitated and straight flow fields but the most obvious choice is multiple serpentine. The same can be used for high temperature PEM fuel cell (HT-PEMFC) application with ease because of absence of

liquid water during the high temperature operation and no need for complex water management.

The gas distribution is strongly dependent on the geometry of flow fields used which provide the pathways for gases. For HT-PEMFCs, conventional serpentine flow fields have been widely used. However, the alternatives need to be considered when better current density distribution with minimum pressure drop is requirement for enhanced performance especially for large active area cells. The advantage in current density uniformity means that the flow field design can be of importance when there is a constraint on the maximum current density and thermal gradient when the cell area is scaled up. In this thesis, to investigate the impact of the flow field pattern on the performance and degradation of HT-PEMFCs a series of experiments (long term stability tests, potential cycling test and potential holding test) are carried out to compare a conventional multiple serpentine, modified serpentine and a straight and parallel flow field design. The influence of three different cathode flow field designs are investigated on the long term performance and stability of HT-PEM fuel cell. Three HT-PEMFCs are assembled with multiple serpentine, segmented serpentine and straight and parallel design on cathode of fuel cell whereas the anode flow field design (multiple serpentine) remains the same. The anode and cathode stoichiometry of 1.2/2 is used for hydrogen and air respectively at ambient pressure. Also, a series of electrochemical characterization are carried out to compare the performance of HT-PEMFC with these flow fields.

The project progresses to identify the operational degradation mechanism of the each HT-PEMFC mainly due to change in cathode flow field design, which will be interpreted with use of polarisation curves, electrochemical characterization studies such as electrochemical impedance spectroscopy (EIS), cyclic voltammetry (CV) and linear sweep voltammetry (LSV). The cathode off-gas is continuously monitored during fuel cell operation using Fourier transform infrared spectroscopy (FT-IR) to assist in performance degradation characterization evaluation for potential holding test. The phosphoric acid loss rates in the case of potential cycling tests are estimated using inductively coupled plasma optical emission spectrometry (ICP-OES) correlated with membrane degradation. The cathode is preferentially studied over anode in terms of degradation mechanisms.

Overall the results from various characterization methods are used to understand degradation mechanisms of HT-PEMFC during steady-state and accelerated stress test (AST) conditions. The performance deterioration mechanisms will be investigated based on the chronological changes in the performance curves, internal cell resistance, electrochemical surface area (ECSA) and platinum particle size estimated from transmission electron microscopy (TEM) and X-ray diffraction (XRD).

The long term stability tests for 500 h at constant current density of 0.2 A cm^{-2}, after the 100 h break-in period confirm that straight and parallel design can be used as an alternative to serpentine designs to achieve better performance over long term operation. However the performance loss is observed with increased operation time within the 500 h operation is due to increase of charge transfer resistance and Pt particle sintering.

Based on the study conducted herein potential cycling regime between 0.5 V and 0.9 V is highly detrimental to HT-PEMFC. The ECSA of fuel cell cathode is drastically reduced after AST period due to significant increase in platinum particle growth confirmed from post-mortem TEM results, 4 to 8 nm for a fresh to degraded catalyst on cathode side respectively.

The potential holding tests at 0.9, 1.0, 1.1 and 1.2 V for 30 minutes showed severe degradation at 1.2 V applied potential confirmed from polarisation curves. 63.55 µg cm^{-2} of carbon dioxide (CO_2) is measured from cathode exhaust after the 1.2 V potential test. The increase in charge transfer resistance and decrease in the ECSA suggests that the main reason for performance degradation during the applied potential is due to degradation of the carbon support at cathode catalyst layer. The carbon in the catalyst support is electrochemically oxidized to CO_2 causing agglomeration of platinum particles.

The straight and parallel flow field design is intended as an alternative to serpentine flow field, especially operation at steady-state with low current density and better current density distribution with low pressure drop is the requirement in the large active area fuel cells and also when scaled-up to stack level.

Acknowledgements

This thesis work is conducted in HySA Systems and supported by Hydrogen and Fuel Cell Technologies RDI Programme (HySA), funded by the Department of Science and Technology in South Africa (Project KP1-S03).

I would like to thank my supervisor Dr Sivakumar Pasupathi and Dr Piotr Bujlo for their personal and professional support during the course of thesis at HySA Systems.

I thank department of science and technology (DST), South Africa for funding my thesis and various conferences attended by me.

The machining of the cell graphite plates by Mr. Clement Cornelius is greatly acknowledged.

I thank my fellow colleagues Mr. Stanford for their support with my experiments in lab.

I am grateful to my Indian friends at Tuscan Park Villas, Bellville for their support.

List of Tables

List of Figures

Chapter 4

Appendix

List of Abbreviations

AST Accelerated Stress Test

BoP Balance of Plant

BoL Beginning of Life

CCM Catalyst Coated Membrane

CFD Computational Fluid Dynamics

CHP Combined Heat and Power

CL Catalyst Layer

CPE Constant Phase Element

CV Cyclic Voltammetry

DPS Danish Power Systems

ECSA Electrochemical Surface Area

EDS Energy Dispersive Spectroscopy

EIS Electrochemical Impedance Spectroscopy

EoT End of Time

FCEV Fuel Cell Electric Vehicle

FT-IR Fourier Transform Infra-Red

GDL Gas Diffusion Layer

HF High Frequency

HOR Hydrogen oxidation reaction

HT-PEMFC High Temperature Proton Exchange Membrane Fuel Cell

ICE Internal Combustion Engine

ICP-OES Inductively Coupled Plasma Optical Emission Spectroscopy

IF Intermediate Frequency

IECD Intrinsic Exchange Current Density

LF Low Frequency

LHV Lower Heating Value

LSV Linear Sweep Voltammetry

LT-PEMFC Low Temperature Proton Exchange Membrane Fuel Cell

MEA Membrane Electrode Assembly

MCFC Molten Carbonate Fuel Cell

OCV Open Circuit Voltage

ORR Oxygen Reduction Reaction

PA Phosphoric Acid

PBI Polybenzimidazole

PEM Proton Exchange Membrane

ppm Parts per million

RH Relative Humidity

SEM Scanning Electron Microscopy

SOFC Solid Oxide Fuel Cell

TEM Transmission Electron Microscopy

XRD X-ray Diffraction

H_2 Hydrogen

H_2O Water

H_3PO_4 Ortho phosphoric acid

CO Carbon monoxide

CO_2 Carbon dioxide

N_2 Nitrogen

Pt Platinum

Contents

1 Introduction

With increasing population there is a growing demand for energy worldwide. The world population is estimated to be 7.6 billion in 2018 with China, India and United States being the leaders of the statistic [1]. The world is affected by overpopulation, rapid industrialization, urbanisation and thereby growing demands for energy (mainly electricity and transportation). Natural resources are being consumed at a rate that they can soon be depleted and over usage of these has led to a large increase in greenhouse gas emissions which needs to be controlled. The atmospheric carbon dioxide (CO_2) level is 406 ppm in 2018 [2]. World energy is predominantly used for transportation, industry and building. Global fossil carbon emissions are highest from coal, petroleum and natural gas. Replacing fossil fuel with renewable energy is a vital solution to green economy. The Table 1-1 shows the estimation of global electricity production by the end 2016 [3]. It can be observed that the global share of renewable electricity is only 25% including hydro, wind, solar, ocean and geothermal means.

Table 1-1 Renewable energy share of global electricity production by the end of 2016 [3].

Source of energy	Global share / %
Non-renewable electricity	75.50
Renewable electricity	24.50
Hydro power	16.60
Wind power	4
Biological power	2
Solar PV	1.50
Ocean, geothermal and other	0.40

But recently, a major transition in energy sector is observed especially electrification of transportation and various energy storage technologies are considered; more changes are expected in next two decades.

1.1 Comparison of various energy storage technologies

There are many energy storage technologies available in the market for utility scale energy storage systems like super-capacitors, flywheels, batteries, pumped hydro and hydrogen technologies. Each technology has its own advantages and limitations. The power handling capacity of energy storage devices and the duration for which this power can be sustained is shown in Figure 1-1. It can be observed that the super-capacitors, flywheels have shorter discharge durations. Hydrogen storage technology is attractive because it preserves energy for longer durations as can be seen from Figure 1. Hydrogen is abundant in universe and it can be stored and transported over long distances.

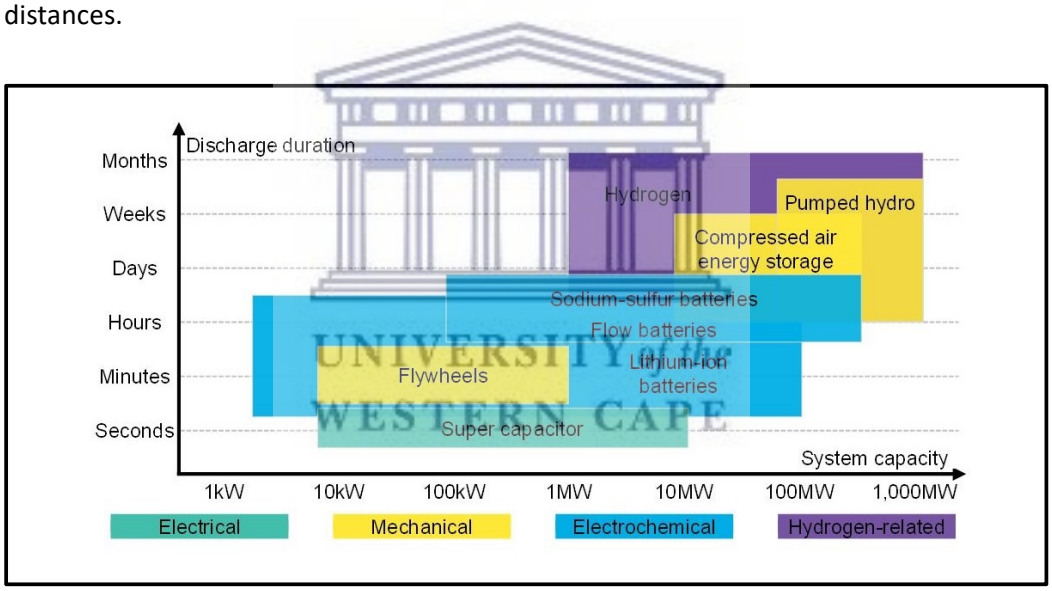

Figure 1-1 Size and discharge durations by energy storage technologies [4].

1.2 Hydrogen economy

Hydrogen, the simplest and abundant element in universe, is considered as a clean fuel in transportation and power generation. The term hydrogen economy refers to using hydrogen as an energy carrier. Hydrogen could be used to transport energy from long distances and store it.

The hydrogen can be used to generate electricity using fuel cells with high efficiencies and can be combusted in air to give energy for space heating with a potential to replace natural gas in industry. Hydrogen has high energy density by weight compared to

gasoline. 1 kg of hydrogen gas contains the same energy as 1 gallon of gasoline. Hydrogen is abundant in our environment in the form of water, hydrocarbons for example methane and bio-mass. The main challenge is to efficiently extract hydrogen from these sources as the gas does not exist on Earth in a free form. Hydrogen is mainly produced from chemical conversion of fossil fuels and electrolysis of water using electricity as well as is a by-product of chemical processes [5]. There exist numerous hydrogen production pathways 1) natural gas reforming (the most common and efficient method), 2) gasification of coal, 3) electrolysis (the electricity used for process is generated from fossil fuel, nuclear and renewables like solar, wind), 4) renewable liquid reforming, 4) fermentation, 5) high temperature water splitting, photo biological water splitting, photo-electrochemical water splitting (currently under development) [6]. The main challenge for hydrogen production is reducing the cost of production which would help to boost commercialization of fuel cell technology.

Hydrogen can be produced at point of usage or produced, stored and distributed to required place. The distribution of hydrogen for automotive applications needs infrastructure and fuelling stations. Hydrogen is distributed as gas with pipelines or tanks in a liquid form or compressed to a high pressure gas. Commercialization of fuel cell technology and applications is dependent on availability of fuel stations. However, there are problems associated with hydrogen such as leak detection and metal embrittlement. Developing hydrogen production methods can minimize distribution issues [7, 8].Hydrogen storage is required on board a fuel cell electric vehicle (FCEV). Hydrogen has very high energy content by weight 33 kWh kg^{-1} based on lower heating value (LHV), but it has very low energy content by volume 0.53 kWh L^{-1} stored with 20 M Pa. This makes hydrogen a challenge to store, particularly within fuel cell vehicle. Developing safe and cost-effective hydrogen storage technologies helps commercialising the fuel cell technology. The issue with hydrogen as a fuel comes from hydrogen gas which is highly flammable and will burn in air at a very wide range of concentrations between 4 percent and 75 percent by volume in the presence of sunlight, flame or spark [9]. Hydrogen flames are invisible to human eye. Hydrogen is odourless.

In summary the hydrogen economy reduces the negative consequences of using hydrocarbon fuels. Hydrogen is an energy carrier not a form of primary energy source. Hydrogen economy is the solution to pollution from hydrocarbon fuels. Hydrogen economy is represented in a block diagram in Figure 1-2. Challenges to hydrogen economy are cost, storage, infrastructure and purity of hydrogen for some applications. Government, industry and R&D are trying to overcome the barriers to efficient hydrogen production, distribution and storage to boost fuel cell technology for a sustainable future.

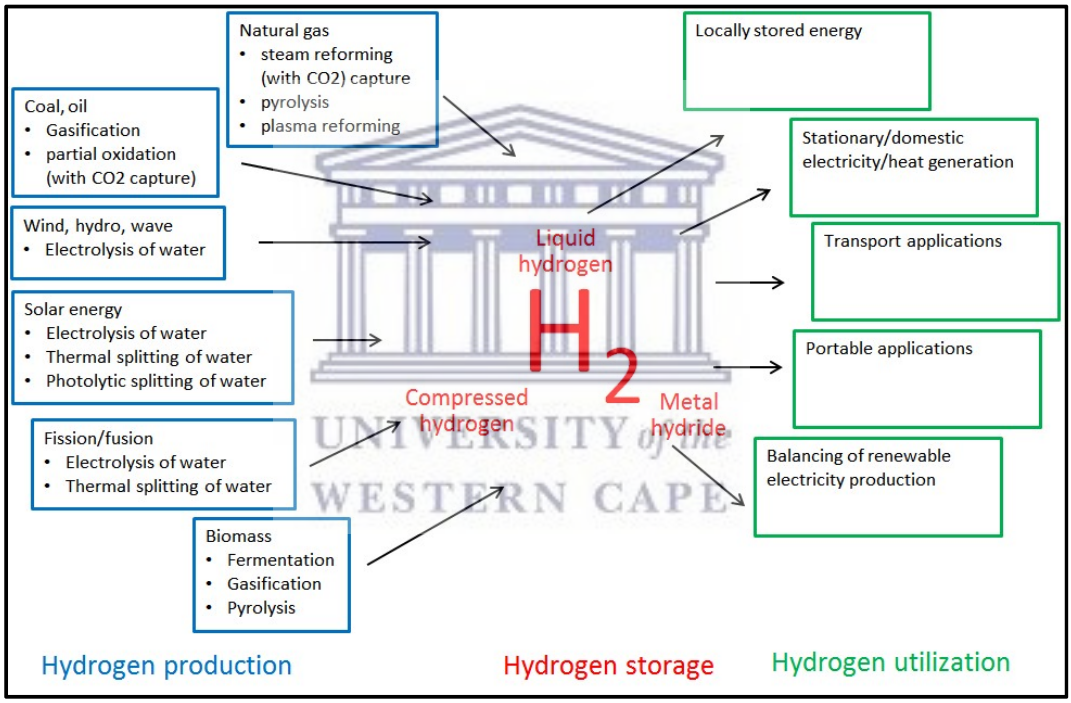

Figure 1-2 Hydrogen economy in block diagram from hydrogen production, storage to utilization.

1.2.1 Fuel cell types and applications

Conventionally electricity is generated from coal, petroleum products, natural gas, nuclear energy and renewable energy sources. Combustion engines and power stations generate electricity by converting chemical energy of fuel to thermal energy. The thermal energy is converted to mechanical energy and then mechanical energy to electrical energy and because of this multi-step conversion there are many losses in system with lower efficiency. If fossil fuels are used as a fuel this process contributes to

pollution. Fuel cells use hydrogen and oxygen to generate electricity via electrochemical reaction in a more efficient way in a single step. The principle ways of power generation using fuel cells, steam turbines and combustion engines is presented in Figure 1-3.

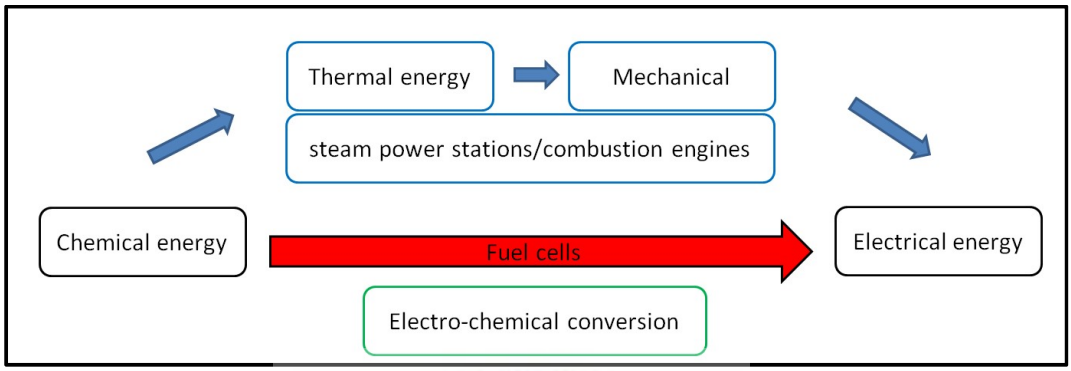

Figure 1-3 Schematic of energy conversion process fuel cell and combustion engines.

1.2.1.1 Fuel cell classification

Fuel cell can be classified based on the operating temperature and type of electrolyte or membrane used. Polymer electrolyte membrane fuel cells (PEMFC) typically have the lowest operating temperatures and solid oxide fuel cells (SOFC) have the highest operating temperature as seen in Figure 1-4. The operating temperature in fuel cells defines the type of fuel and materials used. Reformed hydrocarbon fuels supplied to PEMFCs must be externally reformed and carbon monoxide (CO) has to be removed because fuel cells operating at lower temperatures have low CO tolerance. CO is known to cause poisoning of fuel cell catalyst and thereby lowering fuel cell performance and contamination of catalyst can result in degradation over long term operation. The internal reforming of hydrocarbon fuels is possible with molten carbonate fuel cell (MCFC) and SOFC because of high operating temperature. To obtain high electric efficiencies the low temperature fuel cells can be operated on hydrogen as the fuel processing losses are avoided. The cost of fuel cell system increases with increasing operating temperature because the materials used to withstand the harsher operating conditions are expensive. The technology is commercially available but still there are some challenges for mass production related to cost, safety and lifetime. Although lifetimes have been improved and new materials have been developed to replace a conventional power supply revolutionary changes are needed. R&D is focusing on

increasing the total efficiency of a system by allowing a fuel in the anode to react without fuel processing.

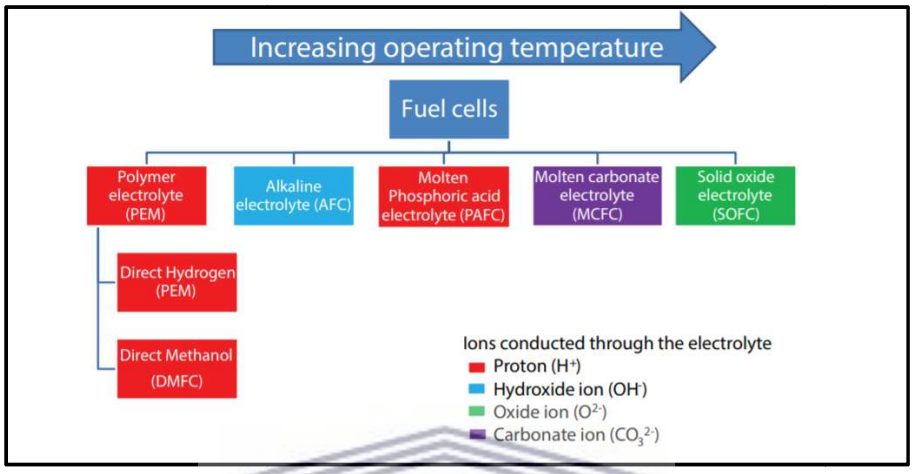

Figure 1-4 Fuel cell types [10].

1.2.1.2 Applications of fuel cells

Fuel cells are invented in 1839 and being intensively developed since last 3 decades [11]. PEMFCs cells have wide range of applications ranging from automotive and stationary to powering portable devices. Today the technology can power buses and cars, heat water and provide electricity.Fuel cells use flexible fuel input (natural gas, renewable biogas and hydrogen). Residential combined heat and power (CHP) units in the range of 1-10 kW using low temperature PEM fuel cells (LT-PEMFCs) have been deployed in Japan and South Korea [12].

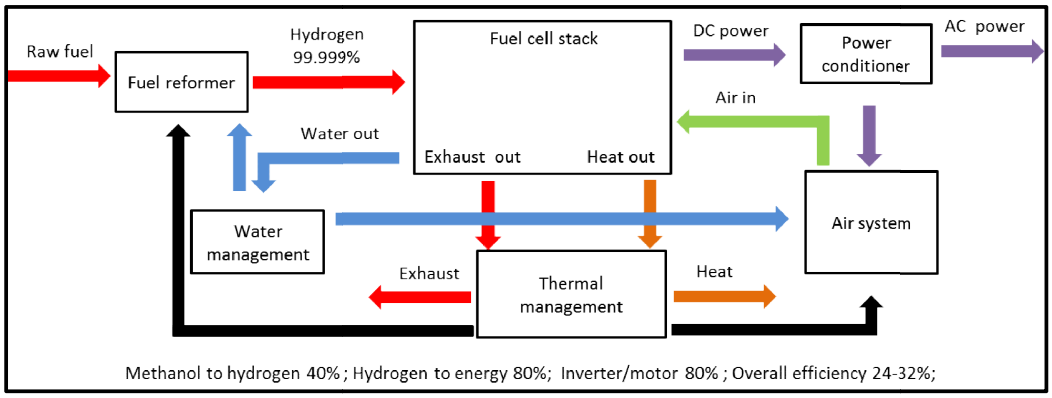

Figure 1-5 Block diagram of a fuel cell system with fuel reformer and power conditioner [13].

Stationary fuel cells have commercial applications in residential and industrial domains and provide electricity in the range of 0.5 kW–1 MW. Commercial systems provide decentralised heat and power to industrial, commercial and municipal facilities worldwide. The typical fuel cell system for such application consists of reformer, fuel cell stack, thermal and water management system and power conditioning for AC power output shown in Figure 1-5. Automotive vehicles using petrol and diesel are one of the leading causes of global air pollution. Automobiles are undergoing a major transition from conventional internal combustion engines (ICE) to vehicles running on electric drivetrain. The electricity required to power the electric drivetrain might come from batteries or from fuel cell. FCEV are promising transportation in the near future. Fuel cells have been successfully deployed in the range of 1-100 kW for transport applications in Canada, Japan, Europe and USA. Worldwide, the hydrogen technology is developing at a rapid pace with USA being leader especially in FCEV deployment [14]. Toyota would build more than 30000 per year of FCEV after 2020 [15]. In London fuel cell buses are being operated for more than 25000 hours [16]. London is also acknowledged leader in installed the largest total capacity of stationary fuel cell in any European city [17]. A FCEV uses compressed hydrogen gas stored on board and oxygen from air from atmosphere. FCEV is highly efficient compared to gasoline powered vehicle. Commercial vehicles like Hyundai Tucson SUV, Toyota Mirai and Honda Clarity ii generation have around 300 miles of range on ~ 5 kg hydrogen [18]. These vehicles are available on lease in California. The success of fuel cell technology depends on hydrogen cost and availability. The hydrogen infrastructure is being developed world wide with Canada, California, Japan and Europe spearheading. It is believed that automotive future will be dominated by fuel cells in the future because of range, adaptability and refuelling time that bring hydrogen fuel cells ahead of competition [19]. At present fuel cell vehicle technology is impeded due to lack of infrastructure and high cost of investment and fuel. Public awareness and acceptance are also challenging issues. Toyota, Daimler and BMW are leading a group of 13 companies across the world over the next 10 years in developing hydrogen technology and infrastructure [20].

1.2.2 HT-PEMFC

The PEMFCs proved to be superior over other types of fuel cells in providing higher efficiencies and power densities. They are known for their ease of handling and widespread commercial applications in automobile, stationary and portable applications. The single PEMFC consists of membrane electrode assembly (MEA) pressed in between two flow field plates and adjoining current collector plates at the end. The MEA has a membrane pressed between two micro porous layer (MPL) containing carbon supported catalyst attached to gas diffusion layer made of carbon paper or cloth. A schematic representation of a PEMFC with principle of operation is shown in Figure 1-6. The MEA is fabricated with catalyst coated to membrane or to gas diffusion layer (GDL).

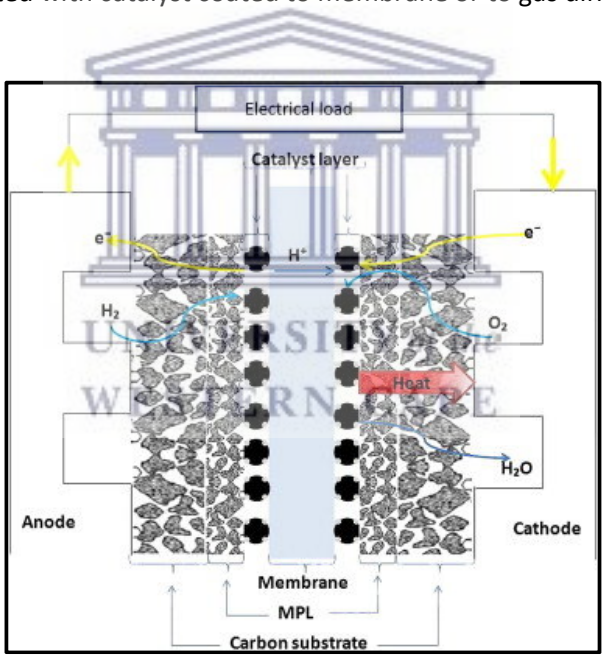

Figure 1-6 Components and principle of operation of PEMFC [21].

In a PEM fuel cell the protons generated from the anode side cross the membrane to react with oxygen on the cathode side along with electrons from external circuit to form water and heat as in equation. The oxygen reduction reaction (ORR) is sluggish reaction and rate limiting leads to voltage and efficiency losses.

Traditionally, Nafion® or similar perfluorinated polymer membranes have been used in PEMFCs. The proton conduction of these membranes depends strongly on the water content. Therefore, fuel cells running with this type of membrane only operate

efficiently below the boiling point of water, otherwise the membrane dehydrates. The LT-PEMFCs have certain issues: 1) inadequate water and heat management; 2) sluggish electrochemical kinetics; 3) intolerance to impurities (mainly CO). Increasing the operation temperature can be a solution to these problems; therefore, HT-PEMFCs which operate above 120°C-200°C have been suggested [22]. Water management can be improved because operating above 100°C and at atmospheric pressure, water will exist mainly in the vapour phase and hence mitigate potential problems associate with flooding. In addition, heat management can be simplified because heat is transferred easily with a greater temperature difference between the cell and ambient environment [23].

In a fuel cell system the overall electrochemical kinetics are dominated by the ORR because it is much slower than the hydrogen oxidation reaction (HOR). The exchange current density at Pt/Nafion® 117 interfaces, for the low current density region, increases with increase in temperature. Therefore, increasing the operation temperature can improve cathode kinetics [24]. A major limitation in fuel cells operating at low temperature is the poor CO tolerance. Hydrogen produced by reforming reactions cannot avoid traces of CO which strongly absorb on the surface of platinum, occupying HOR sites. The CO concentration as low as 10-20 ppm causes a significant loss in cell performance at 80°C. At higher temperatures, adsorption of CO on platinum is less favoured, because of its high negative entropy, which will benefit fuel cell performance at 130°C (tolerate up to 1000 ppm) [23].

HT-PEMFCs typically use a membrane made of a polybenzimidazole (PBI) known to have very good oxidative, thermal and mechanical properties. PBI membrane when doped with phosphoric acid (PA) has proton conductivity comparable to adequately wet Nafion membrane. HT-PEMFC's have been attracting attention because of improved cathode kinetics and CO tolerance compared to LT-PEMFC. The advantages of HT-PEMFC are flexibility in fuel (reformate, hydrogen) supply, humidification of membrane is not required and cathode air cooling is possible. As a result the weight of the system and balance of plant (BoP) is reduced. HT-PEMFCs are being developed for these key advantages. HT- PEMFCs seem more suitable for stationary power applications combined with heat and power generation. For mobile applications (in particular for

automobile applications) more challenges exit due to start up time and thermal/load cycling.

The MEA is the "heart" of fuel cell and the individual electrochemical reactions that take place at anode and cathode of fuel cell are given in Equation 1-2 and 1-2 respectively.

Anode: $H_2 \rightarrow 2H^+ + 2e^-;\ E^\circ = 0\ V$ (eq. 1-1)

Cathode: $O_2 + 4H^+ + 4e^- \rightarrow H_2O;\ E = 1.23\ V$ (eq. 1-2)

The thermodynamic reversible cell voltage (E_{rev}) is also known as maximum theoretical cell voltage can be obtained from Nernst equation for PEMFC reaction as in Equation 1-3 [25].

$$E_{rev} = E^\circ + \left[\frac{\Delta S}{n*F}\right] * [T - 298.15] + \left[\frac{R*T}{2*F}\right] * \ln\left[\frac{P_{H_2} * P_{O_2 0.5}}{P_{H_2O}}\right] \quad \text{(eq. 1-3)}$$

$E^\circ = 1.229$ when the product water is in a liquid form;

$E^\circ = 1.16$ when the product water is in a gaseous form;

The cell potential is a function of temperature and pressure. So, for HT-PEMFC at 160°C and 0.21 atm of partial pressure of oxygen in air of 1 atm, the $E_{rev} = 1.137$. The maximum theoretical efficiency of a fuel cell ($\eta_{fuel\ cell}$) is defined as the ratio between the energy output (electrical energy produced) and energy input (enthalpy of hydrogen). $\eta = \frac{\Delta G}{\Delta H}$ (83% when higher heating value (HHV) of hydrogen is used) [26]. The efficiency of a fuel cell decreases with higher operating temperatures. The maximum theoretical cell voltage is the reversible cell voltage and maximum thermodynamic efficiency is calculated from standard enthalpy of reaction at 25°C.

1.2.2.1 Membrane

HT-PEM fuel cells use typically PBI based membranes which are now commercially available. These membranes operate at higher temperature and proton conduction is possible without hydration. The chemical structure of PBI membrane used in this kind of fuel cells is presented in Figure 1-7. When doped with PA significant proton conductivity can be achieved in non-humidified condition.

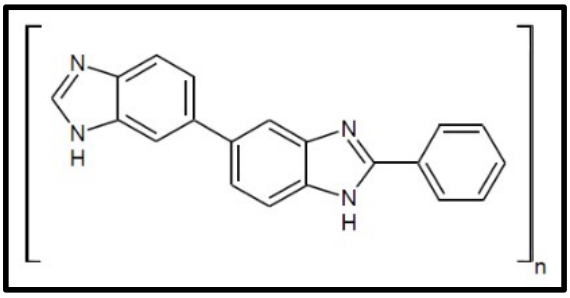

Figure 1-7 PBI polymer structure [24].

The PBI membrane in commercial MEA have following properties[27]:

a) Mechanical strength (maximum tensile strength is12 M Pa for acid doping level of 5.5 - 6.7)
b) Thermal properties (pure PBI hashigh glass transition temperature420-436^{o}C)
c) Water transport (bydiffusion and permeationmechanisms)
d) High doping level (upto70 molecules of PA per PBI repeating unit)
e) Proton conductivity (0.02-0.08 Scm^{-1})
f) Gas permeability (pure PBI has lower gas permeability in comparison to doped PBI)
g) Water uptake (> 3.2 molecules of water depending on the PA doping level)

The PBI polymer and inorganic acid contain hydrogen bonding sites. The protons jump from one site to other without a carrier across the membrane like a hopping mechanism. The conductivity is dependent on acid doping, temperature and humidification which needs to be optimised. Water content in the membrane has a significant effect on conductivity.

The companies that supply membrane components for HT-PEMFCs technology are mentioned in Table 1-2. BASF Fuel Cell Inc. commercialized MEAs designed specifically for 120-180°C PEM fuel cell stacks with products named Celtec®-P MEA. Which is now acquired by Advent Technologies SA, a Greek base company which offers currently five and seven layer high temperature membrane electrode assemblies (MEA). Danish Power Systems (DPS) is a development, research and consulting company. DPS is developing and manufacturing MEAs for HT-PEMFC, these MEAs are available in a number of standard sizes and they are registered under the Dapozol® trademark. FuMA-tech

supplies a wide variety of ion and proton exchange membranes for HT-PEMFC applications.

Table 1-2 Commercial HT-MEA suppliers and membranes used along with gas diffusion layers (GDLs).

Commercial supplier	Membrane	GDL
Fuma-tech®	AB-PBI	Carbon paper
Advent TPS®	Pyridine based aromatic poly ethers	non-woven carbon paper
BASF Celtec® MEAs	m-PBI	Woven carbon cloth
Danish power systems Dapazol® MEAs	PBI	Non-woven carbon cloth

1.2.2.2 Catalyst layer

The catalyst layer (CL) of HT-PEMFC is a thin layer of a few tens µm thick. It consists of carbon particles supported catalysts and the fluorine-based resin as a water repellent and a binder (typically platinum catalyst or platinum alloy catalyst with particle size of 2-3 nm, dispersed on high surface area carbon on anode and cathode side of fuel cell). Generally, Pt based catalysts are used to reduce activation overpotential (the potential difference between solid phase and membrane) [28]. The electrochemical reactions catalysed by Pt are shown in Table 1-3.

Table 1-3 Hydrogen oxidation and oxygen reduction reactions at anode and cathode of the fuel cell.

Anode (HOR)	Cathode (ORR)
$\mathbf{2Pt + H_2 \leftrightarrow 2Pt - H}$	$2Pt + O_2 \leftrightarrow 2Pt - O$
$\mathbf{Pt - H \leftrightarrow Pt + H^+ + e^-}$	$Pt - O + 2H^+ + 2e^- \leftrightarrow Pt + H_2O$

Platinum, carbon support and binder or ionomer together form a CL with three phase interface shown in Figure 1-8. The structure and composition of this CL effect fuel cell performance. The stability of platinum and carbon support is crucial for durability of this kind of fuel cells. Efforts are being made to improve fuel cell performance and life time

as well as reduce cost by using non precious metal catalyst, lower platinum loadings, introduce platinum alloys (Pt_3Co/C alloy). Carbon supports like graphitised carbon, heat treated carbon and multi-walled carbon nanotubes are used to improve the catalyst support durability and performance.

Different types of binders (PTFE, PBI and Polyurethane) are used in electrodes of PBI membrane based HT-MEAs to increase life time. They enhance the performance of fuel cells by 1) improving platinum utilization, 2) improving Tafel slope [29] and 3) decreasing ohmicoverpotential. To obtain a better performance there should be good contact between electrolyte, carbon support, and platinum nanoparticle so that the reaction between protons, electrons and oxygen can take place effectively on the cathode side because the sluggish ORR happens at cathode side. After the fuel cell assembly the PA from the PBI diffuses into the electrodes and activation conditions also allow better redistribution of PA. To maximize the life time and performance of HT-PEMFC the MEA should be carefully designed for better redistribution of phosphoric acid between membrane and catalyst layers and GDL.

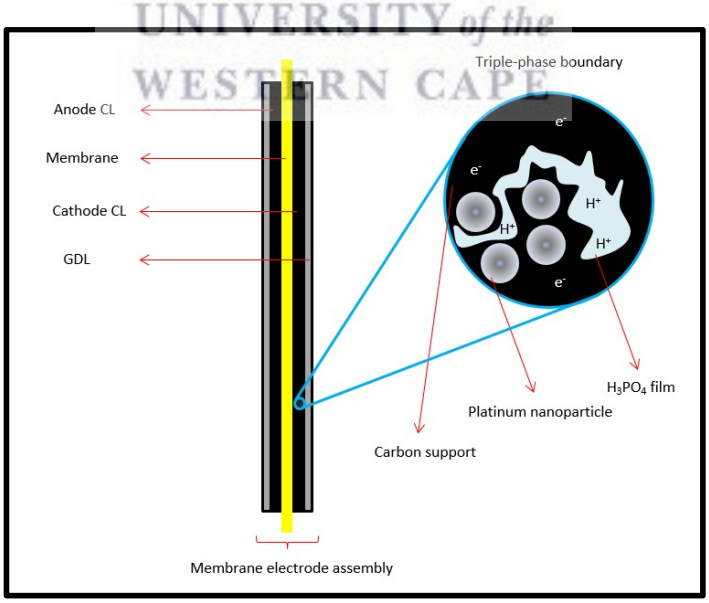

Figure 1-8 MEA cross section and its components with triple phase boundary.

1.2.2.3 Gas diffusion layer

The GDL is an essential component of HT-PEMFC. They are arranged on the both sides of the electrolyte membrane of the catalyst layers. And the GDL is composed of carbon paper or cloth of 100 to 300 µm thick, which has excellent conductivity and gas permeability. It is made of carbon cloth interwoven or in some cases with carbon paper as mentioned in Table 1-2. It has macro porous layer (carbon fibre matrix) and micro porous layer (MPL). Fuel and air diffuse into the catalyst layer through the GDL. Conversely, water generated in the catalyst layer of cathode side by the electrode reaction is also discharged to the flow channels of flow field plates through the GDL.

1.2.2.1 Flow field plates

The flow field plates called bipolar plates contribute more than 80% of stack volume and weight. The flow field plates have two main functional requirements electrical and mechanical. Materials like graphite, metals and composites have been used for flow field plates. Metals like stainless steel, aluminium, titanium have good electrical conductivity and mechanical strength but poor corrosion resistance in the fuel cell environment. Graphite has good corrosion resistance but mechanical integrity is compromised. Composite plates (carbon reinforced polymer composite) have high specific strength and stiffness however large area specific resistance is an obstacle.

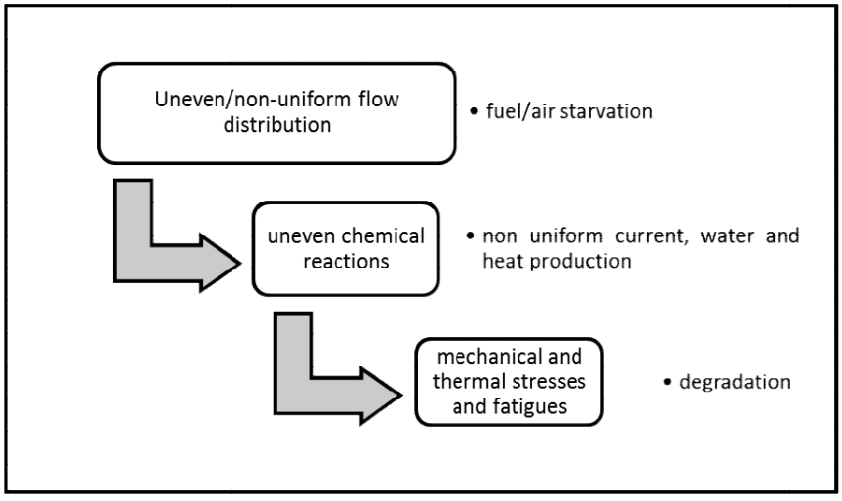

Figure 1-9 Schematic of pathways to degradation from flow field design of bipolar plates.

Bipolar plates made of graphite composite are currently in use due to its chemical stability and high conductivity. Metallic plates are slowly replacing graphite plates in order to reduce the cost, increase the volumetric power density and enhance the mechanical strength.

The flow field plates contain flow channels to distribute the reactant gases over electrode active area and provide water and heat removal from the cell. The primary function of flow fields is to provide homogeneous distribution of reactant gases over the active area with minimum pressure drop and thereby obtain higher performance. Performance failures are caused from uneven flow distribution and high pressure drops leading to cell degradation as shown in Figure 1-9. The flow field plates are attached to current collector plates and endplates with provisions for gas manifold. The end plates (made of stainless steel, aluminium etc.) are used to mechanically support and maintain structural integrity of various cell components. To avoid gas leaks and reactant crossover, suitable gaskets (sealing materials) are used depending on the operating conditions. Silicon, PTFE and EPDM rubber are commonly used gasket materials for sealing purposes with good compressibility. In some cases gaskets are bonded to MEA for better gas tightness. The high operating temperature eliminates the problems of water management so wide range of flow designs can be used for HT-PEMFC. More details concerning the flow field configurations and effects are discussed over section 2.1.

1.3 Problem statement

Literature with variations in flow field design and effects on fuel cell performance do exist for LT-PEMFC but are very limited for PBI based fuel cells. An experimental comparative study of flow field designs and their effects on fuel cell performance only at beginning of life (BoL) is generally considered. However, the effects of long term operation and due to various operating procedures are scarcely investigated. The gas distribution is strongly dependent on the geometry of flow fields used which provide the pathways for gases. For HT-PEMFCs, conventional serpentine flow fields have been widely used. However, the alternatives need to be considered when better current density distribution with minimum pressure drop is requirement for enhanced

performance especially for large active area cells. The advantage in current density uniformity means that the flow field design can be of importance when there is a constraint on the maximum current density and thermal gradient when the cell area is scaled up.

1.4 Research aims and objectives

The aim of the current thesis is to investigate the influence of three different flow field designs on the performance and degradation of HT-PEMFCs. A series of experiments with steady-state and accelerated stress test (AST) conditions are carried out to compare influence of conventional multiple serpentine, modified serpentine and straight and parallel flow field design. Also, a series of electrochemical characterization are carried out to compare the performance and flow field induced effects on HT-PEMFC.

In this work, cathode will be preferentially studied over anode in terms of degradation of HT-PEMFC. Accomplishment of thesis is done by performing long term stability tests, potential cycling AST test and potential holding AST test on single HT-PEMFC with different cathode flow field designs mentioned above, while keeping the anode flow field design constant for all the tests performed.

The objectives of this thesis are to identify the operational (because of long term stability tests, potential cycling tests and potential holding test) degradation mechanism of the each HT-PEMFC mainly due to change in cathode flow field design, which will be interpreted with use of polarisation or I-V curves and electrochemical characterization studies such as electrochemical impedance spectroscopy (EIS), cyclic voltammetry (CV) and linear sweep voltammetry (LSV). The cathode exhaust gases are continuously monitored during fuel cell operation to assist in performance degradation evaluation for potential holding test. The PA loss rates in case of potential cycling tests are quantified and interpreted. Overall, the results from these characterization methods will be used to understand degradation mechanisms of HT-PEMFC during normal operation conditions and AST operation. The performance deterioration mechanisms will be investigated based on the chronological changes in the cell polarisation losses and internal cell resistance and structural changes of electrode (electrode composition and Pt particle

size) analysed using scanning electron microscope (SEM), transmission electron microscope (TEM) and x-ray diffraction (XRD).

1.5 Thesis outline

This thesis is divided into 5 chapters and study concerns the effect of flow field design on degradation mechanisms and long term stability of HT-PEMFC using Celtec®-P2100 HT-MEA of 96 cm^2 geometrical active area.

Chapter 1 begins with introduction to electricity from various renewable and non-renewable energy resources along with hydrogen economy and brief comparison of LT-PEMFC vs. HT-PEMFC. Application of fuel cells and components of HT-PEMFC are described. The aims and objectives of the thesis are also mentioned in this chapter.

Chapter 2 details the literature review concerning the flow field classification and degradation aspects of HT-MEA components. The background of characterization techniques used in this thesis are described.

Chapter 3 presents details of fuel cell assembly, test station, experimental procedures and characterization methods (both in-situ and ex-situ) used in this thesis.

Chapter 4 is segregated into 5 subsections displaying experimental results from characterization of single cell and potential holding test with multiple serpentine design; EIS analysis with three different flow field designs using a manual test station. Then analysis and discussion of long term stability test results followed by potential cycling results.

Chapter 5 gives the conclusion from the results of experiments conducted in this work followed by scope for future work to use the present results for further analysis improvement of HT-PEMFC technology.

References

[1] http://www.worldometers.info/world-population/ accessed on 25 September 2018.

[2] https://www.co2.earth/ accessed on 25 September 2018.

[3] http://www.ren21.net/status-of-renewables/global-status-report/ accessed on 25 September 2018.

[4] https://about.bnef.com/blog/better-than-a-battery-big-energy-backs-hydrogen-power-storage/ accessed on 26 September 2018.

[5] http://homework.uoregon.edu/pub/class/es202/out202/hyd.html accessed on 26 September 2018.

[6] http://www1.eere.energy.gov/hydrogenandfuelcells/pdfs/fct_h2_production.pdf accessed on 26 September 2018.

[7] https://www.afdc.energy.gov/fuels/hydrogen_production.html accessed on 26 September 2018.

[8] http://www1.eere.energy.gov/hydrogenandfuelcells/pdfs/fct_h2_storage.pdf accessed on 26 September 2018.

[9] https://courses.lumenlearning.com/boundless-chemistry/chapter/hydrogen/ accessed on 26 September 2018.

[10] S. Badwal, S. S. Giddey, C. Munnings, A. I. Bhatt, and A. F. Hollenkamp, "Emerging electrochemical energy conversion and storage technologies," Front. Chem., vol. 2, no. 79, pp. 1–28, 2014.

[11] http://www.fuelcelltoday.com/history accessed on 26 November 2018.

[12] https://www.hydrogen.energy.gov/pdfs/48265.pdf accessed on 26 November 2018.

[13] https://www.slideshare.net/ahmedelkholy30/fuel-cell-61235783 accessed on 26 November 2018.

[14] https://www.iea.org/tcep/energyintegration/hydrogen/ accessed on 26 November 2018.

[15] https://newsroom.toyota.co.jp/en/corporate/22647198.html accessed on 26 November 2018.

[16] http://www.ballard.com/about-ballard/newsroom/news-releases/2017/08/29/ballard-powered-fuel-cell-electric-bus-achieves-25-000-hours-of-revenue-operation accessed on 26 November 2018.

[17] https://www.london.gov.uk/sites/default/files/london-a_capital_for_hydrogen_and_fuel_cell_technologies.pdf accessed on 26 November 2018.

[18] https://www.caranddriver.com/hyundai/tucson-fuel-cell accessed on 26 November 2018.

[19] https://spectrum.ieee.org/green-tech/fuel-cells/why-the-automotive-future-will-be-dominated-by-fuel-cells accessed on 26 November 2018.

[20] https://www.altenergymag.com/article/2018/02/hydrogen-fuel-cell-cars-are-coming--maybe/27986/ accessed on Febraury 2019.

[21] A El-kharouf, T. J. Mason, D. J. L. Brett and B. G. Pollet, "Ex-situ characterisation of gas diffusion layers for proton exchange membrane fuel cells", J. Power Sources, 218, 393-404, 2012.

[22] C. Yang, "Approaches and technical challenges to high temperature operation of proton exchange membrane fuel cells," J. Power Sources, 103 (1) 1-9, 2001.

[23] J. Zhang et al., "High temperature PEM fuel cells," J.Power Sources, 160 (2) 872-891, 2006.

[24] C. M. Rangel and T. Sousa, "High Temperature Polymer Electrolyte Fuel Cells," 2011.

[25] G.Bandlamudi, "Systematic characterization of HT-PEMFCs Containing PBI/H3PO4 systems: Thermodynamic analysis and Experimental investigations", ISBN 978-3-8325-2962-8, 2011.

[26] F. Barbir, "PEM Fuel Cells 2nd Edition Theory and Practice", ISBN 978-0-1238-7710-9, 2012.

[27] S. Galbiati, Doctoral thesis: Experimental Study of Polybenzimidazole based High Temperature Polymer Electrolyte Fuel Cells, Politecnico di Milano, 2012.

[28] F. Hashemi, S. Rowshanzamir and M. Rezakazemi, "CFD simulation of PEM fuel cell performance: Effect of straight and serpentine flow fields", Mathematical and Computer Modelling, 55, 1540-1557, 2012.

[29] J. O. Park, K. Kwon, M. D. Cho, S.-G. Hong, T. Y. Kim and D. Y. Yoo, "Role of Binders in High Temperature PEMFC Electrode", Journal of Electrochemical Society, 158 (6) B675-B681, 2011.

2 Literature review

In this section the various flow field geometries used for PEMFCs are discussed followed by degradation mechanisms of HT-PEMFC and its characterization methods relevant to this thesis.

2.1 Flow field classification

A fuel cell stack is made up of repeated assembly of single unit cells. The performance of a fuel cell stack depends on the individual cells of the stack. Similarly, the lifetime and durability of stack are approximately the durability and lifetime of its worst performing single unit cell. The uneven flow distribution is the main cause of the performance loss and degradation of a large scale stack after scaling-up [1]. If some of the cells in a stack or some of the channels in cell deviate from design conditions due to an uneven flow distribution result in an uneven electrochemical reaction and high pressure drop. Uneven water, heat and current generation or in severe cases drying, flooding and hotspots may arise from uneven electrochemical reaction [2]. Drying can cause chemical degradation which is further enhanced in cycling conditions compared to steady-state operation. Hot spots and uneven temperature profiles cause thermal stress and membrane creep due to temperature differences resulting in mechanical failure of membrane and sealing materials used in PEMFCs. High pressure drops are often caused by long channels. The problems associated with high pressure drop are 1) requires a powerful pump to overcome flow resistance. The high parasite power may reduce the overall efficiency of the power system; 2) the pressure gradient between the adjacent channels of a flow field in a cell becomes substantial. The possibility of cross leakage between the adjacent channels; 3) may cause mechanical stresses between inlet and outlet, leading to perforations, cracks or pinholes in membranes (stronger materials are required for membrane, BP, GDL and sealing); 4) high difference of reactant concentration from the flow channel inlet to the outlet. This can cause considerable Nernst losses for practical cells of large size fuel cells [3]. For stack, a loss in pressure should not go beyond 30 % of its initial pressure at inlet [4].

Fuel cells design should be done based on the energy demand to specify the active area and number of cells. Enhancement of the flow field configuration, and hence improvement of performance can reduce the cost as much as 50 % [4]. The BP is central to the flow field designs of fuel cells. In reality, the stack design mostly compromises of BP design. There are many types of flow field layouts, structures, dimensions and flow conditions, making the best choice of specific combination to meet the two criteria high uniformity and low pressure drop is main challenge of fuel cell design [5]. Trial and error is the most common approach to design and evaluate flow fields. As of today, there are many types of flow field designs as reviewed by for fuel cell applications such as serpentine, parallel, interdigitated, pin and spiral flow fields [4]. A great research has been involved in designing and investigation the influence of different types of flow fields.

A single channel configuration is the simplest to distribute the gas reactant through a spiral or serpentine pattern on the active area. This type of single channel configuration has no flow distribution problems since only one channel is used for small active area fuel cell. But for large active area fuel cell the length of single channel increases with size and a high pressure drop occurs due to the high frictional resistance of the long channel. The high pressure drop in the single serpentine or spiral may be as much as tens of times of those in the parallel straight configurations [6]. The problems associated with high pressure drops are discussed earlier.

A straight parallel configuration has the lowest pressure drop because of short channel length which implies the lowest parasite power losses. The straight parallel configurations may cause problems related to mal-distribution of flow, which reduces the performance of fuel cell [5, 6].

The multi-parallel design has a unique advantage of a high steady-state performance with good transient response and therefore should perform better than other designs as shown in Figure 2-1 [7].

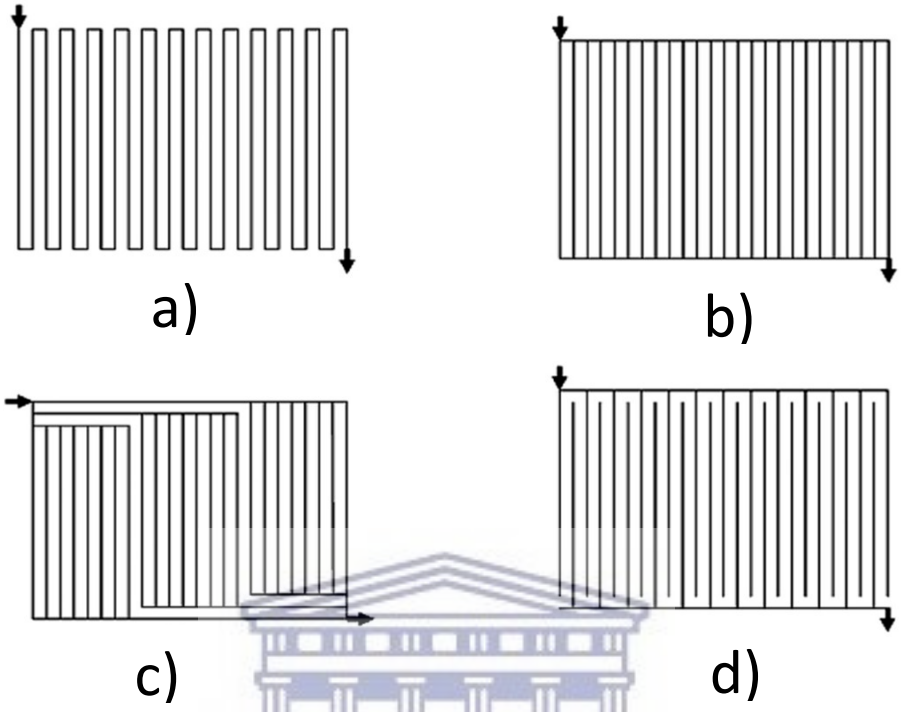

Figure 2-1 Flow field designs a) serpentine b) parallel c) multi-parallel and d) interdigitated[7].

The multi-path serpentine configurations are used to curb the problem of water flooding in the flow channels of LT-PEMFCs. The theoretical performance of six different flow field configurations as shown in Figure 2-2 are compared [5, 6]. The straight parallel configuration has the smallest pressure drops but suffered the most uneven flow distribution across the channels while the single serpentine has the best flow distribution but the largest pressure drops. The pressure drop and flow distribution in multiple serpentine flow fields are between the straight parallel and the single serpentine configurations.

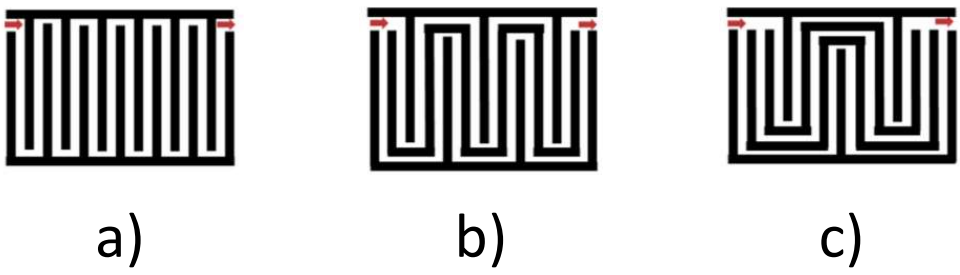

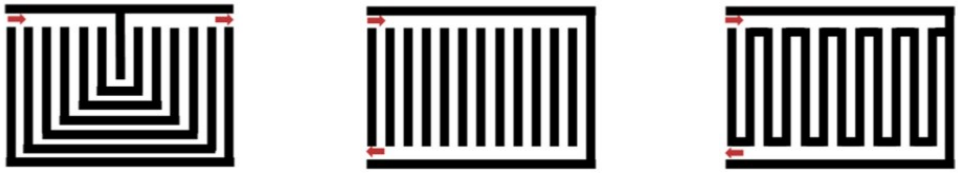

d) e) f)

Figure 2-2 Flow field designs a) single serpentine b) two-path serpentine c) three-path serpentine d) six-path serpentine e) parallel and f) interdigitated [5, 6].

In study conducted by B Tsai et al. with five different flow fields, the polarisation curves showed flow field in Figure 2-3d has the best performance with better reactant coverage of the MEA and high air utilization rates compared to flow field in Figure a, b c and e. Flow field in Figure 2-3c has higher air utilization rate than Figure 2-3a and 3b by increasing the flow path that allows longer residence time for air but also increases the pressure drop and may increase the difficulty for water removal. The single serpentine flow field has the largest pressure drop due to its long flow path (cross-sectional area is 1 mm X 1 mm) and next flow field in Figure 2-3c has the largest pressure drop due to its long flow path and flow field in Figure 2-3b has the smallest pressure drop [14] [8].

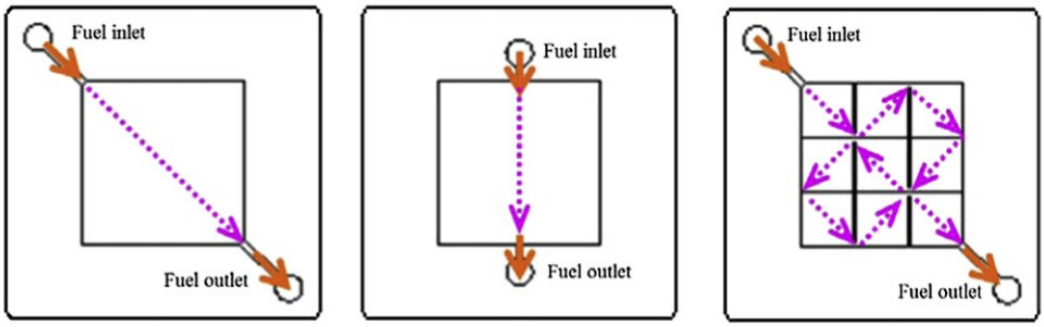

a) b) c)

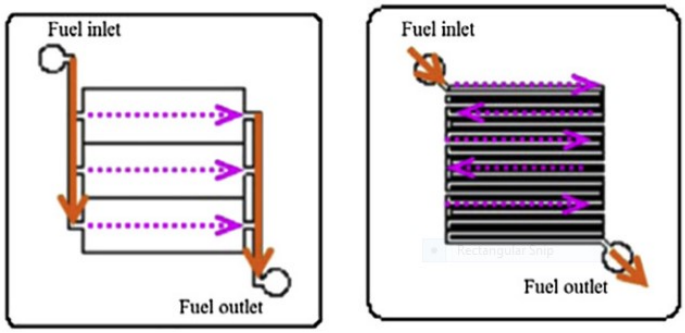

Figure 2-3 Five flow distributor designs studied a) single zone flow field with reactant flows in the diagonal direction b) single zone flow field with reactant flow is side to side c) the flow field is divided into 9 blocks with reactant sweeps over the 9 blocks sequentially d) three zone design with reactant separated into three streams and each flow through one zone e) traditional single serpentine flow field [8].

P Choopanya et al. investigated the transient performance of the three different flow field designs parallel, serpentine and interdigitated and found that the fuel cell responds immediately to the change in cell potential. They found that the interdigitated flow field design outperforms the other two designs in terms of less current overshoot and time response. The interdigitated flow channels give high pressure drop which needs to be considered for automotive applications where a single stack contains large number of cells in series, and if the cell used is typically large active area then the pressure drop will be significantly higher. For this reason, the serpentine design is the best flow field configuration as it gives a good balance between transient performance and acceptable pressure drop [9].

2.1.1 Flow fields for HT-PEMFC

The design of flow fields depends on the fuel cell application or the geometrical size of the assembly. The requirements for a flow field used in a HT-PEMFC differ from the LT-PEMFC. In a HT-PEMFC, liquid product water is not present during operation, thus porous media flooding is less of a concern. The electrochemical half-cell reactions depend on factors such as the mass/mole fraction of the species, thus they depend on the fluid flow and the flow field type [10]. The reported flow fields are numerous for usage in the field of fuel cells. They are serpentine, parallel, pin type and spiral. A

particular geometry possesses a number of parameters such as channel width, depth, the shape of cross-section, the number of turns/channels, taper ratios and path length can be optimized depending on the performance requirements. Other options include arranging reactant and oxidant distribution in co-flow or counter-flow mode. Computational Fluid Dynamics (CFD) can be used as a tool to identify the potential of different designs. There are reports based on CFD in the field of HT-PEMFCs. The significance of a CFD based study can be further augmented by supporting it with experimental data (validation with polarisation behaviour and the current density distribution measurements). The studies on 3D isothermal model of HT-PEMFC concluded that the interdigitated flow fields delivered the highest power output compared to straight, serpentine and pin type [11]. But, hot points could be generated due to heterogeneous current density distribution and also the phosphoric acid in the catalyst layer could be washed out due to convective gas flow. So, pin topology is said to be ideal under given conditions. The dimensions of manifolds and position has a significant influence on performance of HT-PEMFC [11]. Simulation studies for triple mixed serpentine design, at high operating voltages showed uniform local current density whereas, non-uniformities in the local current density are observed with decreasing cell voltages [12].

For HT-PEMFCs, serpentine flow fields have been widely used. However, various alternatives have been tried. C Siegel et al. simulated six different flow field types using COMSOL Multiphysics with serpentine flow field as reference and the details of flow fields along with (position of inlet and outlet, channel to land ratio constant) the pressure loss, average velocity, pressure loss are shown in Table 2-1 [10]. A homogeneous velocity and pressure field is found for both serpentine flow fields. The same for the pin type flow field, whereas the straight type flow field yields an inherent mal-distribution. The mixed type flow fields with mean velocities slightly lower than both serpentine flow fields used in this study as a consequence low pressure drop and quite uniform flow distribution is observed in their straight (parallel) gas channel segments. Simulated results of six parallel serpentine channels with higher lateral velocities are observed in the regions under the gas channel bends and especially in the regions of the highest pressure difference.

Table 2-1 Geometric aspects (channel to land contact area ratio at the porous media interface) and simulated fluid flow data (mean velocity in channel (u_{ch}) and mean velocity GDL (u_{GDL}) along with pressure drop and Reynold number (Re) values) [10].

Type	Channel/land mm	Contact area %	u_{ch} (m s^{-1})	u_{GDL} (m s^{-1})	ΔP (mbar)	Re
Serpentine 1	1/1	52.3/47.7	2.667	$4.6\ 10^{-4}$	9.36	72.3
Serpentine 2	1/0.9	52.6/47.4	1.778	2.8×10^{-4}	4.5	46.8
Mixed 1	1/1	50.6/49.4	0.866	8.7×10^{-5}	1.48	21.1
Mixed 2	1/1	54.1/45.9	0.799	9.6×10^{-5}	1.88	23.9
Straight	1/1	50.7/49.3	0.849	2.7×10^{-4}	3.58	23.7
Pin	NA	73.5/26.5	0.232	NA	0.4	15.4

Gas bypassing between adjacent channels is seen in the regions of highest pressure difference (gas flows from an upstream leg of a channel to a downstream leg of the same channel though the porous media under the land of the bipolar plate). The maximum velocity is located within the middle of the gas channels. For HT-PEMFCs, modifying the position of the inlet and outlet or to design a gas distributor before entering the active area will lead to more uniform distribution [10].

Taccani et al. studied the effect of three flow field designs on performances of HT-PEMFCSs. The 5-step serpentine configuration is the best in terms of performance (power density) but with a higher pressure drop compared to 4-step serpentine and parallel designs [13]. F Liu et al. showed improved gas distribution with the spiral flow field design as shown in Figure 2-4a [14]. 3D CFD analysis of spiral flow field showed mixed flow compared to a plug flow for serpentine design with both the designs having 1 mm^2 of channel cross-sectional area and channel to land ratio of 1:1. The spiral geometry obtained higher cell voltage (40 mV) than the serpentine cell at a current density of 0.2 A cm^{-2}. Degradation rate with spiral design cell is 14 µV h^{-1} (5 times lower than serpentine) after 1000 h. The higher oxygen partial pressure drop between two adjacent flow channels in the spiral cell are the reasons for observed performance. This forces more oxygen permeating to the catalyst layer to reduce the mass transport limitation and to improve the kinetics of ORR. The dilution of PA due to enlarged water partial pressure is another effect of such pressure distribution. This reduces ohmic

resistance and improves kinetics of the cathode reaction. They concluded that the effect of higher water vapour partial pressure seems more dominant than the lower oxygen concentration in the spiral flow field. The ECSA after long term tests for the cell with the spiral flow field are 50 % higher compared to the serpentine flow field cell.

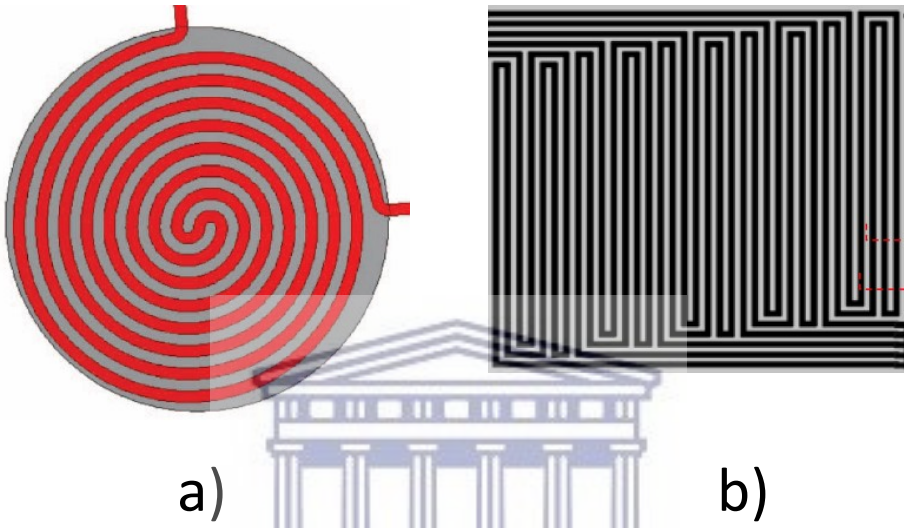

Figure 2-4 Flow field geometry a) spiral [14] andb) modified serpentine [15].

D Singdeo et al. developed a 3D CFD model to analyse the effectiveness of the modified serpentine (5 channels and 6 turns) on anode and cathode for HT-PEMFC application as shown in Figure 2-4b. The cross-sectional area of each channel is 1 mm^2 and thickness of rib is 1 mm. The simulation results demonstrated higher average current density (~22%) and better current density distribution (uniformity factor of 0.998) with modified serpentine geometry compared to serpentine flow fields (uniformity factor of 0.96) at 0.57 V. The major improvement is observed in the middle section of the flow-field for modified serpentine. Under similar conditions the pressure drop for modified serpentine (0.51 kPa at 0.59 LPM) is marginally higher than the conventional serpentine. The inlet and outlet regions showed higher and lower current density values respectively, similar to serpentine flow fields. But, in serpentine flow fields, the current density gradient closely follows the channel length along each turn from the inlet to the outlet section. In modified serpentine, the result indicates that if two adjacent reactant channels have a difference in reactant concentration, then cross-diffusion of gases is possible. This leads to better current density homogeneity and also higher current density values [15].

The influence of 4 step serpentine (mixed), pin, parallel and interdigitated flow field design on the performance of a HT-PEMFC is studied. A maximum power density up to 25% higher is obtained with serpentine or pin type designs using pure oxygen. Using air on the cathode side, the overall performance of the fuel cell gets worse due to the lower oxygen concentration. The wider flow channels lead to slightly higher power when the system is working under high reactant demand conditions, while deeper channels have apparently no effect. The performance with interdigitated flow channels is comparable to serpentine only at high flow rates, probably because convective flux is not needed for water removal at high operating temperatures. The pin type flow channels could be used with HT-PEMFC without expecting lower performance and pressure drop is the lowest, out of the four geometries tested in their work [16].

Flow fields also play a major role in heat dissipation and it is necessary to maintain uniform temperature distribution over the electrode area. The temperature distribution (experimental) is studied for serpentine channels used on anode and cathode and found that the temperature at the first half of the channel length remains more or less unchanged in comparison to the temperature near the inlet. Whereas the last half of the cell displays a more significant change in the temperature relatively to inlet which indicate that degradation is stronger in the last half of the channel length as more heat will be released. Higher temperature may also effect rate of phosphoric acid loss in the last half of channel and thereby ohmic resistance. The polarisation curve after the 700 h showed changing slope of curve and increase in activation losses [17]. For a multiple serpentine flow design, it is expected for current density to be highest at the inlet where the concentration of reactants is highest and decrease as gases moved towards the outlet. However, Aquino et al. noticed that the highest current density occurred at the first and fourth bends of the serpentine flow field and that current density is high in the middle of the plate and low at the gas inlet and outlet edges of the plate. With aging, it is observed that the high temperature peaks at the gas inlet and outlet edges of the plate where there is a large decrease in current density [18]. A 3D model of a HT-PEMFC having triple mixed serpentine flow channel geometry for a small active area of 25 cm^2 predicts temperature distribution along the channels. The current density is higher around cathode inlet so the temperature rise is more emphasized around cathode. The

difference in the temperature is 0.18 K for the operation voltage of 0.6 V (observed current density 0.224 A cm^{-2}) and this value is increased to 0.31 K for the operation voltage of 0.45 V (observed current density 0.313 A cm^{-2}) [19].

The current density distribution is strongly influenced by the structure of the flow field. G. Bandlamudiet al. studied 24 channel parallel serpentine flow field (divided into two blocks of 12 channels each) for HT-PEMFC of 300 cm^2 active area. A significant pressure difference exists in the region under each 180° bend from the pressure drop profiles in the porous media. As a consequence, gas bypasses the gas flow channels through the porous media. A high current density values observed at these locations due to higher gas concentration of the reactants in the regions close to the reaction layer. The oxygen mass fraction and the current density distribution show higher values towards the air inlet and lower values towards the air outlet. The decrease in oxygen mass fraction is almost linear in along the channel direction due to ongoing electrochemical reactions. The cathode side water mass fraction increases towards the outlet with slightly higher values observed under the land areas [20].

The influence of parameters such as flow channel aspect ratio on performance and manipulation of these parameters improves cell performance. At low operating voltages, a serpentine flow field with small rib and channel size (0.5 mm X 0.5 mm) would outperform parallel, interdigitated and Z-type flow fields; and could be further improved by utilizing channels of varying heights. Introduction of baffles improve the performance of various flow channel designs [21]. A 1D model has been developed for HT-PEMFC to optimize the flow channel dimensions. The optimal total width of a flow channel and its wall/rib as well as the ratio of a rib against total width, are investigated for higher power density. A relatively small total width and small rib-to-total width ratio are better for generating high power density in the fuel cell [22]. For very small channel dimensions, the manufacturing effort becomes unnecessarily high and the danger of channel clogging by water droplets is increasing. However, small dimensions are preferred for high current densities, whereas higher dimensions are better for low current densities [23]. Increasing land-to-channel ratio will increase the voltage loss. The co-flow or counter-flow does not matter if the anode presses against the cathode to enhance compression pressure and minimize deflection in the membrane [4].

2.1.2 Mass transport with different flow configurations

The purpose of flow fields on a bipolar plate is to provide uniform reactant distribution over the entire electrode surface area. In the case of LT-PEMFCs, liquid water is produced as a result of electrochemical reaction and it must be removed. So, the flow fields are designed for supplying fuel and oxidant to the fuel cell as well as channels for receiving liquid water and water vapour. But for HT-PEMFCs, no liquid water is present in the fuel cell as the cell is operated above 100^{o}C and as a result simplified water management and flow field design (no need to consider two phase flow) [24]. This is also confirmed from diagnostic studies by Y Zhu et al..The impedance related to diffusion of the HT-PEMFC stack is very small compared to conventional LT-PEMFC stack [25]. The flow field design configuration, dimensional parameters and aspect ratio impact the performance of fuel cell. The gas concentration for the straight flow pattern can be non-uniform, resulting in a local concentration polarization compared to serpentine design with well distributed gas concentration creating a better mass transfer phenomenon. The fuel cell with the serpentine flow channels show high pressure drop with best performance. A non-uniform distribution of oxygen mass fraction and local current density occur for the fuel cell with parallel flow channels with small manifolds (especially at low cell voltages). The fuel cell performance and durability can be significantly affected by the uniformity of the reactants within the fuel cell [26]. The triple mixed serpentine flow fields have non-uniform local current densities (increasing with decreasing operating fuel cell voltage) [19].

Lobato et al. confirmed from CFD studies of 4-step serpentine, parallel and pin-type have well defined current density profile [16]. The mass transfer processes have a very important effect on a fuel cell performance and flow channels are responsible to enable efficient energy and mass transport. The turbulent flow from serpentine channels may enhance mass transfer processes. The multiple channel serpentine, single serpentine, two channel serpentine and mixed serpentine are evaluated for performance. The results confirmed that the flow fields with narrow and long channels present a good performance at high gas flow rates because the convective mass transport in header manifolds is enhanced due to high flow rates. The performance decreases with the low flow rates because the ability to remove the produced water is greatly reduced. The

mixed flow fields showed resistance to flooding with a poor polarisation curve. So, the mixed design with long micro-channels should provide a good performance of PEMFC [3].

The interdigitated flow field can reduce the mass transport overpotential and reduce flooding on the cathode side [27]. On studying the polarisation curves for various channel sizes, for cell voltages higher than 0.7 V, the flow channel size has little effect on the cell performance because at high operating voltages the electrochemical reaction rates are low. As the operating cell voltage decreases, the channel size effect gradually increases as the mass transfer limitations strongly affect the cell performance. At the same operating voltage, the mean current densities increase with decreasing channel size. At 0.3 V, a large amount of liquid water is produced and when the excess liquid water is not properly removed but accumulates in the porous layers, the oxygen transport resistance significantly increases which reduces the mass transfer and the cell performance. As the channel size decreases the inlet velocity increases, which reduces the differences in the liquid water concentrations between the channels and ribs, and the maximum and minimum liquid water concentrations, indicating that the liquid water removal is enhanced. As the channel size decreases, the pressure drop increases. Larger pressure drops in the fuel cell mean that more power is needed to pump the reactants. The pressure drop is a significant issue to be considered in choosing the flow field designs in addition to the polarisation curve.

3D model studies of PEMFC for single serpentine flow field designs confirmed decrease of the flow channel and rib size lead to more uniform current density distributions between the flow channels and ribs. However, as the flow channel size decreases the cell performance increases to a maximum while the total pressure drop in the cell continues to increase.

When the rib and channel widths of flow fields are varied from 0.5 - 3 mm, narrower the rib width, the more improved the performance of the cell. In addition, the magnitude of improvement is larger at low voltage (indicating that the higher channel area portion is beneficial to the high power operation of a cell) [28].

In the case of spiral flow field, the flow crossover occurs, which forces a gas flow through the porous electrode under the land by means of convection. This accelerates the oxygen transport into the catalyst layer and compensates the depletion of reactant along the channel. As a result, the kinetic and mass transport resistances are reduced simultaneously [29].

Fuel cell with pin flow fields showed high power densities compared to parallel channel designs. This might be because that the pin type of flow field designs offer larger reactive area as well as enhanced mass transfer. However, a serpentine flow field is recommended by Liu et al. [30].

The interdigitated flow field outperformed the conventional one in terms of power and mass transport limitations especially at higher current densities. The interdigitated flow fields supply oxygen at a much higher rate through forced convection rather than diffusion [21].

The polarisation curves of the serpentine flow field showed the best performance followed by the Z-type and the parallel flow field. It is suggested that adding corner number, increasing flow channel length and decreasing the flow channel number to conventional flow fields enhance the cell performance by reducing the mass transport losses and increasing the limiting current density. Also, the crossover between adjacent flow channels enhances the mass transport of the reactant to the reaction site at the CL, which improves the performance of fuel cells with serpentine design. However, the GDL deformation from assembly compression reduces crossover and thus reduces cell performance which needs to be considered for PEMFC flow channel geometry optimization.

An optimized gas distribution is required in HT-PEMFC because the performance loss in a HT-PEMFC comes from the proton conductivity of the membrane and cathode. A small variation of water partial pressure results in a large change of the concentration of PA and variation of proton conductivity in the cell. A lower PA concentration due to higher water vapour partial pressure improves oxygen diffusion through PA to the active sites in the electrode. The dilution of PA results in a volume expansion of the acid. This

behaviour of PA might influence the ECSA and may also cause catalyst layer flooding [14].

Poor flow field design causes uneven flow distribution and high pressure leading to an uneven electrochemical reaction. The uneven electrochemical reaction can result in uneven heat and current production. An uneven heat production leads also to a heterogeneous distribution of temperature and thermal stress. Overall, within the cell it is the responsibility of the flow field design to provide a uniform concentration of gas reactants on the active area for a single cell and a reasonably low pressure drop between the inlet and outlet of the channels to minimize the parasitic power losses. The flow field needs to maintain enough membrane hydration over the entire active area to avoid dehydration of membrane.

2.2 HT-PEMFC degradation mechanisms

Fuel cells are being developed for variety of applications but till today they face challenges of limited life time which is major barrier to commercialization. In order to replace current technologies, fuel cells must meet requirements of U.S. Department of Energy (DOE) [31]. A target of 5000 hours (~150,000 miles of driving) and 40,000 hours for transportation application and stationary systems respectively (-40 - 40°C) with < 10 % performance loss. In order to meet these targets the HT-PEMFCs are being continuously developed in terms of design, materials and durability studied with different operating conditions both in-situ and ex-situ. In order to improve the life time of fuel cell it is quintessential to gain in depth understanding of failure modes and degradation mechanisms. Very few fuel cell systems have been demonstrated in the market with adequate long term performance with the cost and durability being major barriers [32]. Durability is defined as the ability of a fuel cell to resist to permanent changes in performance over the time. Researchers also study stability of fuel cell defined as the ability to recover power lost during continuous operation [33]. So it is necessary that the fuel cell systems meet durability targets. Durability is studied using accelerated stress test (AST) and long term operation.

AST is used to quantify the durability of a fuel cell with few tests in a short duration or limited time. A new material or design in development is tested to study its effects

or/and predict its degradation behaviour with operation time. In HT-PEMFCs, it is mainly used to understand degradation mechanisms and predict lifetime of components. A stress is carefully applied over fuel cell that will trigger specific or known degradation. There are no AST methods available specific to HT-PEMFCs. The AST used for LT-PEMFC are adapted for HT-PEMFC application. The protocol for the U.S. DRIVE for automotive propulsion applications is adapted for HT-PEMFC [34]. AST is performed as screening tests, mechanistic tests and lifetime tests. Screening tests are used to determine the performance and durability, relative to other design or product (such as membrane, catalyst, GDL and carbon support) of a fuel cell. The mechanistic tests determine the failure kinetics and pathways. The challenge of an AST is to choose operating parameters that trigger only a single degradation mode and minimizing all other degradation effects. But in reality this is not possible so characterization methods are used to check different degradation pathways. AST protocols to study membrane and catalyst layer degradation are shown in Table 2-2.

Table 2-2 General AST protocols for membrane and Catalyst Layer [35].

Component	Degradation mechanisms	AST stressors
Membrane degradation	Thermal and mechanical degradation	Temperature cycling/ relative humidity (RH) cycling
	Mechanical degradation	Load cycling/freeze-thaw cycling
	Chemical degradation	OCV and Fenton's test
Catalyst layer degradation	Pt oxidation	RH cycling
	Pt dissolution/agglomeration	Load cycling
		Potential control
		Temperature cycling
	Carbon corrosion	Cold-start-up
		Fuel starvation
		Potential control
		Start-up/shut-down cycles

The degradation mechanisms of HT-PEMFCs are not fully understood so durability and lifetime can be improved if the degradation modes and the respective mitigation strategies are understood. Degradation can happen during steady state or accelerated

test conditions. The degradation mechanisms of main components of HT-PEMFC are discussed below.

2.2.1 Membrane degradation

The MEA for HT-PEMFC is made of PBI membrane which is widely studied and successful commercially. Membrane degradation can seriously affect the durability of HT-PEMFC. During the long term operation the degradation of membrane is caused by 1) chemical oxidation, 2) mechanical and 3) thermal stress.

The chemical degradation mechanism for PEM is known to cause by the attack of the C-H bond in the polymer by hydrogen peroxide (H_2O_2) and its radicals (-OH or -OOH) generated during ORR in the cathode and the combination of hydrogen and oxygen in the anode. The H_2O_2 is generated when the O_2 from cathode permeate through the membrane and reduced at the anode according to the following reactions [36]:

$$H_2 + 2Pt \rightarrow 2Pt - H \quad \text{(eq. 2-1)}$$

$$2Pt - H + O_2 \rightarrow -OOH \quad \text{(eq. 2-2)}$$

$$-OOH + Pt - H \rightarrow H_2O_2 \quad \text{(eq. 2-3)}$$

The degradation of the PBI membrane in a life test due to the attack by HO- and HOO-radicals produced by the incomplete reduction of oxygen on the cathode side [37]. The chemical oxidative degradation mechanism of the PBI membrane under high temperature conditions is by the attack of peroxide radicals on H-containing end groups such as N-H bond in the imidazole ring that leads to the opening of imidazole ring and scission of the macromolecular chain [38]. The membrane degradation is known to alleviate in the presence of phosphoric acid, which has inhibiting effect on the decomposition of H_2O_2 [39].

The operation at OCV can enhance the MEA chemical degradation, especially that of the polymer membrane. H_2O_2 generated through incomplete ORR at the cathode or through the reaction of hydrogen and oxygen at the anode catalyst layer under OCV conditions can lead to the chemical decomposition of the polymer electrolyte membrane. The decomposition can then result in membrane thinning or even cracking and pinhole

formation in the membrane, increasing the gas crossover through the membrane, and thereby accelerating the formation of hydrogen peroxide. Qi et al. investigated the impact of OCV on the performance and degradation of a PBI-based HT-PEMFC. The OCV of the fuel cell increased in the first 35 min and declined thereafter. Their EIS results showed significant catalyst activity loss and increase in mass transport loss, and the size of cathode platinum particles increased by 430 % during the test [40].

The degradation of the PBI membrane with applied torque when a MEA is compressed between bipolar plates could cause membrane deformation (membrane creep and micro-crack fracture) that can lead to membrane thinning or pinhole formation which can further accelerate the chemical oxidative degradation of the PBI membrane. The swelling and shrinking of membrane during load cycling or RH cycling could cause mechanical stress. PBI membranes have excellent mechanical strength but doping with PA compromises the mechanical strength. Alternatively, cross-linked PBI membranes with better chemical and mechanical stability can be used. However, the cross-linking affects thermal stability at high temperature. PBI membrane does not show significant thermal degradation in the temperature range 140-180^{o}C. But PBI membranes are doped with PA, is dehydrated to polyphosphoric acid leading to decrease in proton conductivity [41]. The self-dehydration of phosphoric acid in the range 150-175^{o}C is very rapid [42]. Membrane dehydration is expected to be much slower under the operating condition of an HT-PEM fuel cell due to the protection of gas diffusion layer and production of water by electrochemical reaction. Hydrogen crossover rate is measured to check membrane degradation. The hydrogen crossover rate is increased by a factor of 14 at the end of the durability test because of the local thinning or pinhole formation in the membrane [43].

2.2.2 Catalyst layer degradation

During long term operation, the platinum nanoparticles tend to grow in size resulting in decrease of ECSA and fuel cell performance. The degradation mechanisms of the HT-PEMFC catalyst layer are similar to those of LT-PEMFCs. The mechanisms responsible for loss of ECSA are discussed below [44]:

- The dissolution of platinum nanoparticles into platinum ions and then re-deposition on existing Pt nanoparticles resulting in particles with larger diameter.
- The dissolved nanoparticles migrate to other parts of the MEA and are not accessible to reactant gases. The process of dissolution, migration and re-precipitation of the platinum particles leads to platinum particle growth known as Ostwald ripening.
- Sintering of adjacent nanoparticles to form bigger particles known as platinum agglomeration which is common and faster when the particle size is small because of high Gibbs free energy and one of the cause for early or pre-mature performance loss.
- Diffusion of platinum ions and precipitation in the membrane via reduction of platinum ions.

The carbon support corrosion also could lead to detachment of platinum particles and loss of electrochemical surface area.

2.2.3 Carbon support corrosion

In HT-PEMFCs, high surface area carbon is used as a support material for platinum catalyst. Carbon support corrosion happens via reaction mentioned in Equation 2-4 with an equilibrium potential 0.207 V in acidic environment [45, 46].

$$C + 2H_2O \rightarrow CO_2 + 4H^+ + 4e^- \qquad E = 0.207\ \text{V vs NHE} \quad \text{(eq. 2-4)}$$

Carbon support corrosion could lead to ECSA loss due to

- The detachment of platinum particles from the surface of carbon resulting in agglomeration of platinum particles
- The mass loss and reduction of catalyst layer thickness during long term operation
- The decrease in hydrophobicity of the carbon surface due to oxidation of carbon support and thereby increase in mass transfer losses if electrode flooded by doping acid.

In severe cases, the deterioration of carbon support structure and the concomitant increase of the contact resistance (ohmic resistance) of the fuel cell. Carbon corrosion is enhanced by high operating temperature because of kinetics. HT-PEMFC (non-humidified) showed more pronounced corrosion rates than LT-PEMFC with fully humidified condition [47]. Various support materials have been investigated to find suitable support material with better corrosion resistance. The graphitized carbon black showed better stability and longer catalyst durability compared to Vulcan carbon black and multi-walled carbon nanotubes. They confirmed that to improve the stability of the catalyst support, porous carbon can be graphitized through high temperature heat treatment [48]. The Pt catalyst catalyses carbon corrosion and lower platinum loading proved lower carbon corrosion rates. Additionally, Start/stop cycling increases carbon corrosion and fuel starvation [49].

During start-up/shut-down process of HT-PEMFC, carbon corrosion can happen in the catalyst layer caused by the formation of H_2/ air interface in the anode. During a fuel cell shut-down, air can reach the anode of a fuel cell from the anode exhaust or across the membrane from the cathode. During start-up, H_2 is passed through the anode and H_2/air boundary is formed on the anode side. In these conditions, oxygen reduction occurs on the cathode and the anode side of fuel cell, resulting in a higher potential at the cathode, which in turn results in reverse current. The carbon support corrosion can happen under these conditions. Schmidt et al. performed 240 start/stop cycles on HT-MEA for more than 6000 h [50]. The degradation rate is twice compared to MEA operated in steady-state. MEA from two tests showed similar ohmic resistance and activation overpotential whereas cathode mass transport losses are enhanced under start/stop cycling. The increase in mass transport losses correspond to increase in carbon corrosion. Hartnig et al. studied the stability and degradation of the cathode catalysts such as Pt/Vulcan XC72, Pt-alloy/Vulcan XC72 and Pt-alloy supported on a corrosion-stabilized carbon [51]. They found that 1) kinetic losses for Pt-alloy electrodes are almost identical and significantly lower than on the pure Pt catalyst electrode; 2) mass transport losses on the Vulcan XC72 supported catalysts are identical and significantly higher than mass transport losses on the electrodes using the stabilized carbon catalyst support; 3) the increase of mass transport overpotential is a clear

function of amount of oxidized carbon from the catalyst support. Engl Tom et al. observed significant increase in anode overpotential after start-up/shut-down test, confirming carbon corrosion on the anode side of an HT-PEMFC [52]. The Pt-alloy with a corrosion stabilized carbon support are resistant to degradation under start-stop cycling.

2.2.4 Phosphoric acid leaching

PA plays important role in proton conductivity and thus enhance fuel cell performance. However, the free mobile PA molecules migrate from the membrane and the catalyst layer to GDL and flow fields because of cell compression and operational parameters (load cycling, high flow rates and long term operation) resulting in exit of some of the acid. The PA leaching rate is enhanced by high operating temperature and high current density [53]. The PA loss mechanisms in HT-PEMFC's are discussed

- The removal of excess PA in the BoL
- The PA migration due to load cycling
- The squeezing out of PA and acid uptake of flow plates
- The dilution effect at high RH

PA loss occur in the BoL due to the removal of the excess PA in the MEA. The consequence of PA loss is decrease in proton conductivity resulting in performance loss over time. PA loss has significant influence on the fuel cell life time [54]. The excess PA in the MEA can be trapped in the flow field plates and cause solid material build-up during fuel cell operation, which can cause mass transport loss [55]. The graphite bipolar plates exhibit high PA uptake from the MEA during fuel cell operation, which leads to acid loss [56]. The load cycling results in a much higher acid loss rate than constant load operation [57]. The start/stop cycling only slightly increased the PA loss compared to constant load operation [58]. They also performed a short-term water-stress test, in which both anode and cathode gases are humidified to the dew point temperature of 70^0C. In 90 h they saw PA loss of the same order of magnitude as that caused by constant load operation in 4600 h. Oono et al. observed that PA distribution in the electrodes becomes more and more non-uniform during the lifetime test and the performance decreases [59]. Maier et al. used synchrotron X-ray imaging of an HT-PEM fuel cell under dynamic operating conditions and observed that the increase in current

density can result in a reversible PA electrolyte dilution and membrane swelling [60]. Eberhardt et al. investigated PA redistribution during operation by using synchrotron based X-ray tomographic microscopy, and they observed migration of PA from cathode to anode at high current density and flooding of PA in the anode gas diffusion layer and flow channels [61].

2.2.5 Degradation studies specific to HT-PEMFCs

The degradation mechanisms of HT-PEMFCs are studied in numerous works and some of the major findings are: The high potentials on cathode makes cathode catalyst more vulnerable to particle size growth compared to anode catalyst [62]. The degradation of catalyst layer is enhanced by higher operating temperature especially, the kinetics for platinum dissolution, migration, agglomeration and detachment of Pt particles. Carbon support corrosion is also enhanced at high temperatures. Higher operating temperatures cause decrease in ECSA because of increase in Pt particle size [63]. The performance loss and durability is found to be much larger under load cycling conditions than under constant load conditions and start/stop conditions [64, 65]. The load cycling and start/stop cycling conditions cause accelerated CL degradation with severe carbon support corrosion.

Premature performance loss in early stage of fuel cell life is due to catalyst degradation [66]. The increase in particle size mainly occurred in the first 300 h of operation and it remained almost unchanged over the next 200 h supported by rapid performance loss in the first 300 h and a gradual decrease thereafter until 500 h. The same behaviour is reported Oono et al. in a long term study. At the BoL, the platinum nanoparticles (<= 2-3 nm) are well scattered on the surface of carbon support. Smaller particles have higher Gibbs free energy so platinum particles tend to agglomerate. As the particle grows in size the and lower the Gibbs free energy the agglomeration is also less severe so, slower performance loss at later stages of the life. The agglomeration of the Pt/C catalysts, the physical degradation of the PBI membrane and the leaching of PA from the PBI membrane are the major reasons for the performance degradation of the PA doped PBI based HT-PEMFC. Table 2-3 lists few degradation mechanisms with operating conditions.

Table 2-3 Degradation mechanisms of HT-PEMFC along with operating conditions.

Degradation mechanism	Operation conditions	References
Carbon corrosion	0.650, 0.700 V and OCV at 120, 140, 160^{o}C	A Kannan 2018[67]
Acid loss, life time	T = 160, 180^{o}C; i = 0.2, 0.6, 0.8 A cm^{-2}	T Sondergaard 2018 [68]
Acid loss, life time	0.2 - 0.8 A cm^{-2}	S Thomas 2017 [64]
Catalyst degradation (dissolution)	0.6 - 1.0 V , Humidity square wave	T Sondergaard 2017 [69]
Acid loss, ECSA loss	Load cycling square wave	Schonvogel, Dana 2016 [70]
ECSA loss	Load cycling triangular	R Taccani 2017 [65]
PA loss	Constant load with high current interruption	U Reimer 2014 [71]
Electrolyte evaporation	190°C, 0.2 A cm^{-2}	S H Eberhardt 2015 ECS [61]
Membrane thinning	0.24 A cm^{-2}, 17000 h	R Kerr 2015 [72]

2.3 Characterization methods

It is very important to characterize the HT-MEA for performance and understand the cause for performance losses and degradation with aging. Understanding the cause for performance degradation of HT-PEM fuel cell requires knowledge of various characterization methods. The current section details the literature related to characterization methods used for PA doped PBI based HT-PEMFC and Table 2-4 shows the summary of characterization techniques used to accomplish thesis and purpose. The degradation mechanisms can be understood and the long term durability can be improved with the aid of characterization methods.

Table 2-4 Summary of characterization methods for HT-PEMFC (Partly adopted from [73]).

Type	Techniques used	Purpose
In-situ	Polarisation curves	Current voltage relationship and voltage losses
	Tafel analysis	Activation losses
	Electrochemical impedance spectroscopy	Individual losses of cell or resistance
	Cyclic voltammetry	Electrochemical surface area of catalyst
	Linear sweep voltammetry	Hydrogen cross over
	FT-IR	Carbon dioxide measurement
Ex-situ	Transmission electron microscopy	Catalyst particle size and distribution
	Scanning electron microscopy	Thickness of MEA layers
	X-ray diffraction	Crystallite size
	Energy dispersive spectroscopy	Elemental composition
	Inductively coupled plasma-optical emission spectroscopy	Platinum and phosphorous estimation

2.3.1 Polarisation curves

When fuel cell is operated with hydrogen and air on anode and cathode, respectively a voltage ≥ 0.9 V is recorded under no load condition called OCV. This voltage is lower than the ideal potential, E^0 predicted by Nernest equation. The real fuel cell voltage, E_{cell} when operated in load condition (with drawing currents), the voltage observed is lower than the expected as can be seen from Figure 2-5 called polarisation curve and is contributed by three losses or overpotentials 1) activation losses, η_{act} 2) ohmic losses, η_{iR} 3) mass transport losses, η_{mt}. The real fuel cell voltage is given by Equation 2-5.

$$E_{cell} = E^0 - \eta_{act} - \eta_{iR} - \eta_{mt} \quad \text{(eq. 2-5)}$$

For HT-PEMFCs, the significance of the internal current decreases because exchange current density i_0 is quite high. The crossover current is very small for this kind of fuel cells.

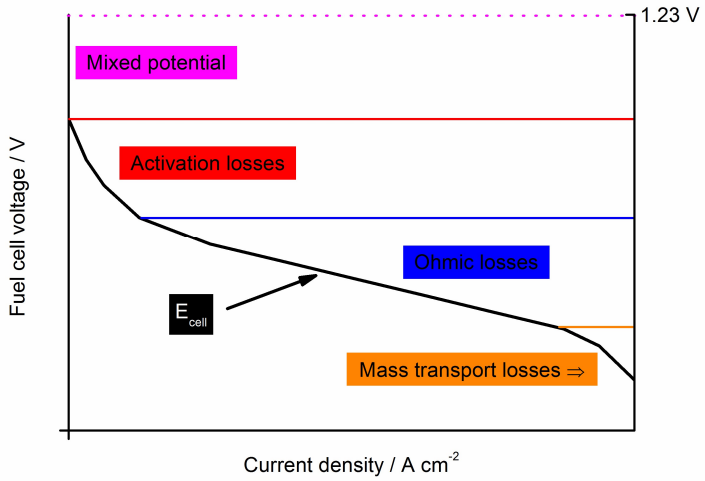

Figure 2-5 Polarisation curve showing various losses.

The following regions are highlighted from polarisation curve or I-V curve. Mixed potential region: The membrane used in the fuel cell is expected to be impermeable to hydrogen and oxygen but in reality there is some hydrogen crossing this barrier and mixing with oxygen on the cathode side resulting in reduced OCV. These are called mixed potentials generated by various processes like gas crossover, reduction of oxygen to hydrogen peroxide, oxidation of carbon and platinum. Activation overpotential region: When current is drawn from fuel cell, a charge transfer overpotential occurs in reaction kinetics on each electrode. Ohmic overpotential region or the ohmic losses: This is contributed by resistance of bipolar plates, gas diffusion layers and electrode material. The contact resistance is also part of ohmic losses but its contributions are minimum if all the components of fuel cell are in good contact. The resistance to conduction of ions or protons through the membrane has major contribution to ohmic overpotential. Mass transport overpotential: When the diffusion of reactants form gas channels to active catalyst sites is hindered, mass transport overpotentials dominate. Current limiting behaviour is observed at high current densities due to mass transport losses. When air is used as reactant, the diffusion of oxygen in the air becomes a limiting factor on the cathode side. Also when reformate is used as reactant on anode side, the presence of CO will effect mass transport losses with increasing current densities. Mass transport losses for HT-PEMFC, can exist because of phosphoric acid flooding in catalyst layer making diffusion of reactants difficult.

2.3.2 Electrochemical impedance spectroscopy

Electrochemical impedance spectroscopy (EIS) has been used for study and control of fuel cell diagnostics. In HT-PEMFC, it has been used to study the effect of phosphoric acid doping level in PBI membrane and Pt catalyst wt%, influence of CO and CO_2 in the fuel and its influence on the MEA performance, novel bipolar plate materials and designs, flow field design analysis [74], optimization of material properties of gaskets and compression force for fuel cell stacks, the effect of anode humidification and cathode gas stoichiometry, performance of fuel cell in wide temperature ranges. The effect of current density, operating temperature, gas stoichiometry on impedance spectra of HT-PEM unit cell is studied by J L Jespersen et al. [75]. EIS is used to identify early failure of fuel cell components like bipolar plate corrosion, catalyst agglomeration, membrane degradation, carbon support oxidation. Degradation mechanisms of fuel cell can be evaluated using EIS studies. The membrane degradation and charge transfer resistance with aging [76], carbon/catalyst degradation, reactant starvation, acid leaching and CO poisoning in HT-PEMFC are studied with EIS spectra fitted with electrochemical equivalent circuit (EEC) [77].

EIS measurements are conducted using a potentiostat or load box in conjunction with a frequency response analyser (FRA). The fuel cell is perturbed using current/voltage perturbation then recording the voltage/current response from the system respectively. For a current control measurement, when the leads are all connected the electrical load is set to a DC constant current. The FRA will generate an AC current perturbation and interrupt the fuel cell through a load bank. The response to the interruption from the fuel cell will enter into the FRA for analysis to obtain the AC impedance spectra. The FRA has four probes out of which two are used for current or voltage signal generation and the other two for receiving the voltage or current response. The response voltage divided by the perturbation current is the complex impedance at that frequency. This procedure is repeated for set of desired frequencies giving rise to a full impedance spectrum which is plotted as Nyquist (imaginary component, -Z" against real component, Z') and Bode (phase angle, θ against frequency /absolute impedance, |Z| against frequency) diagrams [78].

The three main polarisation losses observed in I-V curve could be separated and quantified like charge transfer resistance or kinetic losses, ohmic losses and mass transport losses. These physicochemical processes occurring at different frequencies within the fuel cell are fitted using EEC using a network of inductors, resistors and capacitors and important parameters can be obtained which can be used to optimise fuel cell components and operating conditions thereby performance can be optimised [79].

A typical Nyquist plot of HT-PEMFC is shown in Figure 2-6. The three semicircles are observed and represented as high frequency (HF), intermediate frequency (IF) and low frequency (LF) semi-circle appearing at 100, 10 and 1 Hz respectively depending on the frequency at which they appear. More details concerning components of EEC and associated processes are mentioned in section 4.2.1.

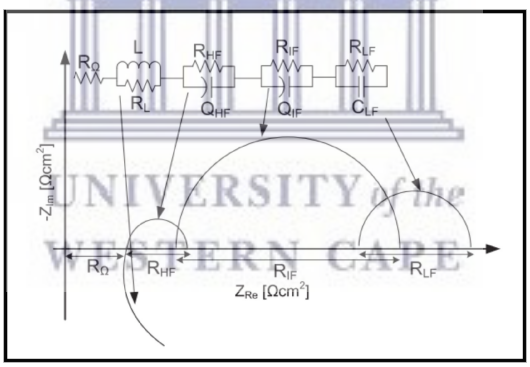

Figure 2-6 EEC used to fit the Nyquist plot of HT-PEMFC [80].

2.3.3 Cyclic voltammetry

Cyclic voltammetry (CV) is conducted to study the ECSA of platinum responsible for electrochemical reactions. In CV, the potential of fuel cell is scanned in a cyclic form from 0.05 to 1.2 V and back (which looks like a triangular wave form when applied voltage vs. time is plotted). The typical CV curve of HT-PEMFC is shown in Figure 2-7 with hydrogen and double layer regime. When cathode is scanned with more positive potentials, oxidation of hydrogen takes place and hydrogen reduction in the reverse direction towards negative voltages. The CV curve has desorption peak (peaks with positive current) and adsorption peak (peaks with negative current) in the voltage range

0.05 - 0.4 V followed by double layer regime. Potentiostat is required to perform voltammetry experiments. Data is recorded current vs. voltage which is equivalent to recording current vs. time.

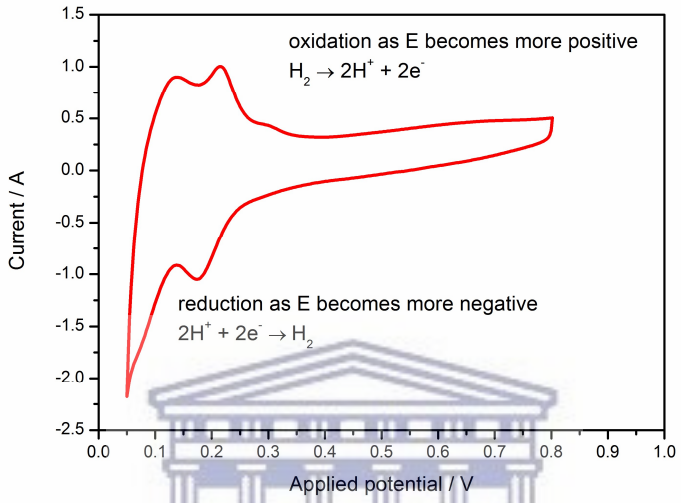

Figure 2-7 Typical CV curve of HT-PEMFC.

ECSA can be calculated from integration of hydrogen adsorption or desorption peaks. The integral for peaks is according to Equation 2-6, where i represents the measure current, and i_{DL} is the current due to the double layer charging [81].

$$A_d = Q_H = \int_{0.05}^{0.4} (i - i_{DL})\, dV \qquad \text{(eq. 2-6)}$$

Where Q_H is charge estimated by integration of the current in the voltammogram in the hydrogen adsorption or desorption domain. Using the integral value, the ECSA of the cathode electrode is estimated based on the relationship between the hydrogen adsorption/desorption area of the electrode (integrated area) and the hydrogen adsorption charge on a smooth Pt electrode (210 µC cm^{-2}-Pt) according to Equation 2-7.

$$ECSA = \frac{\text{integrated area (AV) (obtained from CV curve)}}{\text{scan rate}\left(\frac{mV}{s}\right) * \text{Pt loading}\left(\frac{mg}{cm^2}\right) * 210\ \left(\frac{\mu C}{cm^2 - Pt}\right)} \qquad \text{(eq. 2-7)}$$

The ECSA is in $m^2\ g^{-1}$, where integrated area of the hydrogen adsorption/desorption peak from the CV curve is in units of AV). The ECSA depends on the structural integrity of the CL and also the distribution of PA in the CL. Thin CL with lower Pt loadings result in

higher Pt utilization in comparison to thick CL with low acid distribution from the membrane leading to reduced triple-phase boundaries.

2.3.4 Linear sweep voltammetry

Linear sweep voltammetry (LSV) is a method similar to CV with only forward scan (potential is linearly varied with time) and no reverse scan. The method is used to determine the hydrogen crossover through the membrane from anode to cathode and also the internal short-circuit resistance. Hydrogen crossover may lead to fuel inefficiency and in extreme cases heat and water generation by combining with oxygen at cathode. As mentioned earlier in section of polarisation curves that hydrogen crossover results in cell voltage losses (such as OCV). The hydrogen present at the cathode is oxidized under mass transfer limiting conditions in a linear potential scan with a small sweep potential rate (2-4 mV s^{-1}) from the rest potential to 0.5 V are common. The current density increases in a linear fashion with increase of applied potential indicates the development of an internal short-circuit resistance in a fuel cell. The inverse of the potential vs. current density slope (where linear relation between current density and potential is observed) gives internal short circuit resistance values. Then LSV curve is corrected for hydrogen crossover estimation by subtracting the short-circuit current from total current [82].

2.3.5 Infrared spectroscopy

Fourier transform infrared spectroscopy (FT-IR) can be used for solid, liquid and gas samples. Within the infrared region of the spectrum, for a molecule with functional groups have specific absorption frequencies if it is infrared active because of molecular vibrations. The infrared region ranges from wave number (reciprocal of wavelength) of 625 – 4000 cm^{-1}. The FT-IR spectrometers consists of a parallel polychromatic radiation from an IR source is directed to an interferometer. The modulated beam is reflected through the gas sample cell. Finally, the detector detects the intensity of the infrared beam. The detected signal is digitized and Fourier transformed by the computer resulting in an IR spectrum of the sample gas. The IR spectrum of sample generally consists of the transmission of the infrared radiation through the sample as a function of wavelength. The transmittance, T is the intensity of the infrared radiation that has

passed through the sample, I divided by the intensity of the infrared radiation that has entered the sample gas, I_0 as shown in Equation 2-8:

$$T = \left(\frac{I}{I_0}\right) \text{ (eq. 2-8)}$$

T = 1 or 100 % when there is no absorption. The absorbance scale is used to represents the absorption of the infrared radiation because absorbance, A is directly proportional to the thickness of the sample gas (absorption path length) and the concentration of the sample gas. Absorbance is obtained according to Equation 2-9:

$$A = \log_{10}\frac{1}{T} \text{ (eq. 2-9)}$$

The Beer-Lambert law is used for spectroscopic analysis of sample as shown in Equation 2-10. The law states that the absorbance is directly proportional to the concentration of the sample gas at a given wavelength for constant optical path length. Since Beer's law is additive, the total absorbance is equal to the sum of the absorbance of each gas component.

$$\log(I_0/I) = \log(1/T) = A = abc \text{ (eq. 2-10)}$$

Where I_0 is intensity of infrared radiation entering the sample, I is intensity of infrared radiation that has passed through the sample, T transmittance, A is absorbance, a is absorptivity (The value of 'a' varies from a molecule to molecule as a function of wavelength, but is constant for a given molecule at a given wavelength), b is optical path length (the distance the infrared radiation beam traverses in the gas sample) and c is sample concentration (of sample molecules in sample). In reality, changes in sample gas temperature or pressure in the sample cell will affect the measurements (sample concentration and shape of the IR spectrum).

2.3.6 Inductively coupled plasma Spectroscopy

Inductively coupled plasma optical emission spectrometer (ICP-OES) operate by decomposing a liquid sample by intense heat into a cloud of hot gases with an inductive coupled plasma (a state of matter containing electrons and ionised atoms of Argon). The plasma reaches temperatures of around 10000°C. ICP-OES is solution-based analytical

technique. Solid sample can be used with prior grinding and dissolving. This is used for determination of elements from soil, water etc. ICP-OES can analyse a wide range of elements simultaneously. However spectral interference between different elements cannot be eliminated. The wavelength of one element's light emission can sometimes be close enough to that of another element to cause problems [83].

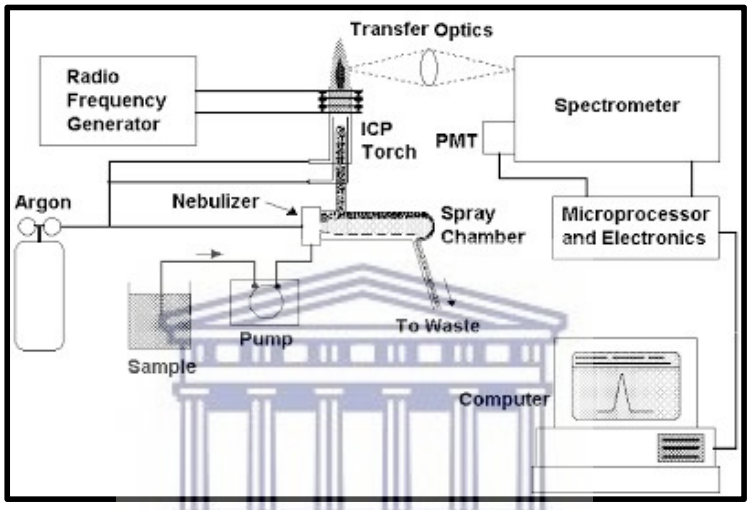

Figure 2-8 Schematic and components of ICP-OES [84].

The sample to be analysed is pumped via a peristaltic pump though a nebulizer. The nebulizer produces spray (aerosol) is lead into argon plasma from the spray chamber. The plasma is generated at the end of a quarts torch by a cooled induction coil (RF coil). Within the torch segment the sample goes through desolvation, atomization and ionization.AC current with high frequency flows through the RF coil, as a result, an alternate magnetic field is induced which accelerates electrons into a circular trajectory. The plasma with 6000-7000 K is generated when the collision between Argon atom and electrons happen. The electrons get excited and reach to higher energy level. When these exited electrons reach to ground level energy is liberated as photons (light). The intensity of light on the wavelength is measured and with the calibration calculated into a concentration. Every element has its own characteristic emission spectrum measured using a spectrometer.

2.3.7 Scanning electron microscopy

The scanning electron microscope (SEM) is used to take images of a sample by scanning it with a high energy beam of electrons. These electrons interact with the atoms producing signals that contain information related to the surface topography, composition, and thickness. A beam of electrons (0.5 - 40 keV) are emitted from an electron gun fitted with a tungsten filament cathode. The electrons pass through electron column and in the final lens, which deflect the beam in the x and y axes and scans over a rectangular area of the sample surface.

When the primary electron beam interacts with the sample, the electrons loses energy by repeated random scattering and absorption within a teardrop-shaped volume of the specimen known as the interaction volume, which extends from less than 100 nm to around 5 µm into the surface. The size of the interaction volume depends on the electron's landing energy, the atomic number of the specimen and the specimen's density. The energy exchange between the electron beam and the sample results in the reflection of high-energy electrons by elastic scattering, emission of secondary electrons by inelastic scattering and the emission of electromagnetic radiation, each of which can be detected by specialized detectors. The beam current absorbed by the specimen can also be detected and used to create images of the distribution of specimen current. Electronic amplifiers of various types are used to amplify the signals which are displayed as variations in brightness on a cathode ray tube. The raster scanning of the CRT display is synchronised with that of the beam on the specimen in the microscope, and the resulting image is therefore a distribution map of the intensity of the signal being emitted from the scanned area of the specimen.

2.3.8 Transmission electron microscopy

Transmission electron microscopes (TEM) employ a beam of highly energetic electrons to provide information at nano-scale. These techniques allow morphological investigations of the samples as well as the analysis of their composition. TEM can achieve resolutions of more than 1 nm. TEM is able to examine the nano-scale structure, composition and other properties of a sample. In TEM the electron beam is passed through the sample and the transmitted electrons are detected. The interaction

between the electron beam and the atoms of the sample emits several types of radiation, including secondary electrons coming from the sample itself, backscattered electrons of the beam that bounce off the nuclei of atoms in the sample, beam electrons that are transmitted through the sample, X- rays, light and heat. X-rays are emitted when an electron from the core level of an atom leaves a vacancy that can be filled by an electron from a higher energy level. This radiation can be used to investigate the composition of the volume penetrated by the electron beam since the energy gap between electron levels is specific of a particular atom. Energy dispersive x-ray analysis (EDX) can determine the composition of the sample surface by means of a special detector that detects this radiation and is often installed in combination with SEM or TEM. There is a limitation on the sample thickness in the TEM experimental set-up, since it has to be lower than 300 Å and even lower than 50 Å for the high-resolution TEM. The interaction between the electron beam and the atomic structure of the sample results in a phase contrast from which it is possible to assemble the image. The transmitted electrons are deflected by proper electromagnetic lenses that deviates their trajectories converging them in a single focus point. The resulting image is obtained by differential contrast between the electrons investing the sample and the transmitted electrons focused on the detector. TEM has been widely used to investigate nanoparticles in catalyst layer of PEM fuel cell.

2.3.9 X-ray diffraction

X-ray diffraction (XRD) is used to analyse powder and crystal samples. It is widely used for the phase identification of crystalline compounds especially in materials research and development. X-ray diffraction technique is based on constructive interference of monochromatic X-rays and a crystalline sample. The X-rays are generated by a cathode ray tube and directed toward the sample. The interaction of the incident rays with the sample produces constructive interference (and a diffracted ray) when conditions satisfy Bragg's equation the X-rays scattered by the atoms in the plane of a periodic structure are in phase and diffraction occurs in the direction defined by the angle θ in Equation 2-11:

$$n\lambda = 2d \sin \theta \quad \text{(eq. 2-11)}$$

Where n is an integer, λ is the characteristic wavelength of the X-rays impinging on the crystallize sample, d is the interplanar spacing between rows of atoms and θ is the angle of the X-ray beam with respect to these planes.

This law relates the wavelength of electromagnetic radiation to the diffraction angle and the lattice spacing in a crystalline sample. These diffracted X-rays are then detected, processed and counted. By scanning the sample through a range of 2θ angles, all possible diffraction directions of the lattice should be attained due to the random orientation of the powdered material. Conversion of the diffraction peaks to d-spacings allows identification of the mineral because each mineral has a set of unique d-spacings like a fingerprint (achieved by comparison of d-spacings with standard reference patterns). An important parameter in XRD is the angle between the incident and diffracted rays.

Copper is the most common target material for single-crystal diffraction, with CuKα radiation = 1.5418 Å. These X-rays are collimated and directed onto the sample. As the sample and detector are rotated, the intensity of the reflected X-rays is recorded. When the geometry of the incident X-rays impinging the sample satisfies the Bragg Equation, constructive interference occurs and a peak in intensity occurs. A detector records and processes this X-ray signal and converts the signal to a count rate which is then output to a device such as a printer or computer monitor. The geometry of an X-ray diffractometer is such that the sample rotates in the path of the collimated X-ray beam at an angle θ while the X-ray detector is mounted on an arm to collect the diffracted X-rays and rotates at an angle of 2θ. The instrument used to maintain the angle and rotate the sample is termed a goniometer. Results are commonly presented as peak positions at 2θ and X-ray counts (intensity) in the form of an x-y plot. Intensity (I) is either reported as peak height intensity, that intensity above background, or as integrated intensity, the area under the peak. The relative intensity is recorded as the ratio of the peak intensity to that of the most intense peak [85].

References

[1] Wang JY. Barriers of scaling-up fuel cells: cost, durability and reliability. Energy 2015; 80: 509–21.

[2] Guo H, Wang MH, Liu JX, Nie ZH, Ye F, Ma CF. Temperature distribution on anodic surface of membrane electrode assembly in proton exchange membrane fuel cell with interdigitated flow bed. Journal of Power Sources 2015; 273:775–83].

[3] J Wang. Theory and practice of flow field designs for fuel cell scaling-up: A critical review. Applied energy 2015; 157:640-663].

[4] H Kahraman, M F Orhan. Flow field bipolar plates in a proton exchange membrane fuel cell: Analysis & modelling. Energy Conversion and Management 2017; 133:363-384.

[5] Wang JY, Wang HL. Flow field designs of bipolar plates in PEM fuel cells: theory and applications. Fuel cells 2012; 12 (6):989–1003.

[6] Wang JY, Wang HL. Discrete approach for flow-field designs of parallel channel configurations in fuel cells. International Journal of Hydrogen Energy 2012; 37 (14):10881–97.

[7] Kumar A, Reddy RG. Effect of gas flow-field design in the bipolar/end plates on the steady and transient state performance of polymer electrolyte membrane fuel cells. Journal of Power Sources 2006; 155:264–71.

[8] B Tsai, C Tseng, Z Liu, C Wang, C Lee, C-C Yang, S-K Lo. Effects of flow field design on the performance of a PEM fuel cell with metal foam as the flow distributor. International Journal of Hydrogen Energy 2012; 37(17)13060-13066.

[9] P Choopanya, Z Yang. Transient Performance Investigation of Different Flow-field Designs of Automotive Polymer Electrolyte Membrane Fuel Cell (PEMFC) Using Computational Fluid Dynamics (CFD). 10th International Conference on Heat Transfer, Fluid Mechanics and Thermodynamics, 14-16 July, 2014; 583-592.

[10] C. Siegel, G. Bandlamudi, N. Van Der Schoot, and A. Heinzel, “Large Scale 3D Flow Distribution Analysis in HTPEM Fuel Cells,” Excerpt from Proc. COMSOL Conf. 2009, no. 1, 2009.

[11] T Sousa, M Mamlouk, C M Rangel, K Scott. Three dimensional model of a high temperature PEMFC using PBI doped phosphoric acid membranes. Study of the flow field effect on performance. Advanced Hydrogen Energy Technology 2012; 12(4);566-576.

[12] D G Caglayan, B Sezgin, Y Devrim, I Eroglu. Three-dimensional modeling of a high temperature polymer electrolyte membrane fuel cell at different operation temperatures. International Journal of Hydrogen Energy 2016; 41(23)10060–10070.

[13] Taccani R, Zuliani N. Effect of flow field design on performances of high temperature PEM fuel cells: experimental analysis. International Journal of Hydrogen Energy 2011; 36(16):10282–10287.

[14] F Liu, M Kvesic, K Wippermann, U Reimer, W Lehnert. Performance and Durability of HT-PEFCs with Customized Flow Field. ECS Transactions 2012; 50(2)681–689.

[15] D Singdeo, T Dey, S Gaikwad, S Juhl, P C Ghosh. A new modified-serpentine flow field for application in high temperature polymer electrolyte fuel cell. Applied Energy 2017; 195:13-22.

[16] J Lobato, P Canizares, M A Rodrigo, F J Pinar, E Mena, D U´ beda. Three-dimensional model of a 50 cm2 high temperature PEM fuel cell. Study of the flow channel geometry influence. International Journal of Hydrogen Energy 2010; 35(11)5510–5520.

[17] J Lebæk, S T Ali, P Møller, C Mathiasen, L P Nielsen, S K Kær. Quantification of in situ temperature measurements on a PBI-based high temperature PEMFC unit cell. International Journal of Hydrogen Energy 2010; 35(18)9943–9953.

[18] A Aquino J Heng. Current and Temperature Distributions in a PEM Fuel Cell 2017.

[19] D G Caglayan, B Sezgin, Y Devrim, I Eroglu. Three-dimensional non-isothermal model development of high temperature PEM Fuel Cells. International Journal of Hydrogen Energy 2018; 43(23)10834–10841.

[20] G Bandlamudi, C Siegel, C Heßke, AHeinzel. Fluid Flow and Current Density Distribution in Large-Area HT PEMFCs. Proceeding of the COMSOL Conference 2011.

[21] A Aiyejina, M K S Sastry. PEMFC Flow Channel Geometry Optimization: A Review. Journal of Fuel Cell Science and Technology 2012; 9(1)011011-24.

[22] H Liu, P Li, AHartz, K Wang. Effects of geometry/dimensions of gas flow channels and operating conditions on high-temperature PEM fuel cells. International Journal of Energy and Environmental Engineering 2015; 6(1)75–89.

[23] J Scholta, G Escher, W Zhang, W Lehnert. Investigation on the influence of channel geometries on PEMFC performance. Journal of Power Sources 2006; 155:66–71.

[24] Zhang J, Xie Z, Zhang J, Tang Y, Song C, Navessin T, et al. High temperature PEM fuel cells. J Power Sources 2006;160:872–91.

[25] Zhu Y, Zhu WH, Tatarchuk BJ. Performance comparison between high temperature and traditional proton exchange membrane fuel cell stacks using electrochemical impedance spectroscopy. J Power Sources 2014;256:250–7.

[26] Li S, Yuan J, Xie G, Sunden B. Numerical investigation of transport phenomena in high temperature proton exchange membrane fuel cells with different flow field designs. Numer Heat Transf Part A Appl 2017;72:807–20.

[27] Wang XD, Yan W-M, Duan YY, Weng F-B, Jung G-B, Lee C-Y. Numerical study on channel size effect for proton exchange membrane fuel cell with serpentine flow field. Energy Convers Manag 2010;51:959–68.

[28] Yoon YG, Lee WY, Park GG, Yang TH, Kim CS. Effects of channel and rib widths of flow field plates on the performance of a PEMFC. Int J Hydrogen Energy 2005;30:1363–6.

[29] Liu F, Kvesić M, Wippermann K, Reimer U, Lehnert W. Effect of Spiral Flow Field Design on Performance and Durability of HT-PEFCs. J Electrochem Soc 2013;160:F892–7.

[30] Liu H, Li P, Juarez-Robles D, Wang K, Hernandez-Guerrero A. Experimental Study and Comparison of Various Designs of Gas Flow Fields to PEM Fuel Cells and Cell Stack Performance. Front Energy Res 2014; 2(2)1-8.

[31] Department of Energy, Office of Science, Basic Research Needs for the Hydrogen Economy, http://www.sc.doe.gov/bes/hydrogen.pdf

[32] J Wang. System integration, durability and reliability of fuel cells: Challenges and solutions. Applied Energy 2017; 189:460–479.

[33] J Wu, X Yuan, J Martin, H Wang. A review of PEM fuel cell durability: Degradation mechanisms and mitigation strategies. Journal of Power Sources 2008; 184:104 – 119.

[34] U.S. Drive Fuel Cell Tech Team. Cell component accelerated stress test and polarization curve protocols for PEM fuel cells. 2013.

[35] N Zamel. Approaches and Methodology on Accelerated Stress Tests in Fuel Cells. 2013.

[36] S S Araya, F Zhou, V Liso, S L Sahlin, J R Vang, S Thomas, X Gao, CJeppesen, S K Kær. A comprehensive review of PBI-based high temperature PEM fuel cells. International Journal of Hydrogen Energy 2016; 41(46):21310–21344.

[37] G. Liu. Studies of performance degradation of high temperature PEMFC based on H3PO4 doped PBI. Journal of Power Sources 2006;

[38] J H Liao, Q F Li, H C Rudbeck, J O Jensen, A Chromik, N J Bjerrum et al. Oxidative degradation of polybenzimidazole membranes as electrolytes for high temperature proton exchange membrane fuel cells. Fuel Cells 2011; 11(6):745-55.

[39] J Liao, J Yang, Q Li, L N Cleemann, J O Jensen, N J Bjerrum et al. Oxidative degradation of acid doped polybenzimidazole membranes and fuel cell durability in the presence of ferrous ions. J Power Sources 2013; 238:516-22.

[40] Z Qi, S Buelte. Effect of open circuit voltage on performance and degradation of high temperature PBI–H3PO4 fuel cells. Journal of Power Sources 2006; 161:1126–1132.

[41] A Orfanidi, M K Daletou, L Sygellou, S G Neophytides. The role of phosphoric acid in the anodic electrocatalytic layer in high temperature PEM fuel cells. J Applied Electrochemistry 2013; 43(11):1101-1116.

[42] J Lobato, P Canizares, M A Rodrigo, J J Linares. PBI-based polymer electrolyte membranes fuel cells: temperature effects on cell performance and catalyst stability. Electrochimicaacta 2007; 52(12):3910-3920.

[43] A D Modestov, M R Tarasevich, V YaFilimonov and N M Zagudaeva, "Degradation of high temperature MEA with PBI-H3PO4 membrane in a life test", ElectrochimicaActa, vol. 54, no. 27, pp. 7121-7127, 2009.

[44] P J Ferreira, Y Shao-Horn, D Morgan, R Makharia, S Kocha and H A Gasteiger, "Instability of Pt/C electrocatalysts in proton exchange membrane fuel cells a mechanistic investigation", J. Electrochemical Society, vol. 152, no. 11, pp. A2256-A2271, 2005.

[45] S. Maass, F. Finsterwalder, G. Frank, R. Hartmann, and C. Merten, "Carbon support oxidation in PEM fuel cell cathodes," J. Power Sources, vol. 176, no. 2, pp. 444–451, 2008.

[46] K. H. Lim, H. S. Oh, S. E. Jang, Y. J. Ko, H. J. Kim, and H. Kim, "Effect of operating conditions on carbon corrosion in polymer electrolyte membrane fuel cells," J. Power Sources, vol. 193, no. 2, pp. 575–579, 2009.

[47] H.-S. Oh, J.-H. Lee, and H. Kim, "Electrochemical carbon corrosion in high temperature proton exchange membrane fuel cells," Int. J. Hydrogen Energy, vol. 37, no. 14, pp. 10844–10849, 2012.

[48] L. N. Cleemann et al., "Catalyst degradation in high temperature proton exchange membrane fuel cells based on acid doped polybenzimidazole membranes," Fuel Cells, vol. 13, no. 5, pp. 822–831, 2013.

[49] F. Zhou, S. J. Andreasen, and S. K. Kær, "Experimental study of cell reversal of a high temperature polymer electrolyte membrane fuel cell caused by H2 starvation," Int. J. Hydrogen Energy, vol. 40, no. 20, pp. 6672–6680, 2015.

[50] T. J. Schmidt and J. Baurmeister, “Properties of high-temperature PEFC Celtec®-P 1000 MEAs in start/stop operation mode,” J. Power Sources, vol. 176, no. 2, pp. 428–434, 2008.

[51] C. Hartnig and T. J. Schmidt, “Simulated start-stop as a rapid aging tool for polymer electrolyte fuel cell electrodes,” J. Power Sources, vol. 196, no. 13, pp. 5564–5572, 2011.

[52] T. Engl, L. Gubler, and T. J. Schmidt, “Fuel Electrode Carbon Corrosion in High Temperature Polymer Electrolyte Fuel Cells-Crucial or Irrelevant?,” Energy Technol., vol. 4, no. 1, pp. 65–74, 2016.

[53] S. Yu, L. Xiao, and B. C. Benicewicz, “Durability studies of PBI-based high temperature PEMFCs,” Fuel Cells, vol. 8, no. 3–4, pp. 165–174, 2008.

[54] Y. Oono, T. Fukuda, A. Sounai, and M. Hori, “Influence of operating temperature on cell performance and endurance of high temperature proton exchange membrane fuel cells,” J. Power Sources, vol. 195, no. 4, pp. 1007–1014, 2010.

[55] S. Matar, A. Higier, and H. Liu, “The effects of excess phosphoric acid in a Polybenzimidazole-based high temperature proton exchange membrane fuel cell,” J. Power Sources, vol. 195, no. 1, pp. 181–184, 2010.

[56] C. Hartnig and T. J. Schmidt, “On a new degradation mode for high-temperature polymer electrolyte fuel cells: How bipolar plate degradation affects cell performance,” Electrochim. Acta, vol. 56, no. 11, pp. 4237–4242, 2011.

[57] N. Pilinski, M. Rastedt, and P. Wagner, “Investigation of phosphoric acid distribution in PBI based HT-PEM fuel cells,” ECS Trans., vol. 69, no. 17, pp. 323–335, 2015.

[58] S. Lang, T. J. Kazdal, F. Kühl, and M. J. Hampe, “Experimental investigation and numerical simulation of the electrolyte loss in a HT-PEM fuel cell,” Int. J. Hydrogen Energy, vol. 40, no. 2, pp. 1163–1172, 2015.

[59] Y. Oono, A. Sounai, and M. Hori, “Prolongation of lifetime of high temperature proton exchange membrane fuel cells,” J. Power Sources, vol. 241, pp. 87–93, 2013.

[60] W. Maier et al., “In-situ synchrotron X-ray radiography on high temperature polymer electrolyte fuel cells,” Electrochem. commun., vol. 12, no. 10, pp. 1436–1438, 2010.

[61] S. H. Eberhardt, T. Lochner, F. N. Büchi, and T. J. Schmidt, “Correlating Electrolyte Inventory and Lifetime of HT-PEFC by Accelerated Stress Testing,” J. Electrochem. Soc., vol. 162, no. 12, pp. F1367–F1372, 2015.

[62] C. Wannek, B. Kohnen, H. F. Oetjen, H. Lippert, and J. Mergel, “Durability of ABPBI-based MEAs for high temperature PEMFCs at different operating conditions,” Fuel Cells, vol. 8, no. 2, pp. 87–95, 2008.

[63] S. Galbiati, A. Baricci, A. Casalegno, and R. Marchesi, “Degradation in phosphoric acid doped polymer fuel cells: A 6000 h parametric investigation,” Int. J. Hydrogen Energy, vol. 38, no. 15, pp. 6469–6480, 2013.

[64] S. Thomas, C. Jeppesen, T. Steenberg, S. S. Araya, J. R. Vang, and S. K. Kær, “New load cycling strategy for enhanced durability of high temperature proton exchange membrane fuel cell,” Int. J. Hydrogen Energy, vol. 42, no. 44, pp. 27230–27240, 2017.

[65] R. Taccani, T. Chinese, and M. Boaro, “Effect of accelerated ageing tests on PBI HTPEM fuel cells performance degradation,” Int. J. Hydrogen Energy, vol. 42, no. 3, pp. 1875–1883, 2017.

[66] Y. Zhai, H. Zhang, D. Xing, and Z. G. Shao, “The stability of Pt/C catalyst in H3PO4/PBI PEMFC during high temperature life test,” J. Power Sources, vol. 164, pp. 126–133, 2007.

[67] Kannan A, Kaczerowski J, Kabza A, Scholta J. Operation Strategies Based on Carbon Corrosion and Lifetime Investigations for High Temperature Polymer Electrolyte Membrane Fuel Cell Stacks. Fuel Cells 2018:1–12.

[68] Søndergaard T, Cleemann LN, Becker H, Steenberg T, Hjuler HA, Seerup L, et al. Long-Term Durability of PBI-Based HT-PEM Fuel Cells: Effect of Operating Parameters. J Electrochem Soc 2018;165:F3053–62.

[69] Søndergaard T, Cleemann LN, Zhong L, Becker H, Steenberg T, Hjuler HA, et al. Catalyst Degradation Under Potential Cycling as an Accelerated Stress Test for PBI-Based High-Temperature PEM Fuel Cells-Effect of Humidification. Electrocatalysis 2017;9:302–13.

[70] Schonvogel D, Rastedt M, Wagner P, Wark M, Dyck A. Impact of Accelerated Stress Tests on High Temperature PEMFC Degradation. Fuel Cells 2016;16:480–9.

[71] Reimer U, Schumacher B, Lehnert W. Accelerated Degradation of High-Temperature Polymer Electrolyte Fuel Cells: Discussion and Empirical Modeling. J Electrochem Soc 2014;162:F153–64.

[72] Kerr R, García HR, Rastedt M, Wagner P, Alfaro SM, Romero MT, et al. Lifetime and degradation of high temperature PEM membrane electrode assemblies. Int J Hydrogen Energy 2015;40:16860–6.

[73] S. Zhang et al., "A review of platinum-based catalyst layer degradation in proton exchange membrane fuel cells," J. Power Sources, vol. 194, pp. 588–600, 2009.

[74] C. Siegel, I. Buder, and A. Heinzel, "Sectional electrochemical impedance analysis of a high temperature polymer electrolyte membrane fuel cell with three types of flow-fields," Electrochim. Acta, vol. 112, pp. 342–355, 2013.

[75] J. L. Jespersen, E. Schaltz, and S. K. Kær, "Electrochemical characterization of a polybenzimidazole-based high temperature proton exchange membrane unit cell," J. Power Sources, vol. 191, no. 2, pp. 289–296, 2009

[76] J. Hu, H. Zhang, Y. Zhai, G. Liu, and B. Yi, "500 h Continuous aging life test on PBI/H3PO4 high-temperature PEMFC," Int. J. Hydrogen Energy, vol. 31, no. 13, pp. 1855–1862, 2006.

[77] C. De Beer, P. S. Barendse, P. Pillay, B. Bullecks, and R. Rengaswamy, "Classification of high-temperature PEM fuel cell degradation mechanisms using equivalent circuits," IEEE Trans. Ind. Electron., vol. 62, no. 8, pp. 5265–5274, 2015.

[78] http://www.scribner.com/wp-content/uploads/2017/06/Scribner-on-Fuel-Cell-Test-Methods-FC-Magazine-2005.pdf accessed on 28 November 2018.

[79] http://www.scribner.com/wp-content/uploads/2017/06/Scribner-Associates-Electrochemical-Impedance-Spectroscopy-for-Fuel-Cell-Research.pdf accessed on 28 November 2018.

[80] S. J. Andreasen, J. R. Vang, and S. K. Kær, "High temperature PEM fuel cell performance characterisation with CO and CO_2 using electrochemical impedance spectroscopy," Int. J. Hydrogen Energy, vol. 36, no. 16, pp. 9815–9830, 2011.

[81] G.-B. Jung, C.-C. Tseng, C.-C. Yeh, and C.-Y. Lin, "Membrane electrode assemblies doped with H3PO4 for high temperature proton exchange membrane fuel cells," Int. J. Hydrogen Energy, vol. 37, no. 18, pp. 13645–13651, 2012.

[82] F. J. Pinar, M. Rastedt, and N. Pilinski, "Characterization of HT-PEM Membrane-Electrode-Assemblies". 2016.

[83] https://www.slideshare.net/icpaes/atomic-spectroscopy-basic-principles-and-instruments accessed on 27 November 2018.

[84]http://analyticalprofessional.blogspot.com/p/oil.html accessed on 27 November 2018.

[85]https://serc.carleton.edu/research_education/geochemsheets/techniques/XRD.html accessed on 27 November 2018.

3 Materials and methods

In this chapter the samples, equipment used, experimental procedures and measurement techniques applied in this thesis are described.

3.1 DUT description

The device under test (DUT) in this study is HT-PEM fuel cell composed of MEA and flow field plates. MEA is "heart" of fuel cell where electrochemical reactions take place and flow field plates supply and remove reactants and products, respectively.

3.1.1 HT-MEA

All experiments were conducted using commercial BASF Celtec®-P 2100 HT-MEA of 938 µm thickness and 96 cm^2 active area. The membrane was phosphoric acid doped polybenzimidazole (PBI) with woven carbon cloth gas diffusion layer. Based on technical specifications declared by the producer, the catalyst on the cathode side is made of a Pt-alloy with a loading of 0.75 mg Pt cm^{-2} whereas the anode Pt catalyst loading is 1.0 mg Pt cm^{-2}. Other specification details concerning the HT-MEA remaining confidential and are not disclosed by the manufacturer.

3.1.2 Flow field plates

The Flow field plates are made of graphite composite material (FU 4369 HT) supplied by Schunk and more details regarding the material properties of plates are provided in Appendix A-1. The required flow pattern is carefully inscribed on to graphite plate using KERN CNC High Precision Micro Milling and Drilling Machine type EVO. The flow pattern on the anode side was multiple serpentine design and remained unchanged for all experiments. Three different flow field designs for the cathode side were used in this study to achieve the purpose of this thesis. The three designs are shown in Figure 3-1 multiple serpentine, segmented serpentine, straight and parallel. More details concerning the specifications of individual design are given in Table 3-1. The graphite plate on cathode side is of 4.675 mm thickness and 102 mm X 102 mm geometrical area.

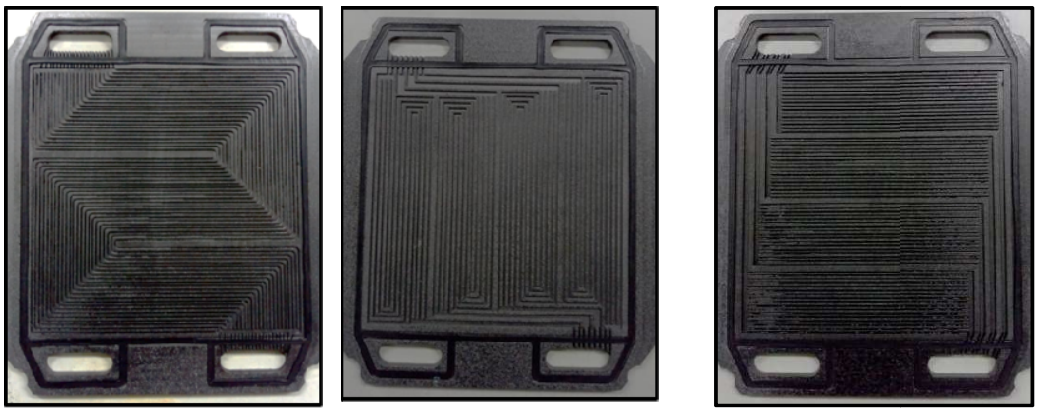

a) Multiple serpentine b) Segmented serpentine c) Straight and parallel

Figure 3-1 Graphite bipolar plate with flow field designs used for cathode in this study.

The apparent contact area of MEA with graphite flow plate is calculated for all the three designs and the values are almost the same. Multiple serpentine design consists of 23 channels with channel length of 302 mm each. Segmented serpentine design has 4 segments with 4 channels per each segment. The straight and parallel design has 4 segments with 17 channels for each segment. The three flow field designs are in 'Z' type configuration. All the designs have channel depth of 0.735 mm.

Table 3-1 Design specifications of flow field plates.

Flow field design	Contact area with MEA, %	No. of channels/ segments	Channel dimensions			Rib
			Length, mm	Width, mm	Depth, mm	Width, mm
Multiple serpentine	53	23	302	0.7	0.735	0.7
Segmented serpentine	52	4/4	253	1	0.735	1
Straight and parallel	53	17/4	82	0.7	0.735	0.7

3.2 Test set-ups

The HT-MEA is sandwiched between two graphite plates with multiple serpentine flow field on anode side (Figure 3-1a) and three different flow field designs on cathode side (Figure 3-1) are used. The HT-MEA is compressed with 3 N m torque.

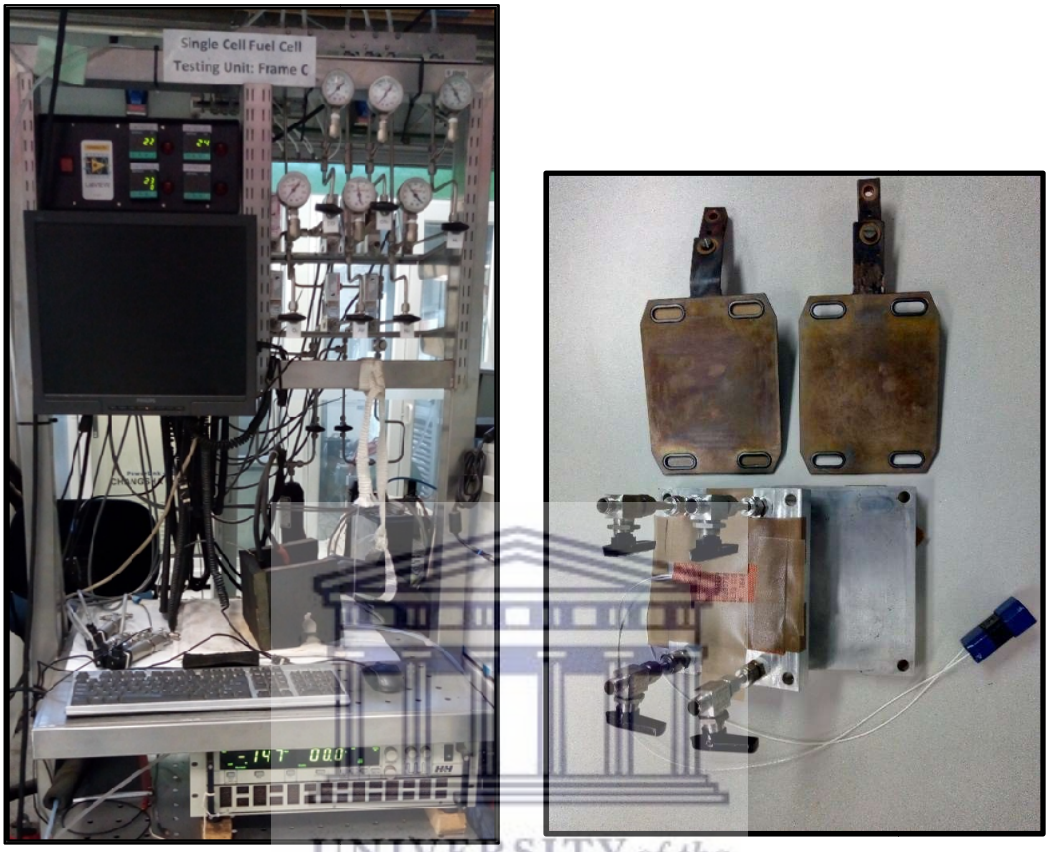

a) b)

Figure 3-2 a) manual test station and b) components of fuel cell assembly.

The fuel cell is tested using manual test station as shown in Figure 3-2a with LabView control based application. The fuel cell assembly is achieved using in-house designed gasket, current collector, insulating sheet and end plates as shown in Figure 3-2b. The end plates are made of aluminium and current collector plates are made of copper metal coated with gold. The temperature is controlled using a PID controller connected to silicone heating pads (200 W) mounted on the surface of aluminium endplates. The water collection points from anode and cathode are extended using a Teflon tube and connected to water bottle of limited capacity. Active cooling methods are not employed for water condensation. Prolonged operation at high temperature caused issues related to fuel cell set-up (such as copper plates, copper bars are used to connect the fuel cell to thick current carrying cables from DC load box) leading to measurement errors and inaccurate results. This particular test set-up is used for evaluation of three flow fields

(section 4.2) and before each test the gold coated copper current collector plates and copper bars are scrubbed to remove surface impurities and other corrosion products but has not resulted in significant improvement in measurements. So, all the experiments (section 4.1, 4.3, 4.4 and 4.5) are conducted using FuelCon Evaluator as controlling the operation parameters is accurate. The HT-PEMFC is tested using FuelCon Evaluator C1000-LT fuel cell test station that was adapted for HT-PEMFC operation as shown in Figure 3-3 along with flow field plates.

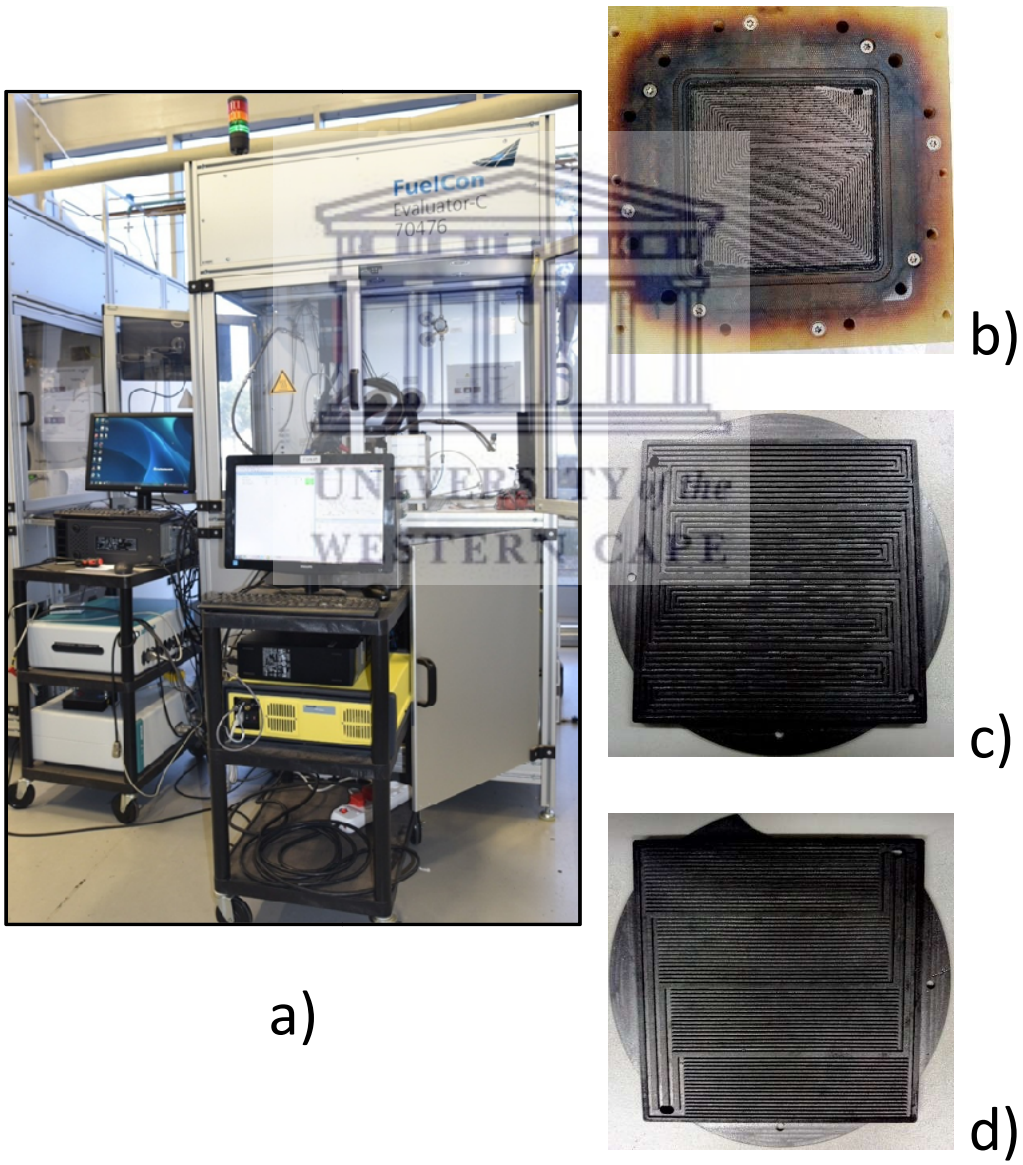

Figure 3-3 a) FuelCon fuel cell test stand and cathode flow field plates b) multiple serpentine c) segmented serpentine d) straight and parallel design.

The MEA is compressed between graphite plates using Cell fixture from balticFuelCells GmbH model cF 100/400 HT and quick connect fixture qCf FC100/400 shown in Figure 3-4a is used to apply uniform and repeatable compression pressure of 2 Nmm^{-2}. The cell fixture is slightly modified to accommodate the flow field plates and the drawings of three flow fields used on FuelCon Evaluator are shown in Appendix A-2, A-3 and A-4. The gases are supplied to fuel cell in counter flow configuration. The software user interface in Figure 3-4b from fuel cell test station is used to control the operating conditions and data logging process.

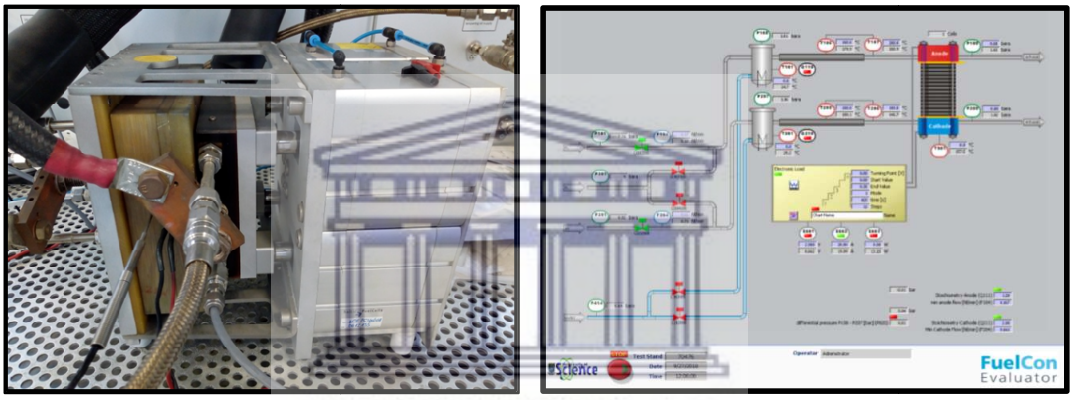

a) b)

Figure 3-4 a) Cell fixture quick connect fixture integrated in FuelCon test stand b) FuelConTestWork software package user interface to control fuel cell operating parameters and data collection.

3.3 Experimental procedures

The HT-PEMFC is operated in three different stages as shown in Figure 3-5. During the start-up the fuel cell is preheated to 120°C and nitrogen gas is purged through the cell during the pre-heating. Thereafter hydrogen and air are supplied to the cell and cell's load current is increased step-wise to 20 A.

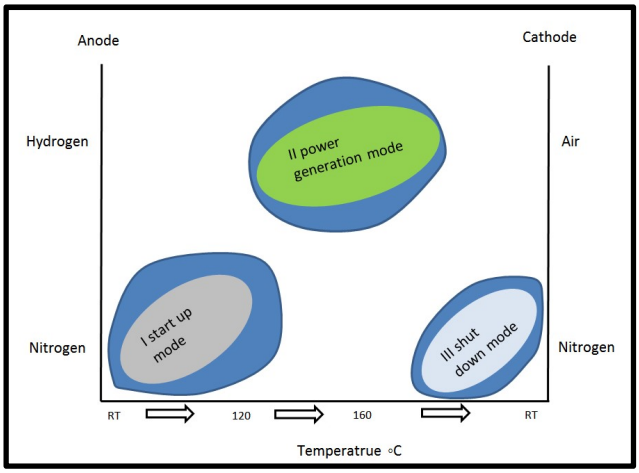

Figure 3-5 Operation stages of HT-PEMFC.

The pre-heating continues until the cell reaches 160°C and switch to the power generation stage. Shut down of fuel cell is performed by reducing the current to 5 A followed by complete load termination (0 A). The cell and the gas pipes are purged with nitrogen during shut down and cell is cooled down to room temperature.

In this thesis 5 experiments are conducted with HT-MEA and details of tests and results are presented accordingly. After the break-in procedure 1) HT-MEA is evaluated with multiple serpentine flow field on anode and cathode side, 2) EIS of three different flow fields on cathode side using manual test set-up, 3) Long term stability tests, 4) potential cycling test and 5) potential holding test are performed. Break-in of fuel cell is performed before each experiment by applying a constant current density of 0.2 A cm^{-2} for 100 hours after the start-up of fuel cell. It should be noticed that two different cell fixtures (FuelCon test station and bolt & rod) are used in this thesis however FuelCon fuel cell test station (Figure 3-3a) is used for long term durability test (4.3), potential cycling test (4.4), potential hold test (4.5) and also evaluation of multiple serpentine design (4.1). Bolt and rod test set up (Figure 3-2a) is used only for EIS characterization of fuel cell with three different designs (4.2). The main purpose of using automated test stand is to eliminate the discrepancies (non-uniform torque) caused by irregular assembling procedures by human intervention. Calculations involving applied torque/pressure distribution are not performed for any of the plate designs.

Table 3-2 Required hydrogen and air flow rates calculated for current of 20 A.

Equation	H_2 (Anode)	Air (Cathode)
$\chi = \frac{IN}{nF}$	0.166 SLPM	0.667 SLPM
$I = 20\ A$ $N = 1$ $n = 2$ for HOR; 4 for ORR	1.2 stoichiometry	2 stoichiometry (0.21 % of O_2 in air)

Where χ is reactant flow rate in standard litre per minute (SLPM)and n is the number of electrons involved in HOR and ORR.

Non-humidified reactants are supplied to the fuel cell during break-in operation at ambient pressure. The minimum gas flow rates of 0.167 SLPM for hydrogen and 0.663 SLPM for air are set for the anode and cathode, respectively. The flow rates are calculated based on the fuel cell stoichiometry of 1.2 and 2, for anode and cathode, respectively, and the values are presented in Table 3-2.

3.3.1 Long term stability tests

Performance evaluation and comparison is conducted by in-situ studies (see section 3.4) after break-in. The performance evaluation is to study the effect of flow field design at BoL parameters immediately after break-in whereas long term stability test with constant current are performed to study the influence of flow field design on the stability of HT-MEA. The long term stability test is performed at 0.2 A cm^{-2} for 500 hours after break-in. During testing in-situ studies are conducted at BoL after 100 h, 250 h, 350 h and 500 h of operation and ex-situ studies after end of time (EoT) is reached.

PEMFCs for automotive applications undergo thousands of cycles (combination of load or voltage cycles and start-stop cycles) during normal operation of the vehicle. Under these conditions, fuel cells suffer from severe degradation of cathode, anode and membrane. Compared to real time experiments, ASTs occur at more stressful condition to accelerate the failure mode.

3.3.2 Potential cycling test

For a typical automotive application, fuel cells must undergo severe load cycling depending on the load demand. Potential cycling AST is used to simulate such conditions in a short time. PEMFCs operate under load cycles, high power demand conditions, idling conditions and start-up and shut-down conditions. So, it is necessary to use a protocol with conditions to simulate the real automotive driving conditions, to predict the PEMFCs lifetime and analyze the potential degradation mechanisms. AST are performed with potential cycling with the details of experimental procedure represented in Figure 3-6. Potential cycling is applied in a square wave pattern with each potential cycle consisting of 3 minutes holding at 0.5 V and subsequent 3 minutes holding at 0.9 V. A maximum of 5000 of such cycles are desired on fuel cell under test. The temperature of the cell is maintained at 160°C during the AST and stoichiometry of 1.2 and 2 is maintained for hydrogen and air, respectively under all circumstances. Minimum flow of 0.167 SLPM for hydrogen and 0.663 SLPM for air are set under ≤20 A load conditions to eliminate degradation effects from unexpected fuel starvation conditions. Three HT-PEMFC single cells with the same anode flow field plate (multiple serpentine design) and different cathode flow field designs are assembled and tested with AST to provoke degradation and study and durability in shorter time. AST is interrupted at regular intervals after every 10 cycles, 100 cycles, 1000 cycles, 2500 cycles and EoT for in-situ characterization studies and ex-situ studies are performed only after EoT.

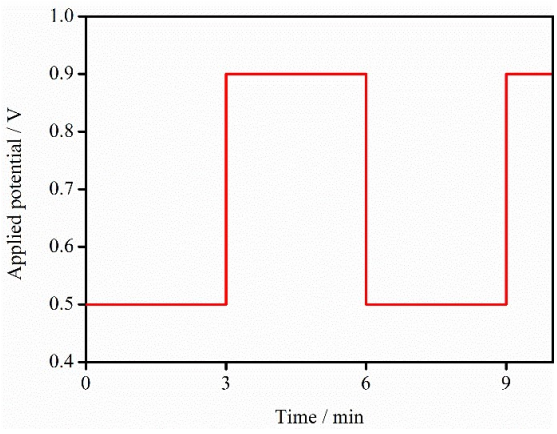

Figure 3-6 AST procedures for potential cycling test.

3.3.3 Potential hold test

Potential holding AST is used to study the degradation of catalyst carbon support. A constant potential was applied to the fuel cell with the use of external potentiostat to trigger the degradation of carbon support. Potentials of 0.9 V, 1.0 V, 1.1 V and 1.2 V are applied for period of 30 minutes each, followed by in-situ characterization respectively and ex-situ studies in the end. Potential holding at 0.9, 1.0, 1.1, and 1.2 V in AST is used to simulate the start and stop condition in the fuel cell vehicle. Synthetic air with a flow rate of 0.663 SLPM and hydrogen with a flow rate of 0.167 SLPM is supplied during the potential hold test to cathode and anode respectively. Application of synthetic air allows to measure precisely the carbon support corrosion. It is determined by measuring the carbon dioxide gas concentration at cathode exhaust using Gasmet DX4000 non dispersive FT-IR online gas analyser. For elaborate start-up, potential cycling and potential holding test procedure refer to flow charts A-5, A-6 and A-7 in Appendix.

The AST (potential cycling and potential hold) is designed to target electrocatalyst degradation with the influence of different flow field designs, which is slightly modified version of the U.S. Department of Energy (DoE) recommended AST protocol for electrocatalyst degradation [1]. DoE's potential cycling protocol is between 0.7 V and 0.9 V for 30s each step, however potential cycling in this work is conducted between 0.5 V and 0.9 V for 3 min each step, for 5000 cycles to accelerate the degradation process. Similarly, catalyst support focused potential hold protocol is modified to 0.9, 1.0, 1.1 and 1.2 V for 30 minutes instead of 1.2 V for 24 h. In both the cases the end of test criteria is < 40% loss of initial ECSA.

3.4 Characterization methods

The characterization methods utilised for each test are mentioned in Table 3-3 and details of each method are explained below. They are divided into in-situ and ex-situ techniques.

Table 3-3 Summary of characterization techniques used for tests performed in this thesis.

Test type	Measurement techniques						
	In-situ					Ex-situ	
	I-V curve	EIS	CV	LSV	FT-IR	TEM, XRD, SEM, EDS	ICP-OES
Performance evaluation	✓	✓	✓	✓	×	×	×
Potential cycling	✓	✓	✓	✓	×	✓	✓
Potential hold	✓	✓	✓	×	✓	✓	×
Long term stability test	✓	✓	✓	✓	×	✓	×

3.4.1 In-situ techniques

Polarisation curves, EIS spectra, CV, LSV and FT-IR methods fall under in-situ characterization techniques.

3.4.1.1 Polarisation curves

I-V curves are recorded with the aid of built-in in FuelCon testing set-up electronic load - TrueData-LOAD. The measurements are performed in a galvanostatic mode from OCV with 10 A current step increment and stabilization time of 30 seconds at each step. The cut-off current is set to be 100 A and cut-off voltage is 0.4 V for all measurements.

Tafel slope analysis (related to kinetic overvoltage) is performed from I-V curve below the current density of 0.1 A cm^{-2} (Tafel approximation i>> exchange current density i_0). At lower current densities, the reactants are abundant and ohmic losses are negligible. Tafel slope is a function of cathode kinetics. From the I-V curve data the kinetic parameters of the ORR for HT-PEMFC can be obtained from Tafel equation 3-1 and 3-2 [2]. The Tafel slopes are calculated from the iR corrected I-V curves in the current density range between 0.01-0.1 A cm^{-2} such that mass transport overpotential values are very small.

$$E_{ir-f} = E_{cell} + iR \qquad \text{(eq. 3-1)}$$

$$= a - b \log i \qquad \text{(eq. 3-2)}$$

$E_{ir-free}$ is ohmically corrected cell voltage; E_{cell} is cell voltage; i is current density; R is ohmic resistance of fuel cell (determined from EIS), a is constant that depends on temperature and electrodes and b is Tafel slope for ORR. The contribution of HOR to cell polarisation is negligible in H_2/air PEMFCs and at low current densities (0.01-0.1 A cm^{-2}) the mass transport losses can be neglected. The polarisation data in the low current density range (<0.1 A cm^{-2}) are fit to equation 3-1 and 3-2 and Tafel plots are plotted using $E_{ir-free}$ vs. $\log i$ graph. These plots represent the overall kinetics of the ORR of cathode. The exchange current density of hydrogen oxidation on anode side is thousand times greater than the ORR on the cathode side and the kinetic overpotential of the anode side is negligible. The Tafel slopes of HT-PEMFC are found to be approximately 90 mV/decade [3, 4] and 111-126 mV/decade [2].

3.4.1.2 EIS

For electrochemical characterization measurements (such as EIS, CV and LSV), Autolab PGSTAT 302N with external Galvanostat/Potentiostat is used. The cathode is used as sense and working electrode whereas anode is used as counter and reference electrode. EIS is recorded at steady state fuel cell load of 0.2 A cm^{-2} current density. The perturbation voltage amplitude of 10 mV and frequency range from 10 kHz to 0.1 Hz is used for impedance characterization (in some cases the scanning frequency is altered to 1 kHz-0.1 Hz). A total of 50 frequency points are recorded during the frequency scan in logarithmic distribution (in some cases the frequency points are reduced to 25 to eliminate noise and obtain better spectra). Both, I-V curves and EIS spectra, are recorded three times with 10-15 minutes interval with conditioning at 0.2 A cm^{-2} between each measurement. The outputs of EIS measurements are presented in the form of Nyquist and Bode plots.

The Nyquist plots are analysed using EEC model to understand the electrochemical processes occurring within the fuel cell. The fitting of EEC is performed by using software like NOVA with suitable circuit model based on the physical interpretation. The software gives an error percentage for each of the circuit elements in the EEC model. As the fitting progresses the NLLS Analysis software calculates X^2 value for the fit. The quality of

fit needs visual examination as X^2 value needs to be monitored along with data and fitted model.

3.4.1.3 CV

CV is performed with hydrogen stripping method at room temperature (25°C) to determine ECSA of fuel cell from equation 3-3. The hydrogen adsorption charge on a smooth Pt electrode is 210 µC cm^{-2}-Pt [5]. The voltage of fuel cell cathode is scanned from 0.05-0.8 V and back in a cyclic manner with scan rate of 30 mV s^{-1}. The anode and cathode are supplied with 1 or 2 SLPM of hydrogen and 1 SLPM of nitrogen respectively during the CV measurements.

$$\mathrm{ECSA} = \frac{\text{integrated area (AV) (obtained from CV curve)}}{\text{scan rate}\left(\frac{\mathrm{mV}}{\mathrm{s}}\right) * \text{Pt loading}\left(\frac{\mathrm{mg}}{\mathrm{cm^2}}\right) * 210\left(\frac{\mu\mathrm{C}}{\mathrm{cm^2-Pt}}\right)} \quad \text{(eq. 3-3)}$$

3.4.1.4 LSV

LSV is performed to assess the hydrogen cross over and internal short circuit resistance. The voltage of cathode is scanned from 0.05-0.5 V with 2 mV s^{-1} scan rate at room temperature (25°C). The anode and cathode are supplied with 1 SLPM of hydrogen and 1 SLPM of nitrogen respectively during measurements. The hydrogen crossover flux ($H_{2,\mathrm{crossover}}$) through the membrane can be calculated from the limiting current density ($j_{H_{2,\mathrm{cross}}}$) using Faraday's law [6] in equation 3-4.

$$H_{2,\mathrm{crossover}} = \frac{j_{H_{2,\mathrm{cross}}} * A}{n * F} \quad \text{(eq. 3-4)}$$

Where A is area of fuel cell, n is number of electrons involved (2 for HOR) and F is Faraday's constant. If a fuel cell develops internal short-circuit, the LSV curve must be corrected for internal short- circuit before making hydrogen crossover analysis. The internal short-circuit resistance can be estimated from the inverse of the slope from the curve within the range where linear relation between current density and potential is observed around 0.3-0.4 V.

3.4.1.5 On-line FT-IR cathode off-gas analysis

The Gasmet DX4000 FT-IR online gas analyzer with a range up to 10000 ppm of CO_2 is used to analyse the carbon dioxide concentration in the cathode exhaust and applied measurement procedure is prepared according to described by Meier et al. [7]. The HT-PEMFC cathode exhaust gas is allowed to pass through FT-IR for continuous gas analysis. A portable sampling system (PSS) is used in combination with the Gasmet DX4000 FT-IR gas analyser. The PSS unit is heated to 180°C and maintained at that temperature during analysis to avoid water condensation. The PSS, sample gas and sample cell is maintained at same temperature. Before the FT-IR measurements a background calibration is performed by passing the zero gas through the sampling system. After the background measurement, a scan rate of 5 sec is used for probing carbon dioxide peaks from cathode exhaust. The concentration of unknown carbon dioxide is determined from the area under the IR absorption peaks with characteristic wavelength range of CO_2 (2282-2348 cm^{-1}). The Gasmet software application process the experimental parameters and log data output. Typically a plot of ppm vs. time can be plotted for analysis. The total amount of carbon dioxide from exhaust gas can be calculated by integrate the area of CO_2 curve with respect to time 30 min. (ppm vs. time). The mass of corroded carbon (m_{cc}) can be calculated using equation 3-5 in ref. [8]. One major drawback is H_2O, serious concern obstructing the ability to calculate carbon dioxide. The pressure, flow and temperature of the sample gas are maintained stable during background measurement and analysis.

$$m_{cc} = M_C * n_{CO_2} = M_C \frac{PV}{RT} * A_{CO_2-pe} \quad \text{(eq. 3-5)}$$

A_{CO_2-peak} is the integrated area of the CO_2 peak (ppms); P and T are the ambient pressure and temperature respectively; R is the universal gas constant; M_C is the molar mass of carbon and V is the effective volumetric gas flow rate.

3.4.2 Ex-situ techniques

The ex-situ methods involve ICP-OES, SEM, TEM and XRD analysis.

3.4.2.1 ICP-OES

The water collected on fuel cell cathode exhaust is analysed for P and Pt elements (for phosphoric acid and platinum loss respectively) with ICP-OES. Varian 710-ES now Agilent is used to determine elemental composition in range 177-785 nm wavelength with detection limit of ≤1 ppm. It uses CCD spectrometer with excellent signal-to-noise performance with very low detection limits. The concentration of unknown is determined by comparing the intensity of light emitted by solutions of known metal concentrations. A minimum of three standard solutions are used for calibration for P estimation. The standards used should have a concentration close to expected concentration of the sample. Blank and standard are used to calibrate instrument which are prepared from 2% nitric solution and LGC custom standard 1586 respectively (commercial). A calibration curve is obtained with above standards P 213 of 1st order line (strong intensity) and P 178 of 3rd order line (weak intensity) accordingly. 45 ml of sample is isolated from the main sample and analysed for P analysis using ICP-OES. 4-5 ml of sample is used by equipment for a good run. The ICP Expert I software allows easy data collection. Phosphoric acid loss rates and molarity of Pt from condensed water of cathode exhaust are calculated from ICP-OES data. Phosphoric acid loss rate (ng cm^{-2} h^{-1}) is calculated according to [9] from equation 3-6:

$$H_3PO_4 \text{ loss rate} = \frac{\left(\frac{M_{H_3PO_4}}{M_{HPO_4^{2-}}}\right) \cdot V_{sample} \cdot C_{HPO_4^{2-}}}{A \, .t} \quad \text{(eq. 3-6)}$$

V_{sample} is volume of liquid in container; M is molar mass ($M_{H_3PO_4}$= 98 g mol^{-1} and $M_{HPO_4^{2-}}$ = 96 g mol^{-1}); A is active area; t is time in hours; $C_{HPO_4^{2-}}$ is concentration of P (obtained from ICP-OES) in ng L^{-1}.

The molarity of Pt is calculated using equation 3-7 concentration (ppm) values obtained from ICP-OES. Molarity is number of moles of solute per litre of solution.

$$\text{Molarity} = \frac{\text{ppm} * 0.001}{\text{atomic weight}} \quad \text{(eq. 3-7)}$$

3.4.2.2 SEM

A small portion of MEA is cut for SEM analysis. AURIGA field emission high resolution SEM supplied by Zeiss (Germany) is used for cross sectional image of MEA. The gun vacuum is 7.7 X 10^{-10} mbar and system vacuum is 7.3 X 10^{-7} mbar with filament current of 2.359 A. The sample preparation for SEM is very important. The cut portion of MEA is carefully mounted on aluminum stubs with the help of carbon tabs in order for the MEA to stick to the stub. The MEA samples are then coated with carbon using the EMITECH K950X carbon evaporator. The carbon coated sample is placed in vacuum chamber of SEM and 5 KeV is used for SEM imaging and processed with SmartSEM imaging software. The working distance for image is displayed on the image. EDS is performed with 20 KeV and data processed with AZTEC software.

3.4.2.3 TEM

The MEA is carefully scraped over anode and cathode sides after peeling the gas diffusion layer for carbon supported catalyst layer. The scraped catalyst powder is stored in container analysed for catalyst particle size estimation and distribution using TEM. The catalyst samples are first dissolved in ethanol followed by ultra-sonication 20-30 min under medium to high frequency to disperse the nanoparticles. The sample is then isolated with a micro pipette and deposited on a copper grid for TEM image analysis. Samples for TEM are prepared by drop-coating. A drop of sample solution onto a carbon coated copper grid. This is then dried under a Xenon lamp for about 10 minutes and analysed under the microscope. Transmission electron micrographs are collected using an FEI Tecnai G2 20 field-emission gun (FEG) TEM, operated in bright field mode at an accelerating voltage of 200 kV. Energy dispersive X-ray spectra are also collected using an EDAX liquid nitrogen cooled Lithium doped Silicon detector for chemical composition of catalyst on anode and cathode side. The TEM images are obtained at 2, 5, 10, 20 and 50 nm resolution. Platinum particle size is evaluated using Image J software application. The mean particle diameter d_m is calculated from histograms with the equation 3-8 [10]:

$$d_m = \frac{\sum_i (x_i d_i)}{\sum_i x_i} \text{ (eq. 3-8)}$$

x_i is the number of particles with diameter d_i. To determine the mean diameter of Pt particles at least 300 particles are chosen. The corresponding standard deviation σ is calculated using the following equation 3-9 [10]:

$$\sigma = \sqrt{\frac{\sum_i (x_i (d_m - d_i)^2)}{\sum_i x_i - 1}} \text{ (eq. 3-9)}$$

3.4.2.4 XRD

XRD is performed on the scraped catalyst on anode and cathode side of MEA to identify the crystallite size of catalyst with the help of Bruker AXS (Germany) with D8 Advance X-ray diffractometer using Cu-Kα radiation ($\lambda K\alpha_1$ = 1.5406 Å) with a tube current of 40 mA, and tube voltage of 40 kV. The 2-theta angular regions between 10° and 89.992° are explored at a scan rate of 0.5 sec per step and 0.034° increment in continuous scan in locked coupled mode with step time 96 sec. An example of the phase and crystal structure of the Pt nanoparticles (crystalline Pt) is shown in Figure 3-7. The broad diffraction peaks of the XRD pattern at 2θ =39.6, 47.4, 67.1, 81.2 and 83.6° corresponding to the reflections (111), (200), (220), (311) and (222) respectively for a face centered cubic (fcc) structure of platinum (JCPDS Card 04-0802). The Pt particle size (D_{hkl}) is estimated from the width of principal diffraction peak (1 1 1)/(220) using the Scherrer formula in equation 3-10 [10]:

$$D_{hkl} = \frac{k\lambda}{\beta \cos\theta} \text{ (eq. 3-10)}$$

θ is the incidence angle for hkl reflection (rad); β is the angular line width at medium height FWHM (rad); k is Scherrer constant (0.9) the shape factor; λ is the X-ray wavelength;

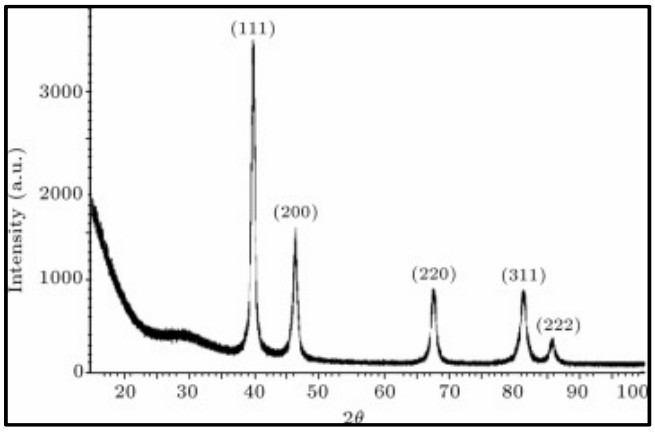

Figure 3-7 XRD spectra of Pt nanoparticle [11].

References

[1] Garland N, Benjamin T, Kopasz J. DOE Fuel Cell Program: Durability Technical Targets and Testing Protocols. ECS Trans 2007;11:923–31

[2] Su H, Felix C, Barron O, Bujlo P, Bladergroen BJ, Pollet BG, et al. High-Performance and Durable Membrane Electrode Assemblies for High-Temperature Polymer Electrolyte Membrane Fuel Cells. Electrocatalysis 2014;5:361–71.

[3] Mader J, Xiao L, Schmidt TJ, Benicewicz BC. Polybenzimidazole / Acid Complexes as High-Temperature Membranes. vol. 216. 2008.

[4] Park JO, Kwon K, Cho MD, Hong S, Kim TY, Yoo DY. Role of Binders in High Temperature PEMFC Electrode Role of Binders in High Temperature PEMFC Electrode. J Electrochem Soc 2011;158:B675–81.

[5] Wu J, Yuan XZ, Martin JJ, Wang H, Zhang J, Shen J, et al., "A review of PEM fuel cell durability: degradation mechanisms and mitigation strategies", J. Power Sources, vol. 184, pp. 104-19, 2008.

[6] K. R. Cooper, "In Situ PEMFC Fuel Crossover & Electrical Short Circuit Measurement," Fuel Cell Magazine, vol. Aug/Sep, pp. 1–2, 2008.

[7] F Meier, S Denz, A Weller and G Eigenberger, "Analysis of Direct Methanol Fuel Cell (DMFC)-Performance via FTIR Spectroscopy of Cathode Exhaust", Fuel Cells, vol. 3, no. 4, pp. 161-168, 2003.

[8] T. Engl, J. Käse, L. Gubler, and T. J. Schmidt, "On the Positive Effect of CO during Start/Stop in High-Temperature Polymer Electrolyte Fuel Cells," ECS Electrochem. Lett., vol. 3, no. 7, pp. F47–F49, 2014.

[9] S. H. Eberhardt, T. Lochner, F. N. Büchi, and T. J. Schmidt, "Correlating Electrolyte Inventory and Lifetime of HT-PEFC by Accelerated Stress Testing," J. Electrochem. Soc., vol. 162, no. 12, pp. F1367–F1372, 2015.

[10] I. Dobrosz, K. Jiratova, V. Pitchon, and J. M. Rynkowski, “Effect of the preparation of supported gold particles on the catalytic activity in CO oxidation reaction,” J. Mol. Catal. A Chem., vol. 234, pp. 187–197, 2005.

[11] M. A. Shah, “Growth of uniform nanoparticles of platinum by an economical approach at relatively low temperature,” Sci. Iran., vol. 19, no. 3, pp. 964–966, 2012.

4 Results and discussion

In this section the results obtained from following tests:

- Characterization of the cell with multiple serpentine flow field,
- EIS of three flow field designs,
- Long term stability tests
- Potential cycling,
- Potential holding,

performed as a part of this thesis with various characterization methods involved are presented, described, analysed and discussed.

4.1 Evaluation of multiple serpentine design

The multiple serpentine gas flow pattern is widely used for fuel cell application as it ensures better performance and durability. The test set-up shown in Figure 3-3 is used to perform experiments. The current voltage and power relationships along with impedance behaviour and ECSA at different scan rates are obtained. The purpose of the test is to obtain results and use them as a reference to compare with the other two flow fields. The effect of anode and cathode stoichiometry along with the influence of operating temperature on the performance of fuel cell is investigated.

4.1.1 In-situ characterization

The HT-MEA is characterized with multiple serpentine flow field design in order to evaluate its performance. The MEA is activated at conditions mentioned in section 3.3. A break-in time of 140 h is seen from the Figure 4-1. The activation time is desired for only 100 h but due to lab operation conditions the break-in time is extended. As it can be seen from figure the MEA has stable voltage during the break-in period. A maximum voltage of 0.664 has been recorded at 0.2 A cm^{-2} during this period.

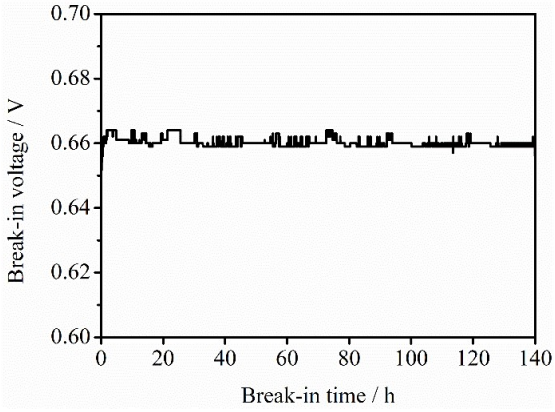

Figure 4-1 Fuel cell voltage during break-in period with cell temperature 160°C, λ = 1.2/2 of H2/Air are being supplied on anode and cathode respectively at set cell temperature of 160°C.

The temperature profile during the break-in period is shown in Figure 4-2. The pre-heating of fuel cell to set temperature of 160°C takes about 1 h depending on RT (according to seasonal weather conditions). On the contrary cooling period takes almost 3 h from 160 to 26°C.

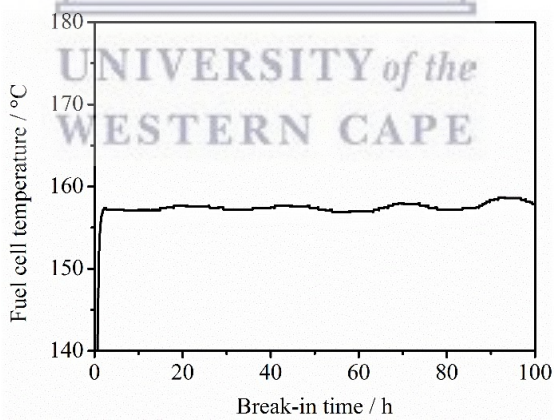

Figure 4-2 Fuel cell temperature during break-in period.

4.1.1.1 Polarisation curves

After the activation period polarisation curves are recorded. The voltage and power density relationship with increasing current density is shown in Figure 4-3. An OCV of 0.926 V is measured on the cell and as the current is drawn activation losses start to appear with steep drop in cell voltage at current densities < 0.1 A cm^{-2}. There after the linear part of polarisation curve is attributed to domination of ohmic losses. Mass

transfer limitations tend to appear at higher current densities > 0.8 A cm^{-2} due to limitation of gas transfer or gas diffusion in porous catalyst layers. The maximum power density of 385 mW cm^{-2} is obtained at 1.1 A cm^{-2}. Operating cell at maximum power densities causes degradation to fuel cell. It should also be noticed that the performance of a HT-PEMFC is lower than the LT-PEMFC at particular current density. Also the efficiency of an HT-PEMFC is lower than that of an LT-PEMFC at a given operating point because of the large activation losses due to the adsorption of phosphate (PO_4^{3-}) anions at the catalyst [1]. However the performance can be improved by increasing the pressure and temperature [2].

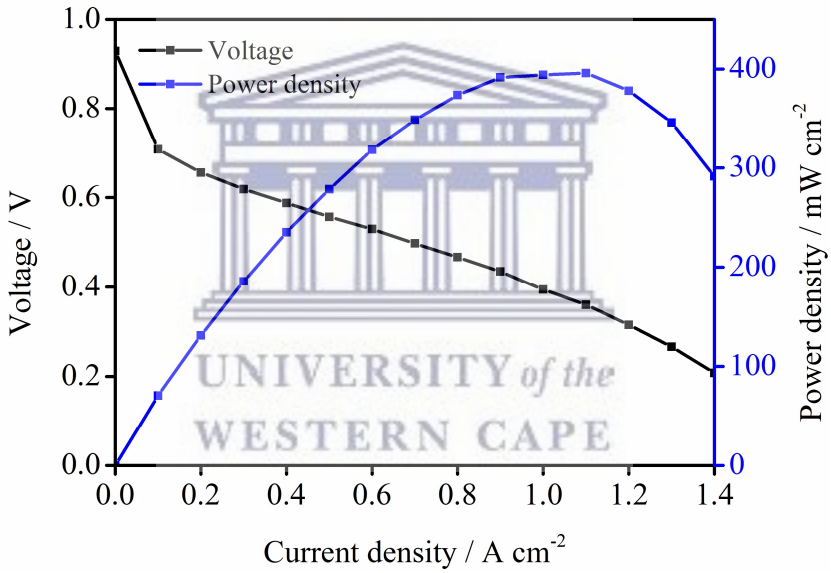

Figure 4-3 Polarisation curve of HT-PEMFC at the BoL after the 140 h break-in period, cell temperature 160°C, λ = 1.2/2 for H_2 and air respectively, gases supplied to anode and cathode at 160°C and ambient pressure.

4.1.1.2 EIS

After the polarisation curve measurement, EIS spectra is recorded after additional pre-conditioning of the fuel cell for 24 h. The Nyquist and Bode plots from the resulting impedance measurements are shown in Figure 4-4a and 4-4b respectively. The inductance behaviour is omitted from Figure 4-4. The Bode plot representing the impedance behaviour with changing frequency is seen in Figure 4-4b. The total cell resistance is 5.2 mΩ.

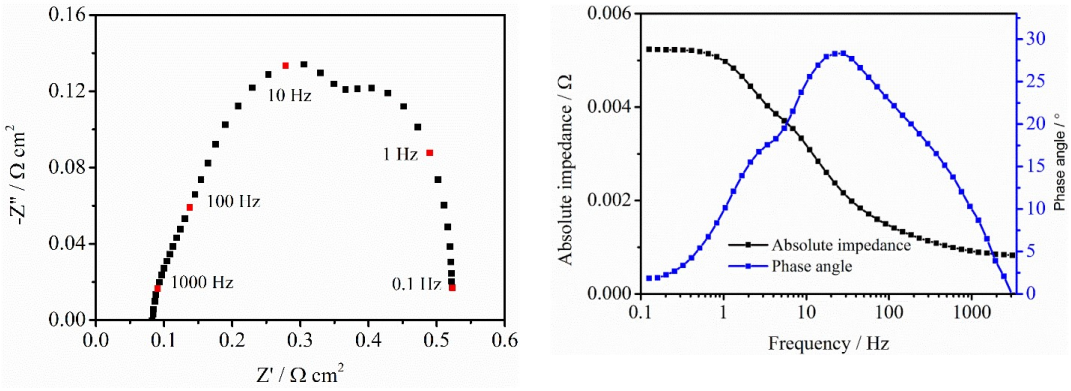

a) b)

Figure 4-4 a) Nyquist plot and b) Bode plot of HT-PEMFC with multiple serpentine design at 160°C and 0.2 A cm^{-2} λ = 1.2/2 of H_2/Air are being supplied on anode and cathode respectively.

The Nyquist plot is fitted with equivalent circuit composed of inductor, a series resistor connected to three parallel RC circuits. The capacitor is replaced with constant phase element (CPE) for better fit. The origin of CPE is ambiguous. It is used for describing a distributed charge accumulation on rough irregular electrode surfaces. It can arise from surface or axial distributions. CPE parameters can be interpreted in terms of capacitance, depending on type of distribution. The usage of CPE may lead to improved regressions (in case of depressed semi-circle). But, not all depressed semi-circles correspond to CPE behaviour. The EEC fitting is performed using Nova 2.1 software and final circuit elements with obtained parameters is shown in Figure 4-5. The value of CPE element is fixed at 0.9 and allowing only resistance parameters to change. More details concerning the individual elements and associated physicochemical processes are discussed in section 4.2.1. The contribution of R_{if} related to cathode activation or ORR dominates the total cell resistance as seen from pie diagram in Figure 4-6.

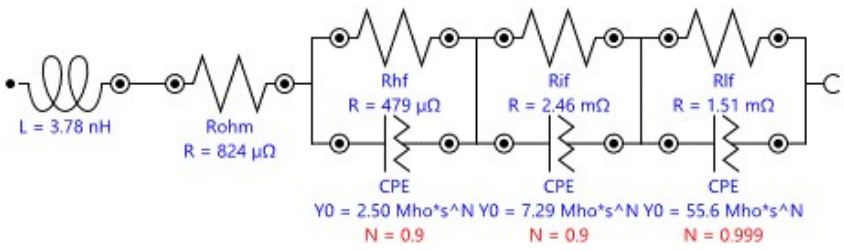

Figure 4-5 EEC used to fit the Nyquist plot in Figure 4-4a.

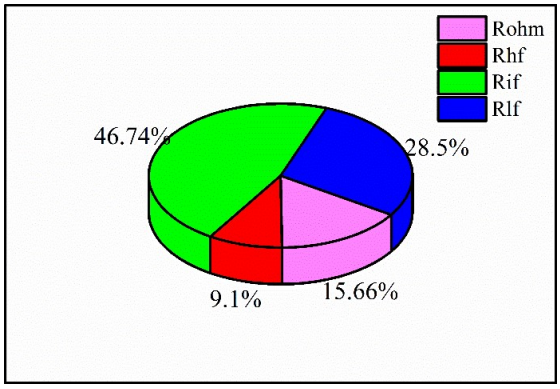

Figure 4-6 Percentage of individual fit parameters obtained from EEC fitting of Nyquist plot at 0.2 A cm-2 and 160°C.

The ohmic resistance is around 0.08 Ω cm^2 and typical value observed in literature [3].

4.1.1.3 CV

After the EIS measurements fuel cell is shut down and cooled to RT to perform CV at three different scan rates 5, 20 and 30 mV s^{-1} and ECSA (is calculated for 0.75 mg cm^{-2} of catalyst) is found to be 16.20, 20.23 and 20.729 m^2 g^{-1} of Pt respectively. The exact cause for the different ECSA values for the same MEA are unknown. Figure 4-7 shows the CV measured at three different scan rates with adsorption/desorption peaks more prominent for CV curve with scan rate of 30 mV s^{-1}.

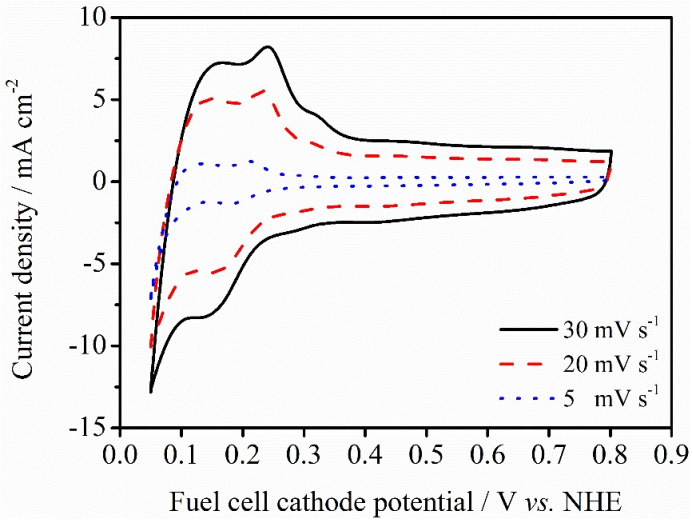

Figure 4-7 CV at RT with three different scan rates 30, 20 and 5 mV s^{-1} in the voltage range of 0.05-0.8 V with 1 SLPM of hydrogen and 1 SLPM of nitrogen on anode and cathode respectively.

4.1.2 The effect of stoichiometry

The influence of anode and cathode stoichiometry on HT-PEMFC performance is studied with polarisation curves. Galbiati et al. found anode stoichiometry (1.3 and 1.75) has no impact on fuel cell voltage [4]. The anode stoichiometry is varied between 1.0, 1.2, 1.5 and 2.0 to verify the influence of hydrogen flow rate on performance of HT-PEMFC at fixed cathode stoichiometry of 2.0. As it can be noticed from Figure 4-8 increasing the anode stoichiometry has negligible influence on the performance of fuel cell with only slight change at higher current densities > 0.9 A cm^{-2} as pointed out in Table 4-1. The increase in anode stoichiometry has negligible effect on performance if pure hydrogen is used [1]. It should be noted that the stoichiometry is maintained at lower current densities as well.

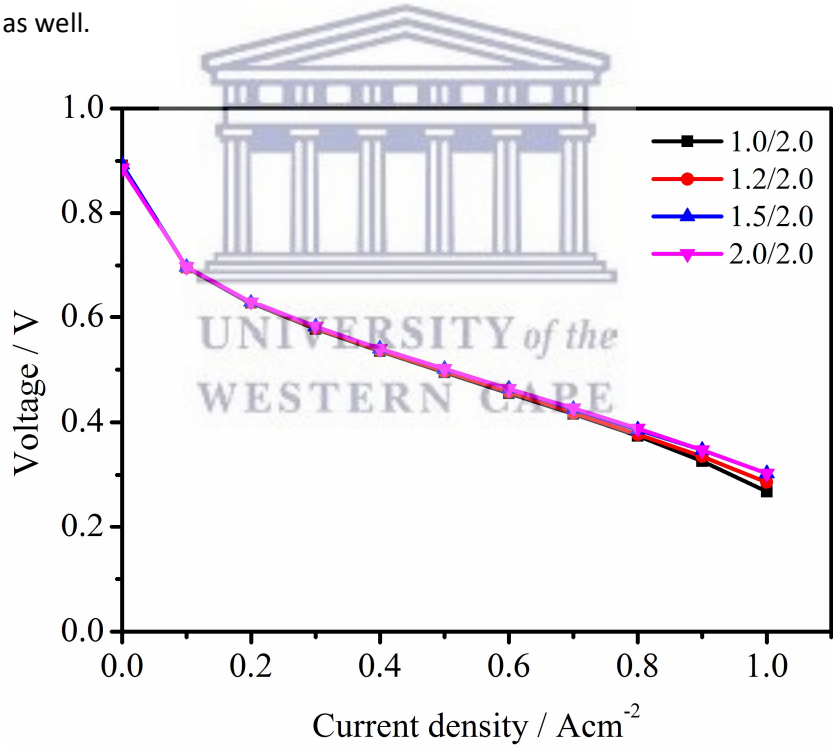

Figure 4-8 Polarisation curves at 160°C and ambient pressure with different anode stoichiometry 1.0, 1.2, 1.5, and 2.0 with constant cathode stoichiometry of 2.0.

However, in the case of HT-PEMFC stack reducing the anode stoichiometry has negative impact but very small (2% power loss) [5]. Janßen et al. noticed when the anode stoichiometry was reduced from 2.7 to 1.3 the performance loss was only 4% and still high cell stability. At lower hydrogen stoichiometry and higher current density cell reversal can happen under hydrogen starvation conditions [6]. In severe cases, it may

result in uneven current density distribution and increased reaction rates of carbon corrosion and water electrolysis. H_2 starvation can be avoided during the operation of the HT-PEM fuel cell by sufficient gas supply and well-designed gas flow field geometry in fuel cell [7].

Table 4-1 Voltage points from polarisation curve at 1.0 A cm^{-2} with different anode stoichiometry and constant cathode stoichiometry.

		Voltage, V @ different Anode stoichiometry			
Cathode stoichiometry	Current density A cm^{-2}	1.0	1.2	1.5	2.0
2.0	1.0	0.268	0.286	0.303	0.303

Similarly, cathode stoichiometry is changed between 2.0, 2.5, 3.0, 4.0 and 5.0 to study its influence on performance of HT-PEMFC at constant anode stoichiometry of 1.2. The cathode stoichiometry has significant effect on polarisation curves as shown in Figure 4-9. The effect is more pronounced for current densities > 0.4 A cm^{-2} as noted in Table 4-2.

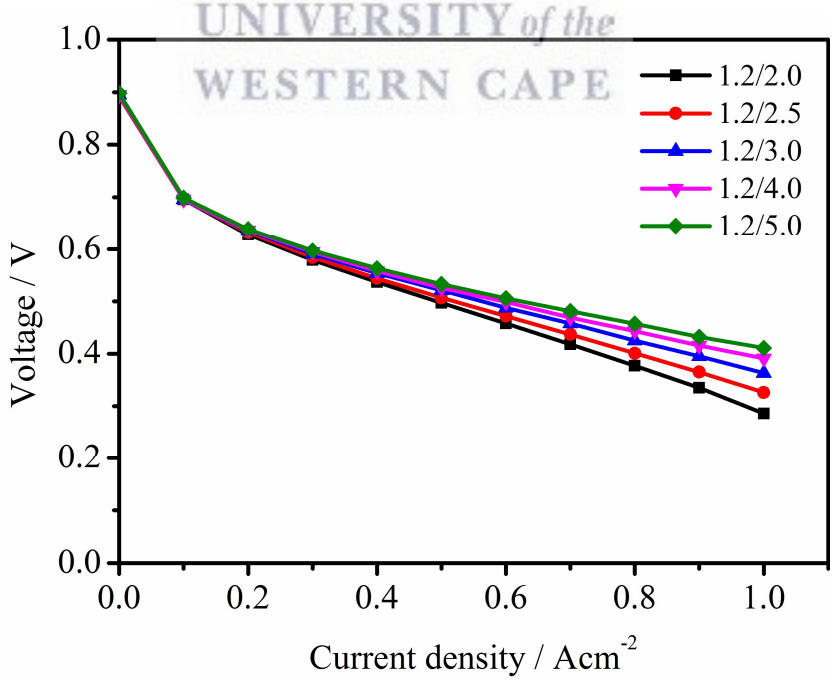

Figure 4-9 Polarisation curves at 160°C with different cathode stoichiometry 2.0, 2.5, 3.0, 4.0 and 5.0 with constant anode stoichiometry of 1.2.

Table 4-2 Voltage points from polarisation curve at 0.4, 0.8 and 1.0 A cm^{-2} with different cathode stoichiometry.

	Current density A cm^{-2}	**Voltage, V @ cathode stoichiometry**				
Anode stoichiometry		2.0	2.5	3.0	4.0	5.0
1.2	0.4	0.537	0.544	0.554	0.558	0.563
	0.8	0.377	0.401	0.425	0.443	0.457
	1.0	0.286	0.326	0.363	0.391	0.411

Increasing the cathode air stoichiometry has a positive effect on HT-PEMFC performance as this increases the oxygen partial pressure causing improvements in thermodynamics and kinetics of fuel cell reactions [3]. According to Nernst equation 4-1, an increase of partial pressure of oxygen improves fuel cell thermodynamics. This improves the fuel cell performance according to equation 4-2 (used to simulate polarisation curve).

$$E^{OCV} = E^{0} + \frac{RT}{2F}\ln\left(\frac{P_{H_2}P_{O_2}^{1/2}}{P_{H_2O}}\right) \quad \text{(eq. 4-1)}$$

$$V_{cell} = E^{OCV} - \eta_c - \eta_a - I_{cell}R_m \quad \text{(eq. 4-2)}$$

Where E^0 is ideal standard potential for fuel cell reaction, P_{H_2O} is partial pressure of water vapour, V_{cell} is the fuel cell voltage at current density I_{cell}, R_m is membrane resistance and η_c and η_a are overpotential related to cathode and anode respectively.

At lower current densities < 0.4 A cm^{-2} there is negligible effect on the proton transfer process inside the catalyst layer with increasing cathode stoichiometry whereas at higher current densities the effect is more pronounced on the gas transfer process inside the catalyst layer. Also at higher current densities water vapour is produced in high amounts on the cathode side and transportation of this water vapour varies with GDL material and there by performance. Increased flow rates on cathode side facilitates rapid removal of water vapour and better cell performance. The effects of cathode stoichiometry are more prominent in a fuel cell with GDL made of carbon cloth compared to carbon paper [1].

Even in the case of stacks the cell voltage increases with cathode stoichiometry. Janßen et al. noticed that the cathode air stoichiometry < 1.3 can be critical for stack due to local oxygen starvation and ≥ 1.5 is possible with fairly stable operation. In practical, increasing air stoichiometry has effect on power consumption of the air blower or compressor. As a compromise between system efficiency and stable stack operation a cathode stoichiometry between 1.5 and 2 is recommended [8].

4.1.3 The effect of temperature

The influence of operating temperature on HT-PEMFC performance is studied at different temperatures 130, 140, 150 and 160°C with polarisation curves. The temperature has positive effect on performance and power density at a particular current density increases with increasing temperature and Figure 4-10 depicts the polarisation curves at different operating temperatures.

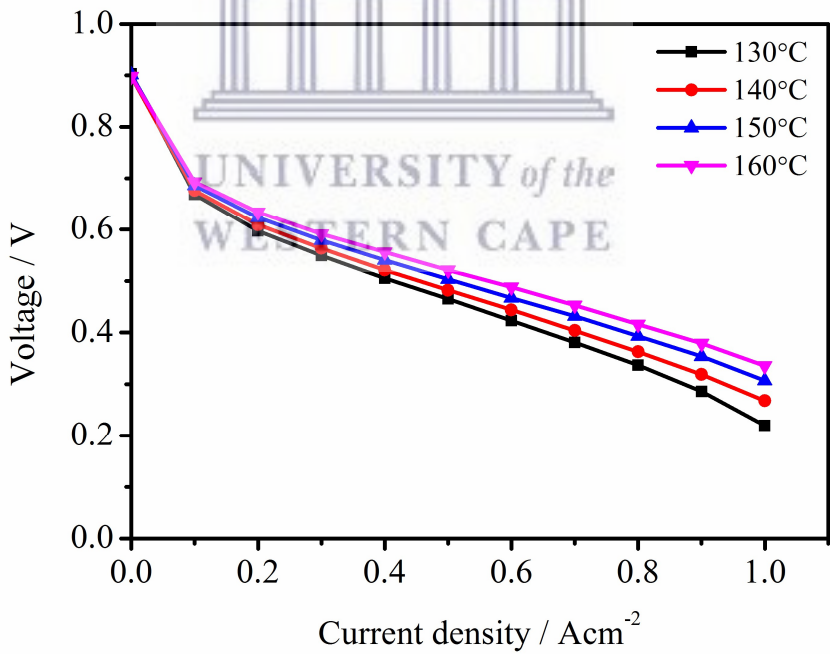

Figure 4-10 Polarisation curves of HT-PEM fuel cell at 130, 140,150 and 160°C with λ = 1.2/2 of H_2/Air are being supplied on anode and cathode respectively at ambient pressure.

The linear increase of power density with increasing temperature (120, 140, 160, 180 and 200°C) is observed by [3]. Temperature has a significant effect on charge transfer and gas diffusion (hydrogen and oxygen) resistance (measured at 160 and 200°C).

Robert et al. showed that higher operating temperatures (120, 140, 160 and 180°C) improve the stack performance and also reduce the negative influence of CO presence on cell voltage uniformity [9]. Kyeongmin Oh et al. and Q Li et al. showed improved CO tolerance with higher operating temperatures and therefore better performance [10], [11].

The performance enhancement at higher operating temperatures can be explained from adsorption behaviour of phosphoric acid on Pt surface. At lower operating temperatures the phosphoric acid anions adsorb over a wider potential window. Increasing the cell temperature leads to a decrease in the PO_4^{3-}coverage and an increase in the PO_4^{3-} mobility respectively resulting in more free Pt sites accessible for reactions to take place on the catalyst surface [12].

Two dimensional numerical model of HT-PEMFC with increasing temperatures of 120, 140, 160 and 180°C showed 1) the cell performance increases due to increase in ionic conductivity and diffusivity of all species, 2) increase in the electrolyte potential of MEA to ~ 63%, 3) effective consumption of hydrogen and oxygen over the catalyst layers due to high electrochemical reaction rate 4) the temperatures through MEA increase linearly towards the cathode from the anode for all the cell operating temperatures [13].

The positive effect of temperature (faster reaction kinetics and higher membrane proton conductivity) for single channel and triple mixed serpentine geometry are validated experimentally and found that the influence of temperature is more pronounced between 100°C and 120°C than between 160°C and 180°C [14]. The ionic conductivity of the phosphoric acid doped PBI membrane is function of temperature according to their proton migration mechanism based on equation 4-3.

$$k_e = \frac{A}{T}\exp\left(\frac{-E_a}{R*T}\right) \quad \text{(eq. 4-3)}$$

Where A is the pre-exponential factor (S.K m^{-1}), E_a is proton conducting activation energy (J mol^{-1}), T is the temperature in (K) and R is ideal gas constant (J mol^{-1} k^{-1}).

The voltage points from polarisation curves in Figure 4-10 are highlighted in Table 4-3 to see the influence of operating temperature on fuel cell voltage.

Table 4-3 Voltage points from polarisation curve at 0.1, 0.2, 0.4 and 0.8 A cm^{-2} at different operating temperatures.

Temperature, °C	**Voltage @ Current density, V**			
	0.1 A cm^{-2}	0.2 A cm^{-2}	0.4 A cm^{-2}	0.8 A cm^{-2}
130	0.668	0.597	0.505	0.337
140	0.676	0.609	0.521	0.363
150	0.686	0.623	0.540	0.393
160	0.693	0.634	0.556	0.416

To get a more detailed insight about effect of temperature in activation region of polarisation curve, the current voltage relationship curves are recorded from 0.01 to 0.1 A cm^{-2} as shown in Figure 4-11a. It is clearly seen that temperature has a positive effect in this region. To find a meaningful relationship Tafel plots are prepared to estimate the activation losses as in Figure 4-11b.

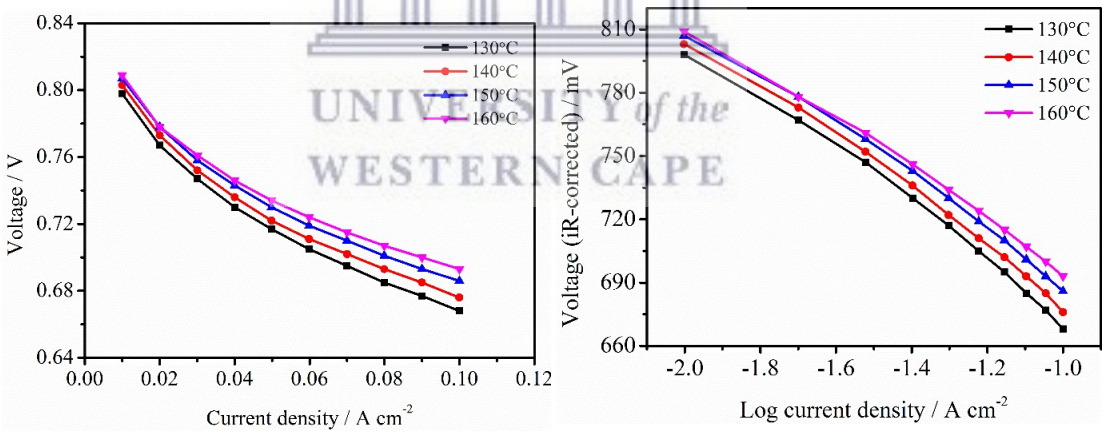

Figure 4-11 a) Polarisation curves of HT-PEMFC at 130, 140, 150 and 160°C with 0.167 and 0.663 SLPM of H_2 and Air on anode and cathode respectively at ambient pressure b) Tafel plots for corresponding curves in Figure 4-11a.

It can be inferred from Figure 4-11b that the slope of associated plots reduces with increasing temperature related to reduced activation losses. The increasing temperatures have a positive effect on intrinsic exchange current density (IECD) of HOR and ORR. The IECD of HOR is much higher (~10^{-3} times) than ORR showing that fuel cell

reaction kinetics is determined by ORR [3]. Activation overpotential of HT-PEMFC is reduced with increasing cell temperature [15].

4.2 EIS of flow field designs

The aim of this work is to study the influence of the flow field designs on HT-PEMFC performance and three flow field designs are investigated using EIS measurements. Graphite plates containing gas flow channels play a crucial role in reactants supply, heat dissipation and maintaining fuel cell operating temperature which influence the performance of fuel cell.

Three HT-PEMFCs are assembled with different flow field plates (Figure 3-1) on cathode side and more details about materials and assembly procedure used for this test are described in section 3.1 and 3.2. The manual test set-up is used for performing experiments. After the break-in at 0.2 A cm^{-2} for 100 hours at 160°C, characterization is performed with EIS spectra at different current densities. The temperature profile during the break-in period is recorded using thermocouple mounted on graphite flow field plate of anode and cathode and temperature data is shown in Figure 4-12. It can be observed from Figure that the stable temperature of 160°C is maintained during break-in of HT-PEMFC.

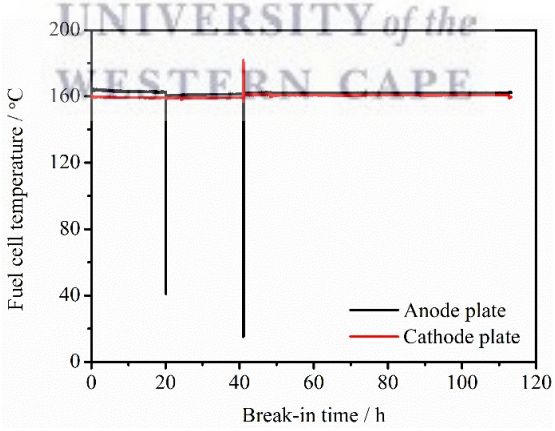

Figure 4-12 Temperature profile during the break-in period (thermocouple is located on graphite bipolar plate).

4.2.1 The effect of current density on EIS

The EIS spectra are obtained according to procedure mentioned in section 3.4.1.2 for HT-PEMFCs with three cathode flow field designs. The Nyquist plot of HT-PEMFC obtained at 0.1 A cm^{-2} is used to explain the various physicochemical process associated

with spectra as shown in Figure 4-13. The spectra has three semi-circles related to high, intermediate and low frequency highlighted with frequency points at 100, 10 and 0.1 Hz. At frequencies greater than 1000 Hz inductance contribution is observed attributed to inductance of wires in the set-up [16]. Chen et al. observed inductance in Nyquist plot at low frequencies <0.3 Hz [17]. The high frequency intercept of real axis in the Nyquist plot represents ohmic loss, R_{ohm} (around 1000 Hz) comparable to the linear part of polarisation curve. The HF semi-circle is due to contribution from the impedance of the HOR on the anode side represented as R_{HF} [18]. The intermediate frequency contribution is the most prominent loop and primarily associated with cathode activation represented as R_{IF}. The ORR is much slower than the HOR. So, the intermediate frequency arc is assumed to be dominated by cathode effects. The low frequency sem-circle is associated with transfer of gas to electrodes represented as R_{LF}. It is mainly governed by mass transfer on the cathode side in terms of convection in the channels of the bipolar plate and diffusion in the GDL and electrodes [19]. The anode has minor contributions to fuel cell losses as the hydrogen gas has better transport capabilities and diffusion than oxygen owing to smaller in size. Schneider et al. reported that the low frequency semi-circle is formed due to sinusoidal oxygen-concentration oscillations within the cathode gas along the flow field [20].

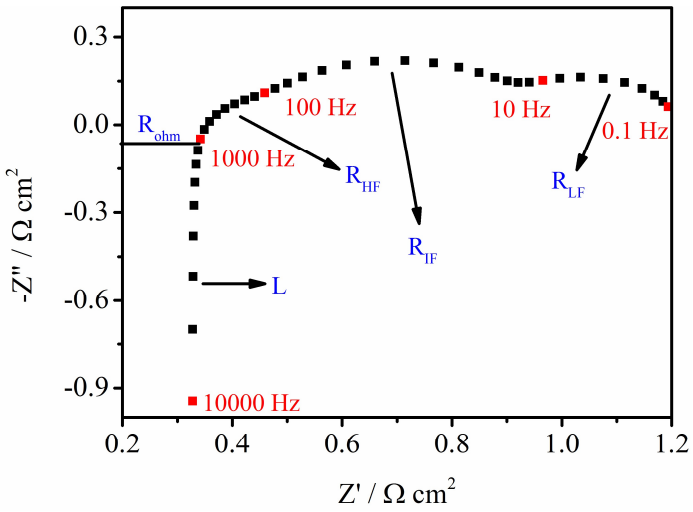

Figure 4-13 Nyquist plot of HT-PEMFC (Celtec-P2100) after break-in with segmented serpentine flow field design on cathode side recorded at 0.1 A cm^{-2} from 10 kHz - 0.1 Hz.

EIS is recorded with three different cathode flow field designs at 0.1, 0.2, 0.4 and 0.8 A cm^{-2}. The cell is pre-polarised between each measurement for 10-15 minutes at respective current density. The Nyquist plots from EIS measurements of three designs are shown in Figure 4-14. It is obvious from the Nyquist plot, the size of the spectra decrease with increasing current density and the same trend is observed with all the designs. This is because of decreasing polarisation resistance with increasing current density as observed in ref. [15]. The spectra obtained for straight and parallel design recorded at 0.1 A cm^{-2} is missing because of technical issues. It can be noticed from the Figure that the inductance contribution is omitted.

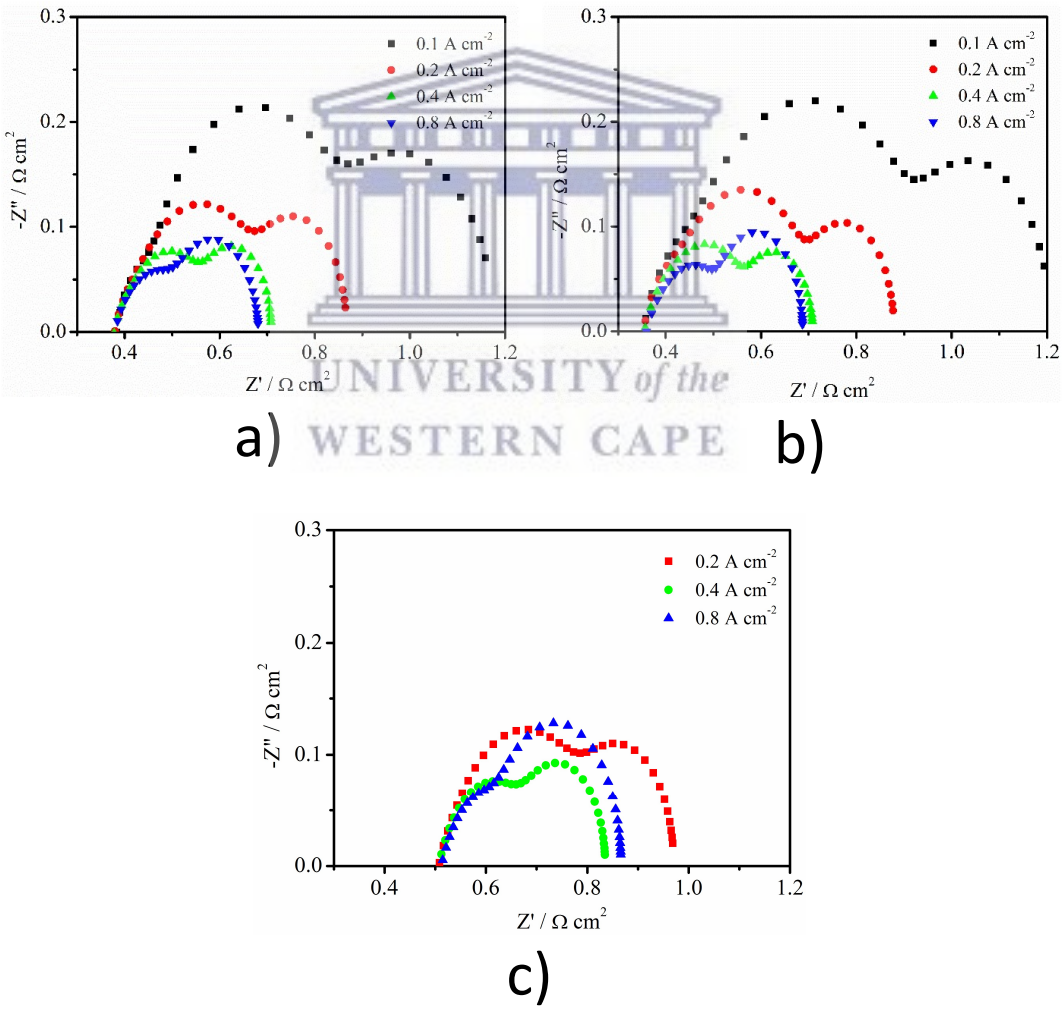

Figure 4-14 EIS spectra (Nyquist plot) of HT-PEMFC (Celtec-P2100) after break-in with a) multiple serpentine, b) segmented serpentine and c) straight and parallel design on cathode side recorded at 0.1, 0.2, 0.4 and 0.8 A cm^{-2} from 10 kHz - 0.1 Hz and 10 mV perturbation voltage.

To get more insights into the individual contributions responsible for observed behaviour of spectra, EEC parameters are estimated. The EEC parameters are obtained by fitting the EEC shown in Figure 4-5. The evolution of individual EEC parameters are shown in Figure 4-15 for three designs. Typically ohmic resistance is about 0.1-0.2 Ω cm^2 for HT-PEMFC. In the experiments as in Figure 4-14 the ohmic resistance is found to be more than 0.2 Ω cm^2 which might be attributed to high contact resistance.

The cell is compressed between endplates with 3 Nm torque and non-uniform compression for three cells could be possible. Even though the ohmic resistance is high the trends of various EEC parameters can be considered and valid and a qualitative understanding is possible.

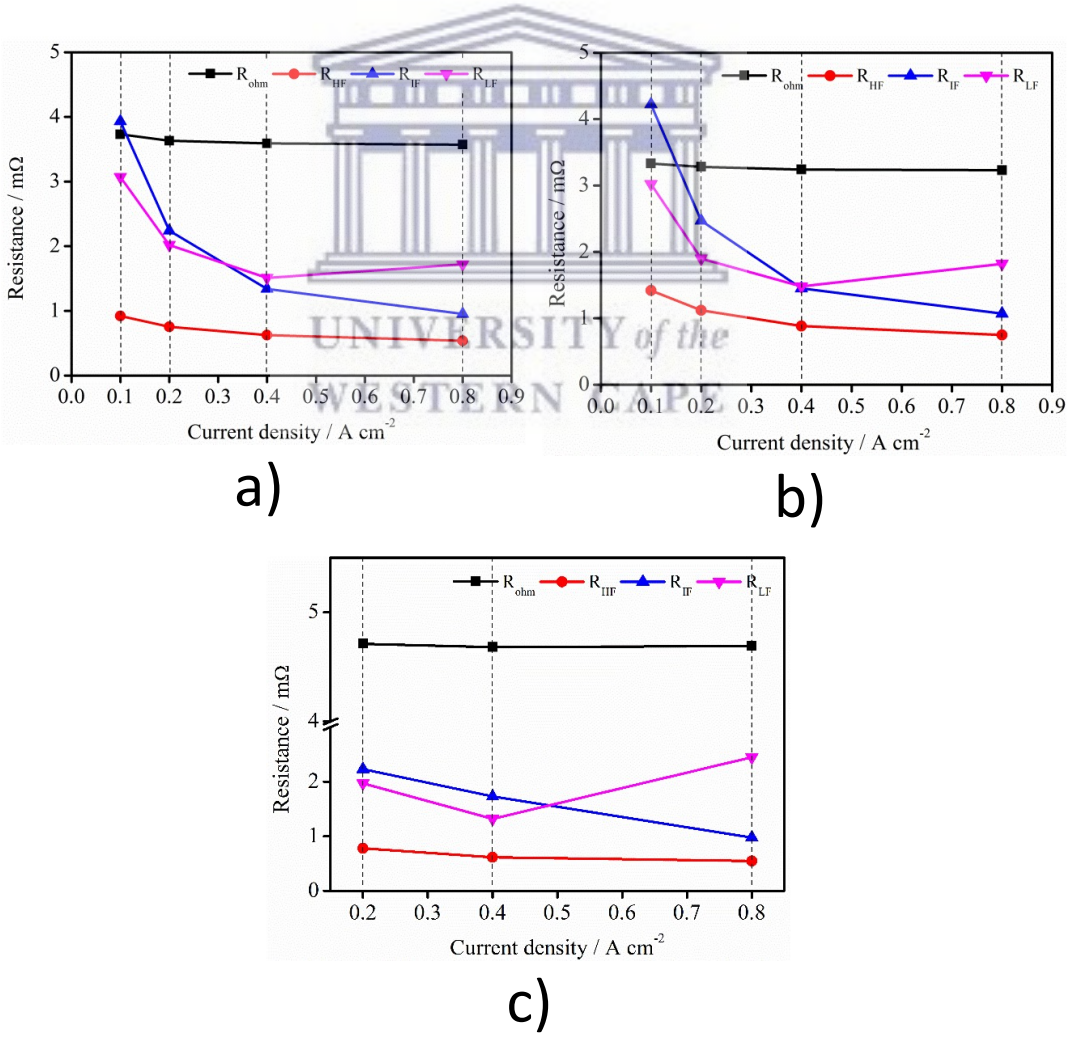

Figure 4-15 Evolution of EEC fit parameters for HT-PEMFC (Celtec-P2100) after break-in with multiple serpentine design, b) segmented serpentine and c) straight and parallel design on cathode side at different cell current densities.

The R_{ohm} slightly decreases with increase of current density at 160°C from 0.1 -0.2 A cm^{-2} for serpentine designs Figure 4-15a and 4-15b. At intermediate current densities, the equivalent humidity inside the fuel cell increases due to increase in rate of water generation from electrochemical reaction. The amount of water adsorbed in the membrane influences the rate of proton conduction and thereby membrane resistance. With higher current densities the water generated at cathode and water removed from the cell are maintaining optimal balance to ensure stable ohmic resistance. The ohmic resistance is almost constant with changing current density for straight and parallel design Figure 4-15c. With increasing current density, there could be increased local temperature and water content leading to higher proton conduction and lower membrane resistance at least theoretically. The proton conduction mechanism of the PBI membrane is proton hopping (the proton transfer from one carrier to another via hydrogen bonds) [21]. During the proton transport there is no net transport of proton carriers across the membrane. (Whereas for the Nafion based MEA the proton conduction happens via vehicle mechanisms the protons diffuse through the medium via solvated hydrogen ion species H_3O^+).

R_{HF} for three designs decreases slightly with increasing current density. Similarly R_{lF} decreases with increasing current density but major drop is observed around 0.1-0.2 A cm^{-2}. The contribution of this parameter is dominating the total cell resistance at low current densities. But at higher current densities R_{LF} dominates the total cell resistance. The low frequency resistance decreases with increasing current density and started to increase from 0.4 A cm^{-2}. As the current density is increased the gas diffusion to catalyst layer is increased because of local temperature rise and further increase in current density results in gas diffusion limitations because of water vapour generated from reaction is not purged with available gas stoichiometry creating problem for mass transport of reactants and products.

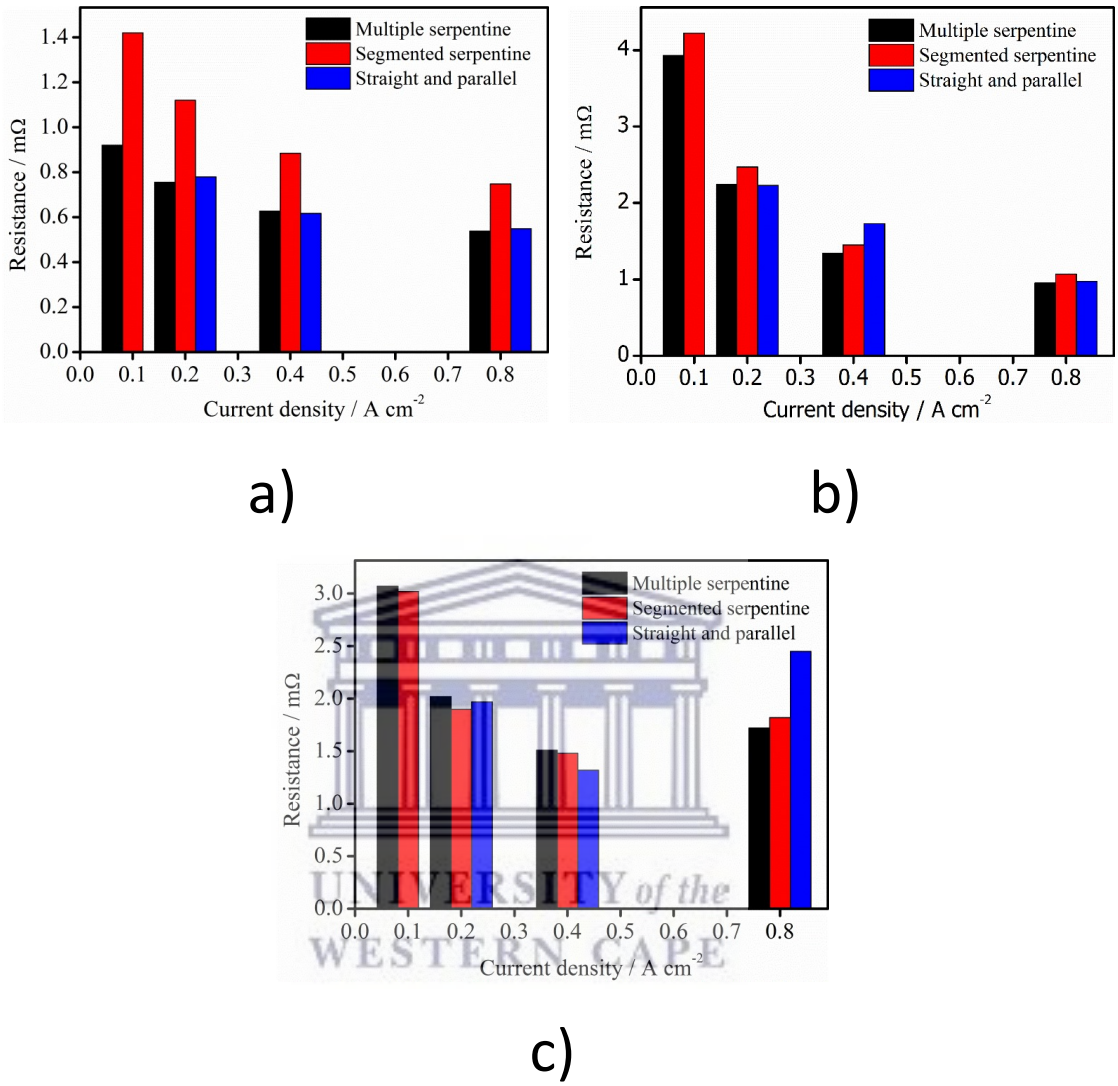

Figure 4-16 Evolution of a) R_{HF}, b) R_{IF} and c) R_{LF} for different flow field designs on cathode of HT-PEMFC at 0.1, 0.2, 0.4 and 0.8 A cm^{-2}.

The individual EEC parameters and their trends with increasing current density are plotted in order to compare three designs as shown in Figure 4-16. R_{HF} slightly decreases with increasing current density for multiple serpentine and straight and parallel design whereas for multiple serpentine the decrease is prominent as in Figure 4-16a. The decreasing behaviour is reported by [22]. Chen CY et al. and S J Andreasen et al. reported increasing trend of R_{HF} with increasing current density and assumed the increase is related to intermediate frequency semi-circle and not the HF semi-circle [17], [23]. The R_{HF} values obtained are almost close to ref. [23]. R_{IF} decreases with increasing current density and the values obtained are close to ref. [23]. The resistance is reduced

significantly with increasing current density (0.1-0.2 A cm^{-2}) and this behaviour reflects the slope of the activation related part of the polarisation curve which approaches zero with increasing current. The acceleration of electrons at high current density enhances the charge transfer process and lowers the impedance of ORR process observed from Figure 4-14, 4-15 and 4-16c and from current densities > 0.4 A cm^{-2} the resistance drop is not significant. The charge transfer resistance decreases with increasing current density. In the low current region ORR at cathode dominates while HOR at anode is negligible. Mass transport losses picked up with increasing current density and the same trend repeats for three designs as shown in Figure 4-16c. R_{LF} decreases initially and then increases with increasing current density especially at 0.8 A cm^{-2} for straight and parallel is slightly higher compared to serpentine. According to Jespersen et al. the low frequency semi-circle vanished with air stoichiometry > 4 [24]. At high current densities mass transfer resistance is main contributor because gas concentration in the GDL decreases at elevated current densities [17].

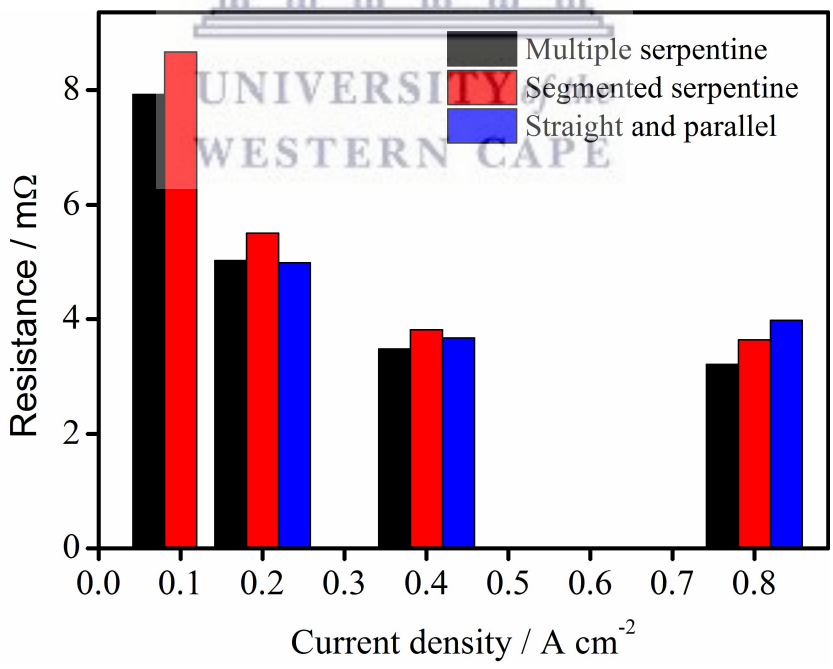

Figure 4-17 Total resistance of HT-PEMFC with different flow field designs on cathode measured at 0.1, 0.2, 0.4 and 0.8 A cm^{-2}. Note: Ohmic resistance is subtracted from total resistance.

The membrane resistance is subtracted from total cell resistance and plotted in Figure 4-17 as a comparison for three designs with increasing current densities. It can be observed that segmented serpentine show higher cell resistance compared to multiple serpentine design. Whereas, straight and parallel design show similar resistance as multiple serpentine design but with a slight change at high current density. At intermediate current densities the resistance of cell decreases because the contributions from R_{IF} (charge transfer resistance) decreases. At high current densities the contribution of gas transfer resistance is increased and this is attributed to following reasons. The resistance to proton conduction increases as the gas stoichiometry increases because the partial pressure of water in the cathode is reduced [25], [26]. At such conditions along with high cell operating temperatures, two processes may occur 1) phosphoric acid is being dehydrated and pyrophosphoric acid or other dimerised products are being formed as in equations 4-4 and 4-5) and hydration of the latter when exposed to water vapour and formation of phosphoric acid [27]. The two reactions are reversible and equilibrium concentrations of these reactions depend on temperature and RH. The dimerised products are less proton conductive than phosphoric acid [19].

$$2H_3PO_4 \leftrightarrow H_4P_2O_7 + H_2O \quad \text{(eq. 4-4)}$$

$$H_4P_2O_7 + H_3PO_4 \leftrightarrow H_5P_3O_{10} + H_2O \quad \text{(eq. 4-5)}$$

EIS is recorded with three flow field designs at 0.1, 0.2, 0.4 and 0.8 A cm^{-2}. The stoichiometry of 1.2 and 2 is used for H_2 and air on anode and cathode of fuel cell respectively which is sufficient for electrochemical reaction. Overall, the results show that multiple serpentine with lower internal cell resistances compared to other two designs at different current densities measured in this test. The straight and parallel designs showed low cell resistance (similar to multiple serpentine) only at low current density however, the trend changes at high current density. The advantage with this kind of design is low R_{LF} compared to other designs which is important factor considering the pressure drop and parasitic losses from system point of view. The results should also be confirmed by measurements using a more sophisticated test set-up to clearly isolate the flow field effects on performance parameters of HT-PEMFC.

4.3 Long term stability studies

The fuel cell is assembled with three different cathode flow field design as shown in Figure 3-3 with BASF Celtec®-P2100 MEA of 96 cm^2 geometrical area using quick connect fixture shown in Figure 3-4 of section 3.2. After the break-in operation for 100 h as mentioned in section 3.3, the three single HT-PEMFCs are allowed to operate for duration of 500 h to check the stability of MEA performance at 0.2 A cm^{-2} with three different flow geometries. The details of long term stability test procedure is given in section 3.3.1. The evolution of voltage profile at the applied current density with three flow patterns is shown in Figure 4-18. It can be observed from the Figure 4-18, that the fuel cell with straight and parallel design showed better voltage profile compared to multiple serpentine design from the beginning of test. The fuel cell with segmented serpentine design showed lower cell voltages compared to other two designs from the initial test period with difference being more obvious after the activation period and until the end of test period.

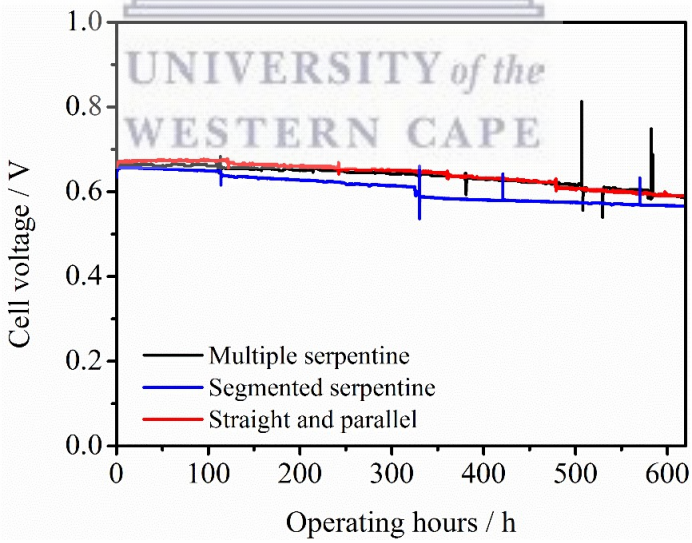

Figure 4-18 Fuel cell voltage profile with multiple serpentine design, segmented serpentine and straight and parallel flow field geometry on cathode side of HT-PEMFC at 160°C and 0.2 A cm^{-2} with stoichiometry of 1.2/2 of H_2/Air for anode and cathode respectively.

The three fuel cells showed similar behaviour (increasing cell voltage) during first 20 h of activation period. This kind of increasing cell voltages during the break-in period is common for HT-PEM MEA. Schenk et al. observed a steep increase of the cell

performance in the first 14 h of operation and voltage gain is ascribed to the redistribution of the electrolyte within the cathode catalyst layer after hot-pressing and to a further cleaning of the catalysts surface [28]. The multiple serpentine design showed maximum cell voltage of 0.664 V for first 20 h with little fluctuation thereafter for the rest of activation period with a peak voltage of 0.666 V. The segmented serpentine design showed 0.656 V of maximum cell voltage during first 20 h of activation period. The straight and parallel design showed maximum cell voltage of 0.674 V in first 20 h and stabilised for entire activation period. The flow fields investigated have some influence on cell voltages during break-in period.

The three fuel cells are operated for ~600 h including the break-in period, the exact operating hours are provided in Table 4-4. The fuel cell with multiple serpentine design is operated for 579 h including 110 h of activation period with degradation rate of 53 µV h^{-1}. The cell experienced unexpected shut downs during the last 100 h of operation which is visible in Figure 4-18. The fuel cell with segmented serpentine design showed voltage degradation of 106 µV h^{-1} during an operation period of 659 h which is highest compared to other two designs. The straight and parallel design showed degradation rate of 69 µV h^{-1} and operated for 622 h. The straight and parallel designs showed better cell voltage but with time the cell voltages started to gradually decline by the end of period.

Table 4-4 Operating hours, degradation rate and linear fit parameters of long term stability tests for HT-PEMFCs at 0.2 A cm^{-2} and 160°C.

Flow field design type	Operating hours (including activation period)	Degradation rate µV h^{-1}	Linear fit
Multiple serpentine	579.18	53.523	$y = -1.18486 * 10^{-4}x + 0.67366$ $R^2 = 0.924$
Segmented serpentine	659.416	106.154	$y = -1.70992 * 10^{-4}x + 0.65975$ $R^2 = 0.941$
Straight and parallel	622.18	69.118	$y = -1.47151 * 10^{-4}x + 0.68693$ $R^2 = 0.945$

The degradation rates are calculated based on initial cell voltages observed at break-in period.

4.3.1 In-situ characterization

4.3.1.1 Polarisation curves

To get more insights into voltage behaviour during the constant current operation electrochemical characterization studies are performed. The fuel cell operation is interrupted for polarisation curves and EIS at BoL, 100, 250, 350 and 500 h of operation (Note: approximated hours are mentioned). The polarisation curves for segmented serpentine design are recorded at BoL, 200 and 500 h. The polarisation curves for three designs in Figure 4-19 show decreasing trend of performance with increasing operation hours. The segmented serpentine showed significant drop in performance during long term stability tests (observed from slope of voltage profile) observed in Figure 4-19b. The activation losses for three designs increase with operating hours.

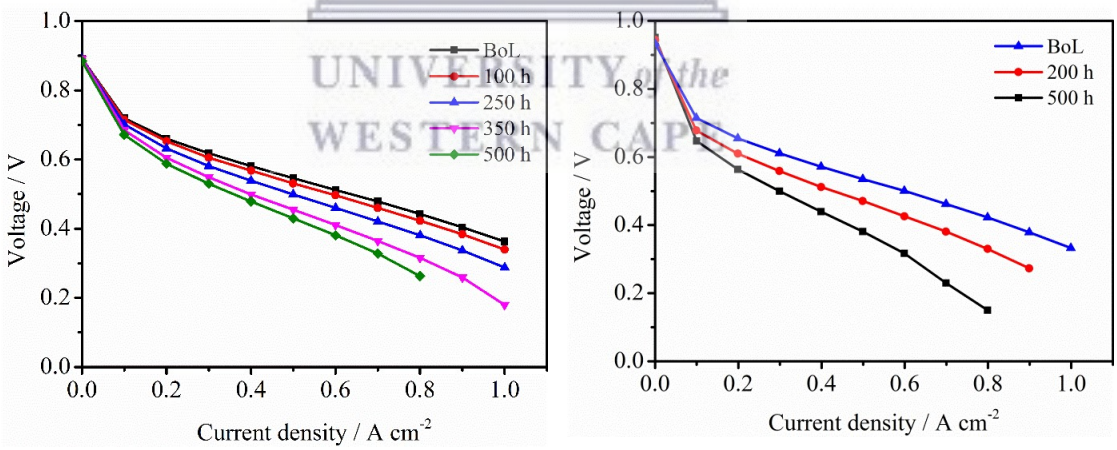

a) b)

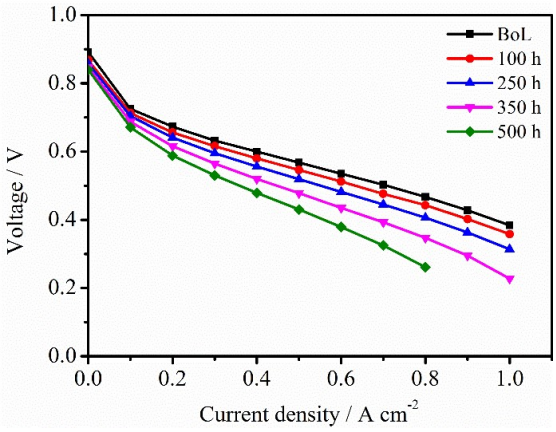

c)

Figure 4-19 Polarisation curves during the long term stability test of 500 h for HT-PEMFCs with a) multiple serpentine b) segmented serpentine c) straight and parallel at 160°C and ambient pressure with stoichiometry of 1.2/2 of H_2/Air for anode and cathode respectively.

The straight and parallel design as mentioned earlier had better cell voltages from break-in period compared to multiple serpentine design as shown in Figure 4-20. This is supported by the fact that the BoL performance of straight parallel design have significantly higher performance compared to multiple serpentine design.

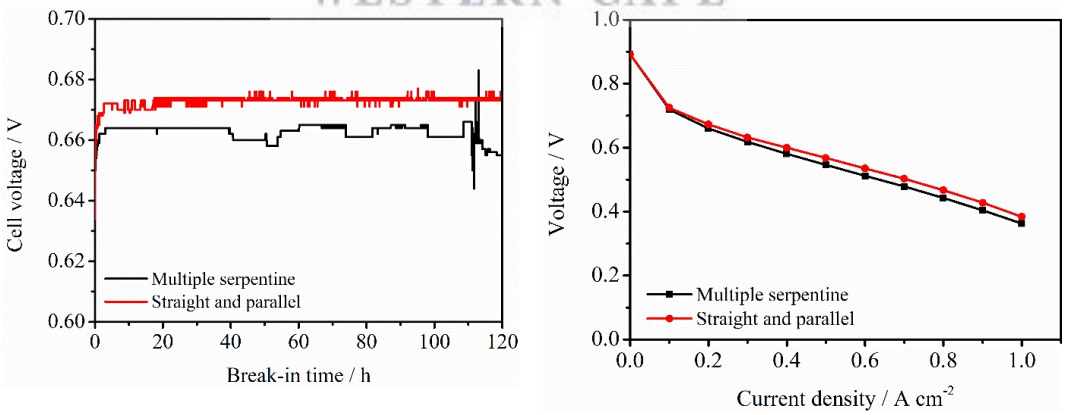

a) b)

Figure 4-20 Comparison of a) break-in period b) polarisation curves at BoL for multiple serpentine and straight and parallel designs.

To investigate the influence of flow fields at higher current densities the voltage points from polarisation curves at 0.8 A cm^{-2} are compared for multiple serpentine and straight

and parallel designs as shown in Figure 4-21. At higher current densities mass transport losses dominate the performance loss resulting in lower cell voltages. Both multiple serpentine and straight and parallel designs show decreasing trend of voltages with increasing operation time but the multiple serpentine showed significantly lower cell voltages compared to straight and parallel design however at the end of test this trend is reversed.

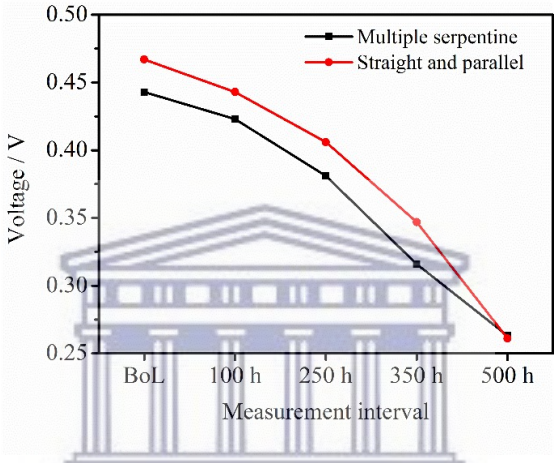

Figure 4-21 Comparison of voltage points from polarisation curves at 0.8 A cm^{-2} for multiple serpentine and straight and parallel designs.

4.3.1.2 EIS

EIS spectra is recorded to assist in further investigation of long term stability tests. The Nyquist plot for multiple serpentine and straight and parallel design is shown in Figure 4-22 and unfortunately, the EIS data for segmented serpentine is found to be missing and could not be retrieved from system. The spectra obtained are typical of HT-PEMFC and details of various elements of spectra are discussed already refer to section 4.2.1. The resistance related to intermediate frequency increases observed from increasing diameter of semi-circle. The ohmic resistance has not changed with operation for multiple serpentine design but the charge transfer resistance of cathode increases with time and especially the difference between the spectra at 250 and 350 h is significant.

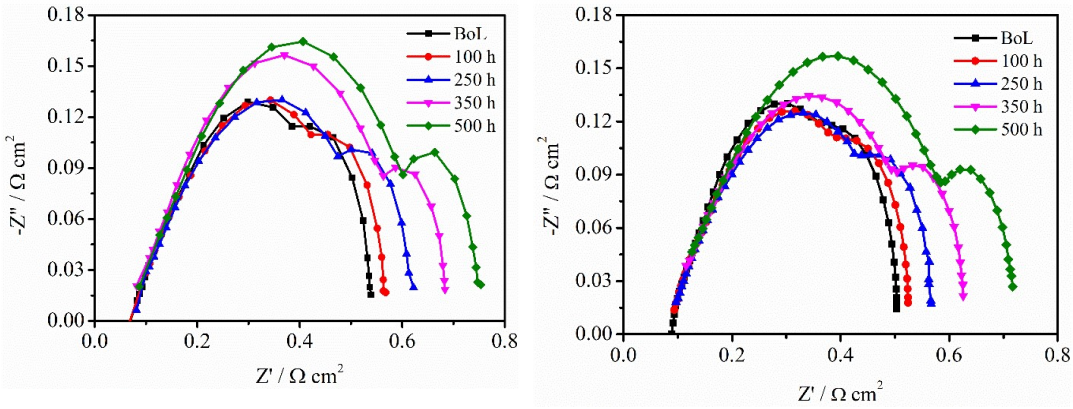

Figure 4-22 Nyquist plot of a) multiple serpentine b) straight and parallel design at 0.2 A cm^{-2} and 160°C from 10 kHz - 0.1 Hz with 10 mV perturbation voltage.

Similarly, the straight and parallel design has no influence on ohmic resistance with operation time but cathode resistance increases significantly after 350 h of operation. Similarly, in a 500 h continuous aging test on HT-PEMFC performed by J Hu et al. The cell performance began to degrade after break-in period (150 μVh^{-1} at 0.640 A cm^{-2}) but with stable internal resistance and the increase of charge transfer resistance confirmed from impedance studies because of degradation of catalyst [29]. To compare the results of EIS spectra of multiple serpentine and straight and parallel flow fields, polarisation resistance is plotted in Figure 4-23. The multiple serpentine shows comparatively higher cell resistance with operation.

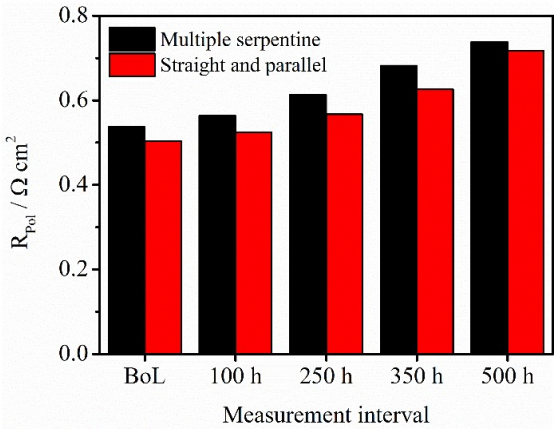

Figure 4-23 Comparison of total cell resistance (R_{pol}) for multiple serpentine and straight and parallel design from Nyquist plot in Figure 4-22.

4.3.1.3 CV

The voltammetry studies confirm the ECSA available for electrochemical reaction. The CV of three designs is shown in Figure 4-24 and for segmented serpentine the CV curves are recorded only twice and one at EoT could not be obtained. The adsorption/desorption area from CV curves decrease with operation time.

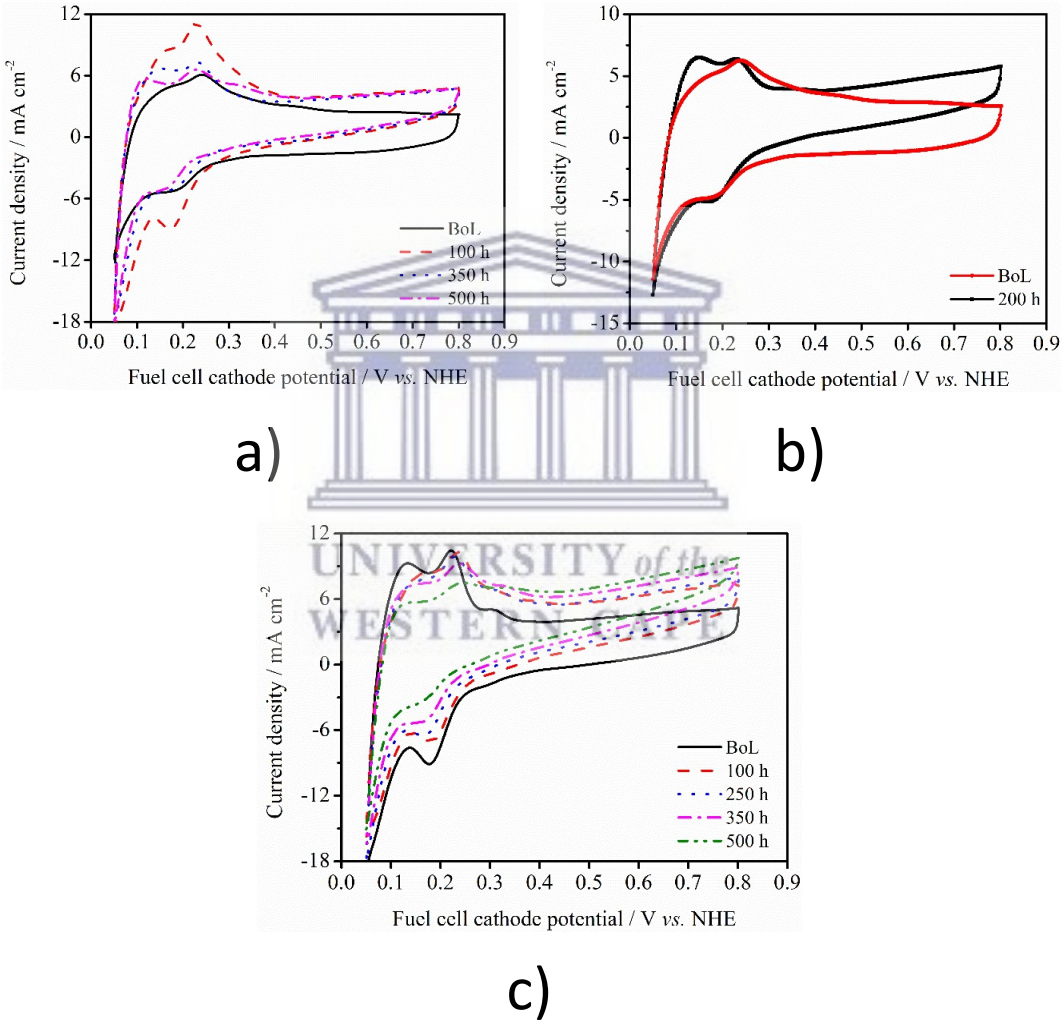

Figure 4-24 CV of a) multiple serpentine (CV at 250 h could not be obtained) b) segmented serpentine c) straight and parallel design.

The ECSA is calculated from equation mentioned in section 3.4.1.3 and details of obtained results are shown in Table 4-5. The ECSA decreases with time during long term stability tests with all the designs and the exact reasons are not known. The PO_4^{3-} adsorption on the electrode can interfere with CV measurements at room temperature

resulting in poor CV curves. The multiple serpentine design has lower ECSA at BoL compared to after 100 h of operation followed by decreasing trend. Overall, the ECSA decreases with constant current operation attributed to early degradation of catalyst because of agglomeration and particle sintering. Similar behaviour in the early life of fuel cell is investigated in literature. The long term stability tests of Pt/C catalyst investigated by Zhai et al. found that during the first 300 h, the ECSA decreased from 17.2 to 7.8 m^2 g^{-1} Pt confirmed from CV which is equal to about 55% and small decrease about 5% in the next 210 h [30].

Table 4-5 ECSA of fuel cell with three different flow field designs from long term stability tests.

Operating hours	**Multiple serpentine**	**Segmented serpentine**	**Straight and parallel**
h	$m^2 g^{-1}$ of Pt		
BoL	14.31	14.51	18.73
100	22.2	NA	15.4
250	NA	12.53	13.44
350	12.5	NA	9.92
EoT	9.65	NA	6.65

4.3.1.4 LSV

The LSV is measured for fuel cells with three designs to investigate performance loss due to hydrogen crossover and internal short-circuit. The LSV curves for three designs at BoL and EoT is shown in Figure 4-25. The hydrogen crossover current is measured from LSV curves as mentioned in section 2.3.4 for three designs at BoL and EoT of long term stability tests. The hydrogen crossover current values did not change significantly for multiple serpentine design however for segmented serpentine and straight and parallel design the hydrogen crossover current has increased slightly from 1 to 2.5 mA cm^{-2} and 0.8 to 1.2 mA cm^{-2} respectively. The acceptable value for hydrogen crossover is 2 mA cm^{-2}. The insignificant crossover current values suggest that fuel cell has not suffered from hydrogen crossover and membrane is not damaged.

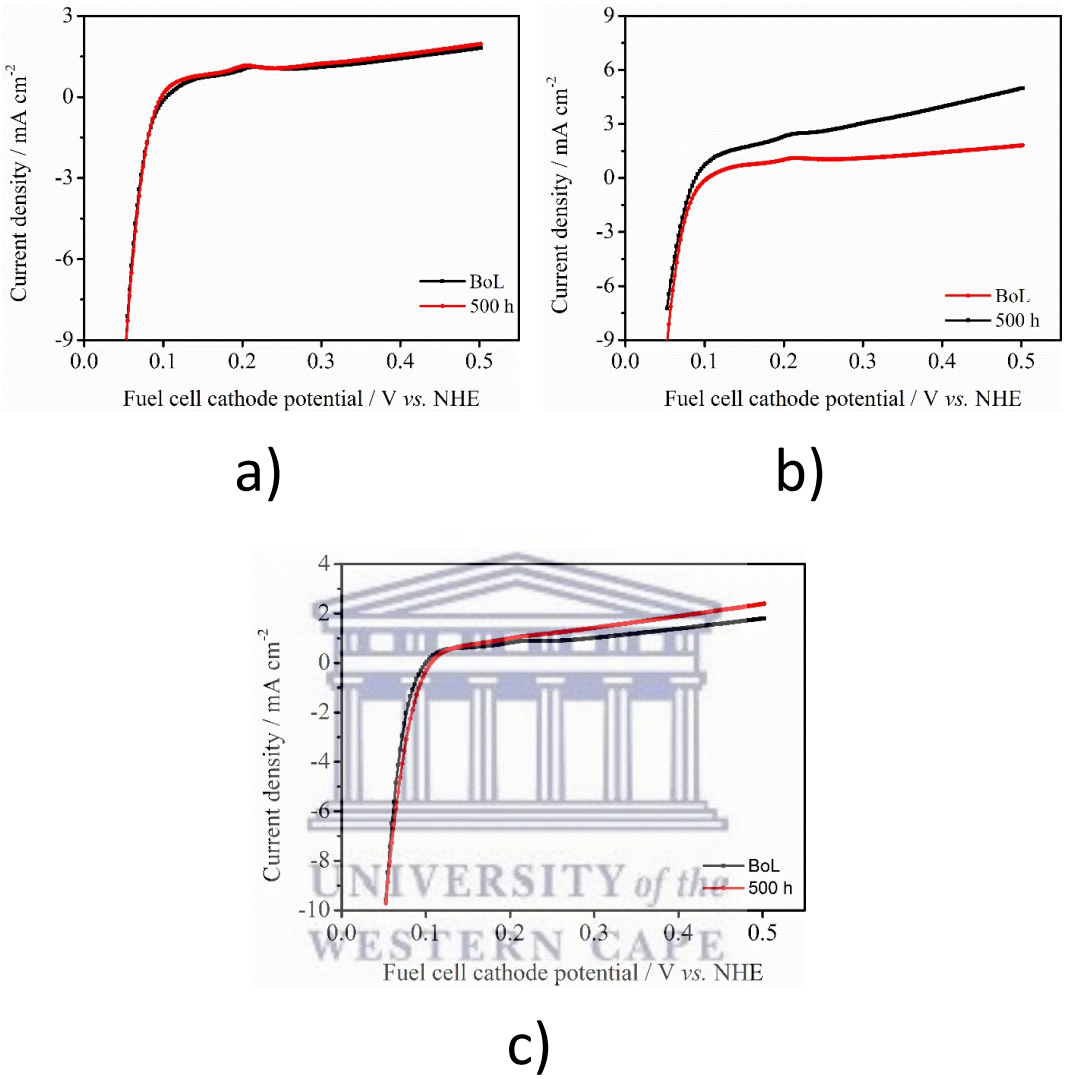

Figure 4-25 LSV of a) multiple serpentine b) segmented serpentine c) straight and parallel design.

4.3.2 Post-mortem analysis

4.3.2.1 TEM

The post-mortem analysis is performed only for multiple serpentine and straight and parallel designs and not for segmented serpentine design due to non-availability of MEA. After the long term stability tests the catalyst from both side of MEA is scraped and collected for TEM and XRD analysis. Apart from this a piece of MEA is cut for SEM analysis. The TEM images are obtained and processed as mentioned in section 3.4.2.3.

The images of fresh and long term tested catalyst (scraped from MEA) are shown in Figure 4-26 of both multiple serpentine design and straight and parallel design.

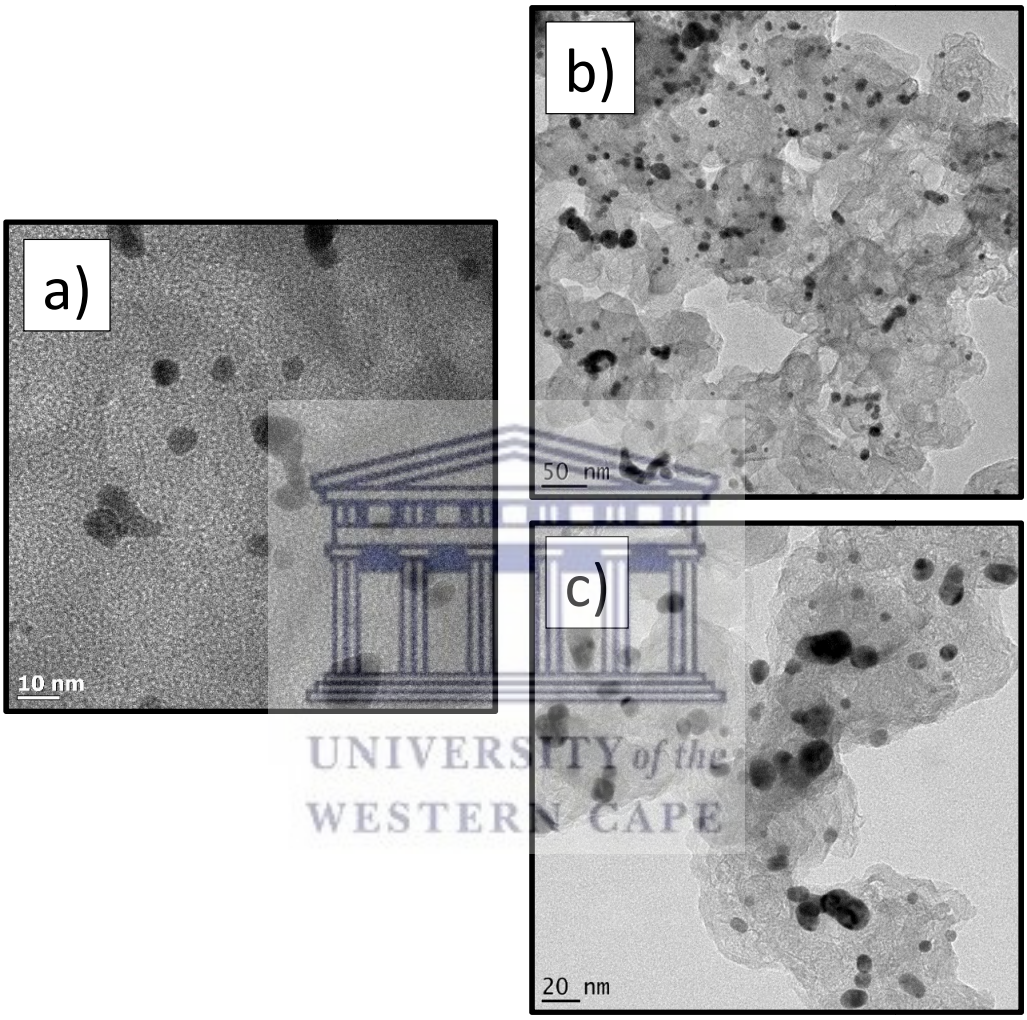

Figure 4-26 TEM images of a) fresh and long term tested cathode catalyst of b) multiple serpentine and c) straight and parallel design.

The particle size distributions are determined by measuring the platinum particles randomly selected in each TEM image. The corresponding particle size distributions of fresh and tested catalyst is shown in Figure 4-27. It can be noticed that the mean particle size has increased from 4.1 ± 1.2 nm for a fresh catalyst to 6.4 ± 1.9 and 7.0 ± 1.9 nm for fuel cell with multiple serpentine and straight and parallel design on the cathode side respectively. Performance loss due to particle agglomeration and ECSA loss in early life of fuel cell is observed in literature. The TEM results of long term stability tests of Pt/C

catalyst investigated by Zhai et al. showed that the Pt particle size in the cathode increased from 4.0 to 8.3 nm before and after 300 h with no Pt depositions in PBI membrane [30]. They concluded agglomeration of platinum particles occurred via coalescence mechanism on carbon at the nanometer scale.

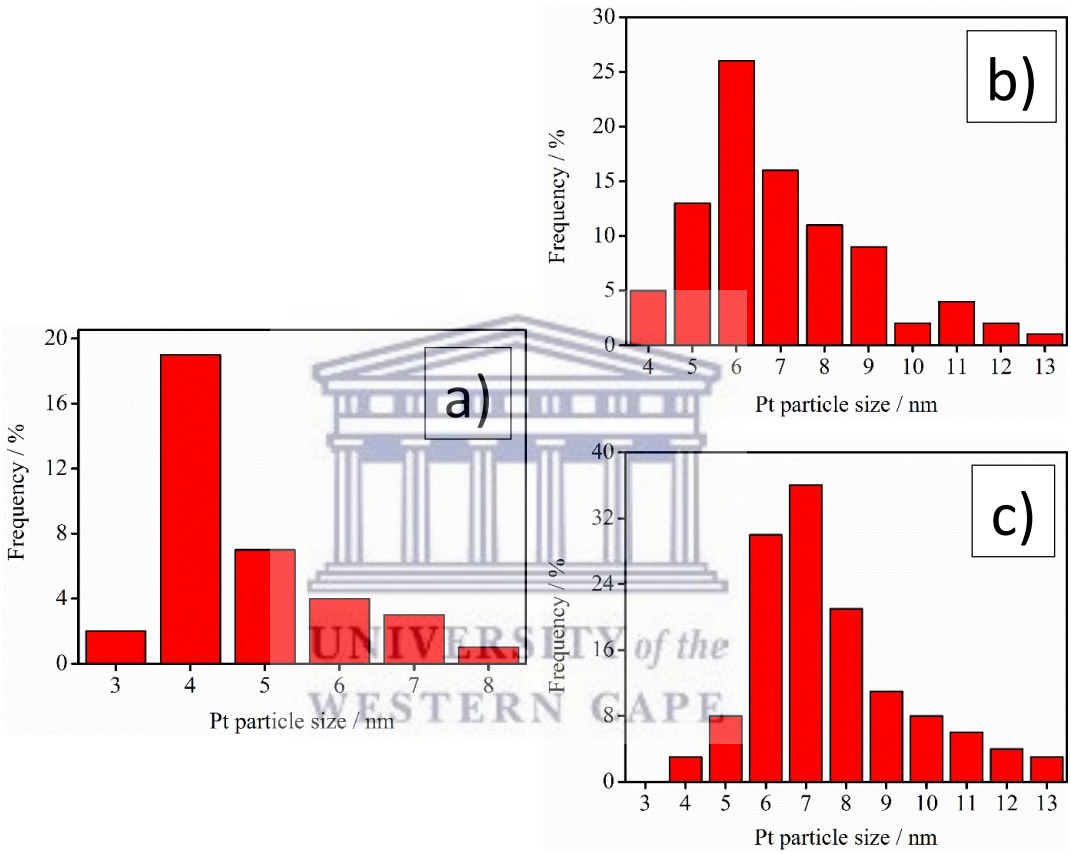

Figure 4-27 TEM particle size distribution of a) fresh and long term tested cathode catalyst of b) multiple serpentine and c) straight and parallel design.

4.3.2.2 XRD

The XRD images for catalyst powder also confirm the growth of crystallite size for long term tested catalyst compared to fresh or untested MEA (catalyst) as shown in Figure 4-28. The mean crystallite size of Pt nanoparticles is obtained by applying Scherrer's equation from width of Pt (220) peak. The calculated values as shown in Table 4-6 are within the same order of magnitude of those measured on the TEM images. There are discrepancies in the measured results between TEM and XRD for sample c, d, e and f and this is because of different instrumentation and measurement principle.

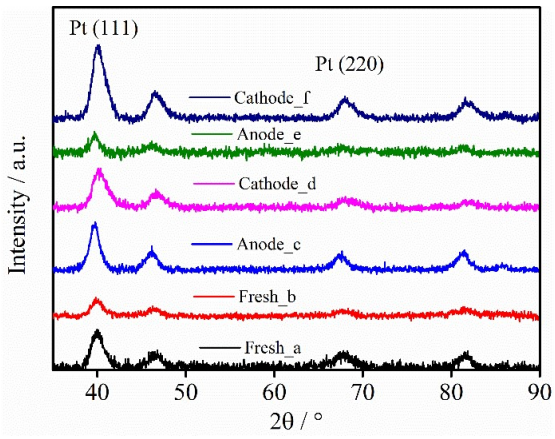

Figure 4-28 XRD (with Y offset values) of fresh and long term tested MEA (catalyst) with multiple serpentine design and straight and parallel design on cathode.

Table 4-6 shows the crystallite size obtained from Pt (220) peak with peak positions (2 theta values) typical of Pt (fcc) 67.6.

Table 4-6 Pt crystallite size and 2θ values from Pt (220) peak for fresh and long term tested MEA with multiple serpentine and straight and parallel design on cathode side.

Sample label	Sample description	2 theta / °	Crystallite size / nm	Sample type
a	Powder	67.6	3.7	Fresh catalyst
b	CCM	67.7	3.7	
c	Multiple serpentine_cathode	67.5	6.9	Long term tested catalyst
d	Multiple serpentine_anode	68.0	4.6	
e	Straight and parallel_cathode	67.5	6.2	
f	Straight and parallel_anode	67.9	5.0	

The peak positions of cathode catalyst after the long term-stability test changed slightly and this is because of alloy composition on cathode side.

4.3.2.3 SEM

The SEM images of used MEA are collected to identify the changes in surface morphology and cross-sectional thickness changes because of long term operation. After 500 h of operation the various layer of MEA remain intact and are not affected by operation. The backscatterd image of MEA resulting from long term operation with multiple serpentine design on anode and cathode is shown in Figure 4-29. Membrane thinning and catalyst layer thinning is not observed. Membrane thinning and acid loss is observed only after long term operation of several thousand hours (17000 h) [31]. The CL corrosion is observed by reduction in thickness of cathode from 30 to 8 µm and anode unchanged (6 µm). XRD showed the crystallite size of anode increased from 3 to 4.6nm and cathode 3.3 to 8.9 nm after long term operation supported by TEM studies.

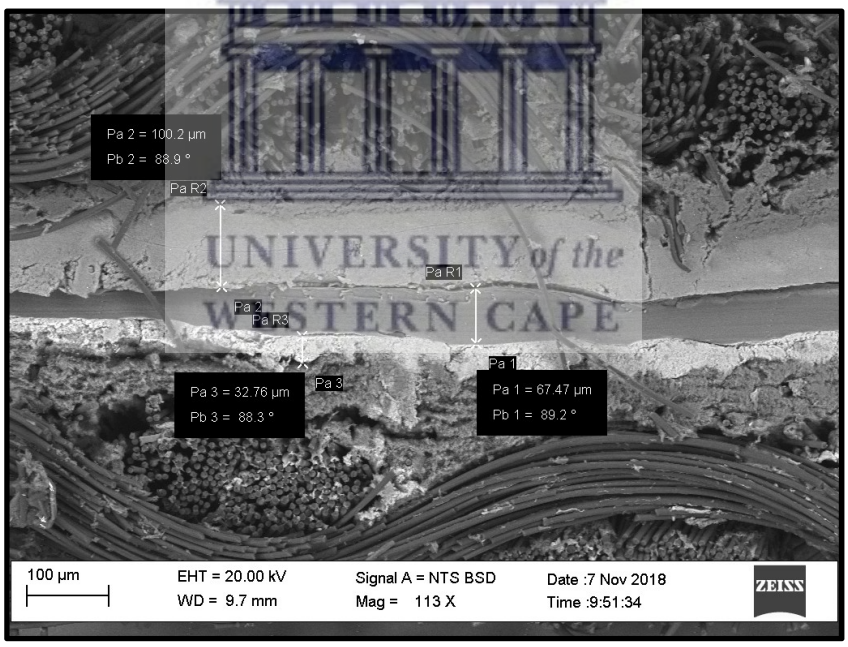

Figure 4-29 SEM cross-sectional image of Celtec®-P2100 MEA after long term stability with multiple serpentine design on cathode side.

The post-mortem characterization results confirm the growth of Pt particles on cathode and possible cause for loss of ECSA of Pt. The sintering rate is faster in the cathode than in the anode and the difference is attributed to the different environments of potential and water vapour density of the cathode and anode [32].

Overall, the straight and parallel design showed better performance over long term stability tests however, the voltage behaviour of multiple serpentine cannot be ignored. The results of long term stability tests confirm that the cathode side flow-field layout is one major optimization parameter in order to increase the performance and equally distribute the oxygen [33] and maintain uniform current density distribution (gradient). With the advances in CFD, it is now possible to optimize the flow-field structure and minimize current density distribution gradients over the MEA [34]. The flow field plate design must address these issues, together with a low pressure drop along with the mass and heat flows in cells. Maintaining uniform current density distribution by ensuring adequate oxidant and fluid flow is crucial in cells with large geometrical area [35]. The mean velocities of similar kind of straight and parallel design are studied with the aid of simulation and found to be slightly lower when comparing them to serpentine flow fields and only a low pressure loss occurs with quite uniform flow distribution in their straight (parallel) gas channel segments (i.e. central region of the active area). For HTPEMFCs, to substantially improve flow fields, it is required to modify the position of the inlet and outlet or to design a gas distributor before entering the active area. This will probably lead to more uniform distribution [36]. The current study highlights the use of straight and parallel design on cathode flow plate to achieve superior performance over both serpentine designs and possible operation with low pressure drop and uniform current distribution. Even though the degradation rates achieved in this study are quite high compared to literature the continuous (without shut-down) and uninterrupted (limited characterization studies) operation at slightly high reactant stoichiometry will guarantee low degradation rates with multiple serpentine and straight and parallel designs.

4.4 Potential cycling test

In this section potential cycling AST procedure mentioned in section 3.3.2 is applied on three unit cells with different cathode flow fields shown in Figure 3-3. The observed current density profile when cycling the fuel cell potential between 0.5 V and 0.9 V for three cathode flow field designs is presented in Figure 4-30. The potential cycling has significant impact on HT-MEA performance over the duration of AST period. The trend of current densities observed at 0.5 V decreases with increasing cycle number. It can be noticed from Figure 4-30 the total number of cycles performed on each HT-MEA is different depending on the performance obtained at EoT with associated design. The performance of fuel cell at EoT is ~40 % of the initial performance at 0.5 V observed for all the three designs. Multiple serpentine design operated for the longest duration of 482 h (4821 cycles) compared to segmented serpentine reaching similar performance by EoT in 367 h (3677 cycles) of cycling. The HT-MEA with straight and parallel design shows more pronounced degradation compared to both serpentine designs. The flow field geometry used on the cathode side has strong impact on the long term performance of HT-MEA.

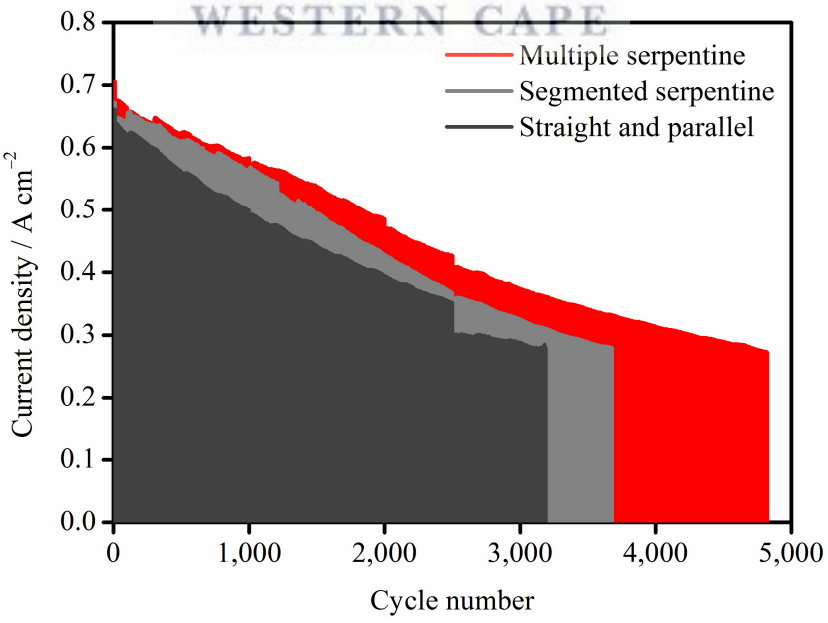

Figure 4-30 Comparisons of evolution of current density over the applied AST with three designs.

The current density profile for multiple serpentine design at 0.5 V initially (first 10 cycles) increases showing a positive effect of cell voltage cycling. This could be attributed to holding the cell potential at 0.5 V (leading to sufficient water and temperature generation) resulting in improved HT-MEA properties or better triple phase conditions. There is a slight drop post shut down after 10 cycles which recovers significantly over next 90 cycles. After the unexpected shutdown at 300 cycles due to fuel gas shortage and subsequent cycling resuming there is a rise in performance followed by gradual degradation in current density until 1000 cycles. Prolonged cycling beyond 1000 cycles to 2500 cycles shows further reduction in current density with a slight irrecoverable drop in current density at 2000 cycles. Post 2,500 cycles there is gradual reduction in current density to 272.4 mA cm^{-2} by EoT (4821 cycles). The cycling effect is clearly observed between 100-4821 cycles.

Potential cycling has a positive effect on fuel cell with segmented serpentine over the first 10 cycles and thereafter the gradual decline in performance with prolonged cycling and severe degradation is observed after 1000 cycles until EoT (3677 cycles). Interruption of potential cycling for characterization studies after 10 cycles showed slight irrecoverable drop in performance. Further interruptions of potential cycling for characterization studieshave little influence on performance loss. Overall, there is no observable loss in first 100 cycles. Again, with increasing number of potential cycles the observed current density at 0.5 V decreases.

Fuel cell with straight and parallel cathode flow field design also shows improved performance during the first 10 cycles then followed by gradual degradation in next 90 cycles. There is severe drop in performance after 100 cycles until 2500 cycles. After 2500 cycles there is a sudden sharp drop of current density and this is due to liquid water accumulation during shut down conditions. The declined performance stabilized over next 700 cycles until EoT (3188 cycles). It should also be noted that when the AST is interrupted for CV and LSV characterization studies after 100, 1000 and 2500 cycles there is some drop in performance because of shut down condition which is recovered to some extent when the potential cycling is resumed in all the cases. But for the cell with straight and parallel design there is a sharp major drop observed after 2500 cycles which is irrecoverable. The adverse effects of cell potential cycling is clearly seen from

Figure 4-30. Fuel cell with multiple serpentine design shows least degradation of 8.98 mA cycle^{-1} compared to other two designs with straight and parallel design showing highest degradation of 11.92 mA cycle^{-1}.

Current density recorded at beginning and end of each set of cycles in the range of 0-10, 10-100, 100-1000, 1000-2500 and 2500-EoT is used to calculate the performance loss associated with each design is represented in Figure 4-31. During the first 10 cycles of AST there is a gain in performance for all the three designs with straight and parallel design showing maximum gain in current density represented with white stripes in Figure 4-31, 0-10 cycle range. The current density gain could be caused by increased concentration of water in the electrolyte in cathode CL [37]. As a result a decrease in membrane resistance at high current densities could be observed due to PA dilution and increased conductivity. At intermediate cell voltages like 0.5 V, high current densities are achieved also resulting in increased water vapor generation which dilutes the PA and improves membrane resistance and ionic conductivity. The reason for increase in current density due to local HT-MEA temperature rise also cannot be eliminated. In the next 90 cycles the HT-MEA with straight and parallel design starts to lose its performance on the contrary segmented serpentine shows stable performance. Multiple serpentine design shows gain in current density over first 100 cycles. The degradation behavior of all the three designs over the entire duration of AST is shown in Figure 4-31. The columns with white patterns indicate gain in performance and columns without white pattern represent loss in performance. After the 100 cycles the performance starts to drop and as a result current density losses appear drastically especially for straight and parallel design by the end of 1000 cycles. As the cycling continue to 2500 cycles segmented serpentine shows huge current density loss. By the EoT the loss of current density decreases for straight and parallel and this is due to fewer number of cycles. It can be said that loss of current density is proportional to number of cycles which is visible from the graph presented in Figure 4-31. It is understood that potential cycling is detrimental to fuel cell catalyst and cycling to OCV must be limited to avoid unnecessary loss of performance. During the AST, current density is lost due to HT-MEA degradation and to identify the causes of degradation characterization studies are performed.

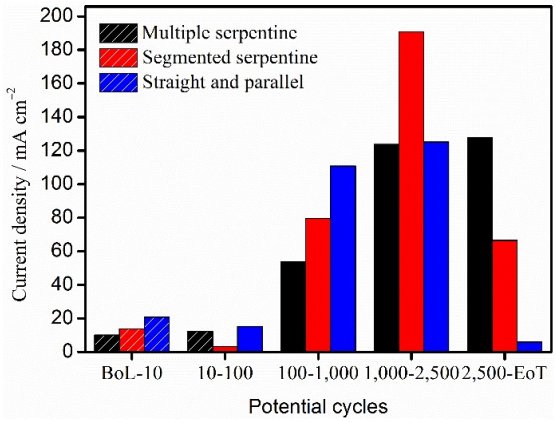

Figure 4-31 Comparisons of current density loss after 10, 100, 1000, 2500 cycles and EoT for three designs after AST.

4.4.1 In-situ characterization

4.4.1.1 Polarisation curves

The polarisation curves are recorded after BoL, 10, 100, 1000, 2500 cycles and EoT of AST period. The performance remains more or less stable over the first 10 hours of cycling with three designs. After prolonged cycling the performance of fuel cell with multiple serpentine, segmented serpentine and straight and parallel tend to decline and accelerated with number of cycles which is presented in Figure 4-32. After 100 cycles of AST, there is significant loss of performance especially for straight and parallel design as shown in Figure 4-32c at 1000 cycles. The I-V curve recorded at 2500 cycles also show severe degradation in performance.

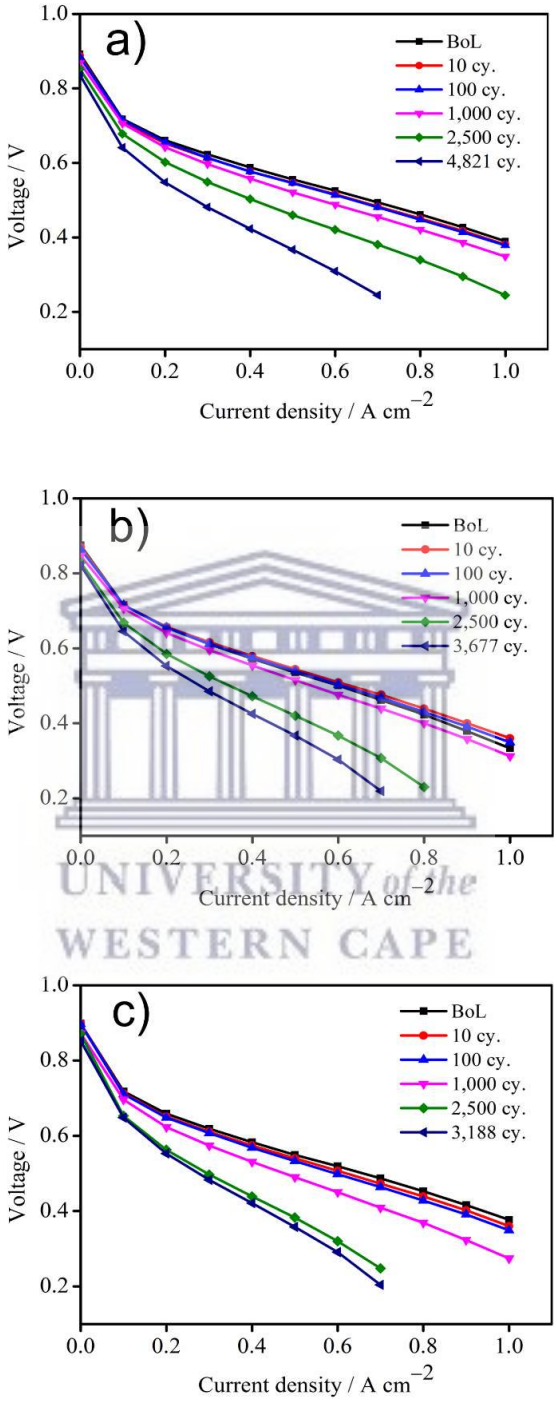

Figure 4-32 Polarisation curves of HT-PEMFC after BoL, 10, 100, 1,000, 2,500 cycles and EoT with a) multiple serpentine, b) segmented serpentine, c) straight and parallel flow field design on cathode side. The number of potential cycles (cy.) are indicated in the figure.

This can be noticed from power density curves from polarisation curve calculated for 0.5 A cm^{-2} at various stages of AST as shown in Figure 4-33. Overall, the activation losses

increase significantly after AST. The voltage decay rates at 0.2, 0.5 and 0.7 A cm^{-2} from polarisation curve were presented in Table 4-7.

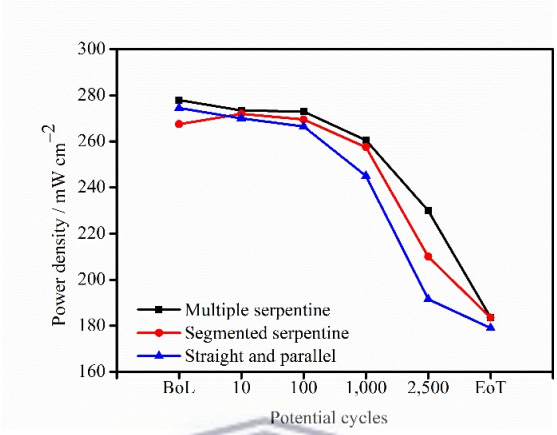

Figure 4-33 Comparison of power density at 0.5 A cm^{-2} for three designs during AST.

The results from polarisation curves are in agreement with the current density profile plotted in Figure 4-30 as a result of AST.

Table 4-7 Summary of current density @0.5 V during AST period and voltage degradation rate at 0.2, 0.5 and 0.7 A cm^{-2} for three flow field designs from polarisation curves.

Design type	AST cycles	Current density @ 0.5 V / mA cm^{-2}		Voltage decay rate / µV $cycle^{-1}$		
		BoL	EoT	0.2 A cm^{-2}	0.5 A cm^{-2}	0.7 A cm^{-2}
Multiple serpentine	4821	705.4	272.4	23.43	39.20	51.64
Segmented serpentine	3677	671.8	279.3	18.76	45.68	66.08
Straight and parallel	3188	660.6	280.3	33.24	59.91	88.77

The Tafel slopes are calculated (not shown here) in the activation region from IR-free voltage curves in the current density range between 0.01 and 0.1 A cm^{-2}. Tafel slope provide information about the kinetics of ORR on cathode electrodes. The activation losses for fuel cells with three designs increased exponentially after 1000 cycles to EoT. The increase in activation losses is due to agglomeration of Pt particles on cathode side under severe potential cycling at high operating temperature [38]. So, prolonged operation of the HT-PEMFC in the region >750 mV should be avoided to extend the life

of fuel cell because this accelerates degradation with a Tafel slopes ranging around 100 to 147 mV per decade which is almost similar to ref. [39].

4.4.1.2 EIS

The voltage losses observed from I-V curves are further analyzed in detail using EIS spectra. The spectra obtained from EIS technique during the AST period are represented as Nyquist plots as shown in Figure 4-34. From the spectra two semi-circle regions can be identified associated with HF and LF. The point where the spectra cross the real axis at high frequency represents R_{ohm} as shown in Figure 4-34a and 34c [3], [15]. Some of the spectra do not show high frequency intercept, instead show capacitive behavior at high frequency as in Figure 4-34b and 34c as in ref. [40]. The details of spectra and associated process are mentioned in section 2.3.2.

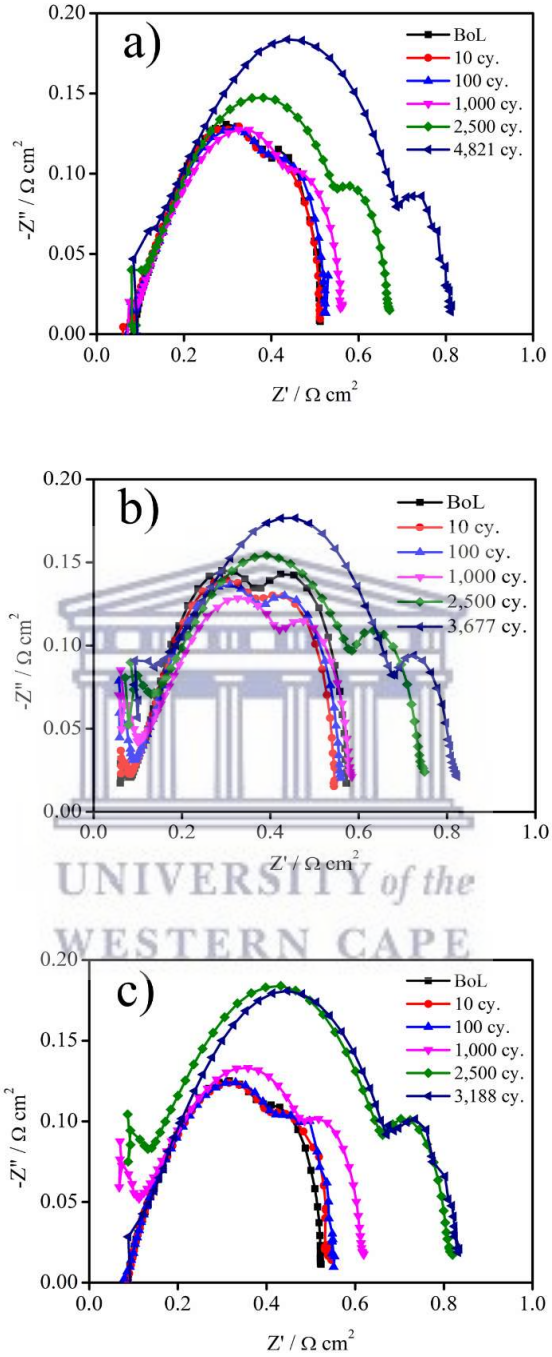

Figure 4-34 EIS spectra of HT-PEMFC obtained at 0.2 A cm^{-2} after BoL, 10, 100, 1,000, 2,500 cycles and EoT with a) multiple serpentine, b) segmented serpentine, c) straight and parallel flow field design on cathode side. The number of potential cycles (cy.) are indicated in the figure.

The extrapolated R_{pol} is combined resistance of cell plotted in Figure 4-35 as a comparison for three designs. The polarisation resistance increases from around 0.5 Ω cm^2 to 0.8 Ω cm^2 for three designs during AST period. The resistance of multiple

serpentine is almost stable during first 100 cycles and increases thereafter with increase in potential cycling. The resistance of segmented serpentine decreases after 10 cycles (in agreement with polarisation curves and Tafel slope) and gradual increase upto 1000 cycles and steep rise thereafter until EoT. The unexpected high resistance for segmented serpentine cell at BoL is possibly because of insufficient activation time or PA adsorption onto catalyst and blocking the GDL resulting in high activation and mass transfer losses. With progressive cycling the PA is redistributed between the various HT-MEA components there by showing a decrease in LF resistance. Unlike the serpentine designs, the resistance of straight and parallel cell shows gradual increase after BoL up to 100 cycles followed by steep rise till EoT. Even though the R_{pol} is almost same with all three designs at EoT, the total number of cycles performed is different with three cells. The cell with straight and parallel design shows high resistance between 100 and 2500 potential cycles showing a strong impact of potential cycling on this type of design.

Membrane resistance remains almost stable during AST with slight variation. During potential cycling operation the water is generated at cathode which could flush the acid out

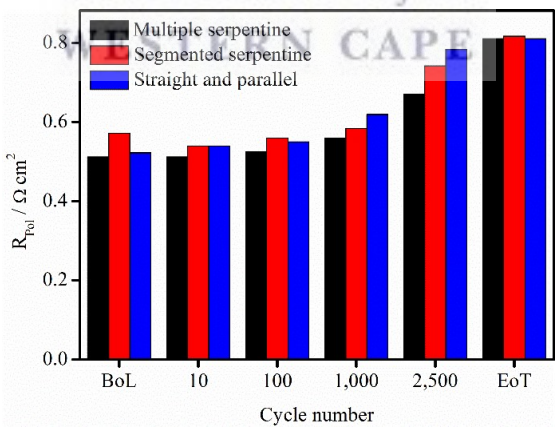

Figure 4-35 Comparison of combined cell resistance from EIS for three designs during AST.

of cell. The high frequency intercept is expected to move slightly towards right by EoT corresponding to decrease in proton conductivity because of acid leaching. The acid loss from membrane is said to have serious effect however cannot be concluded at this point. The availability of phosphoric acid in the catalyst layer causes the high frequency arch to increase [41]. The resistance of membrane is around 0.1 Ω cm^2 depending on

acid content and state of polymer matrix [40]. The cell compression torque also largely affects membrane resistance which is constant during the AST period. In the present scenario the acid leaching is assumed to cause some membrane degradation however hydrogen crossover and internal short circuit are evaluated before making any clear conclusions. The acid loss from PBI membrane causes increase in membrane resistance thereby decreasing the ionic conductivity of electrolyte. The HF semi-circle associated to cathode charge transfer resistance increases throughout the AST test and has high contribution to total resistance R_{pol}. This behavior is observed from spectra in Figure 4-34. The increase in charge transfer resistance might be associated with platinum agglomeration, catalyst support corrosion or electrolyte loss from catalyst layer. All of these mechanisms could possible lead to ECSA loss. The LF semi-circle representing the mass transport resistance does not change much with AST. Higher operating temperatures beyond 160°C have effect on mass transport resistance due to effect of temperature on carbon support corrosion and thereby change of porosity of backing layer/catalyst layer [40]. Apart from this lower stoichiometry on cathode side and severe start-up and shut down cycling contribute to mass transfer losses. The OCV operation also causes carbon support corrosion and thereby increase in mass transport resistance.

4.4.1.3 CV

To quantify ECSA of Pt, CV measurement is performed after BoL, 100, 1000, 2500 cycles and EoT during AST. CV is performed at 5 intervals and 3 measurements every time. The second measurement curve is used for integration of hydrogen desorption/adsorption peaks to evaluate ECSA of Pt. The voltammograms for cells with three designs at BoL and 100, 1000, 2500 and EoT of AST are shown in Figure 4-36.

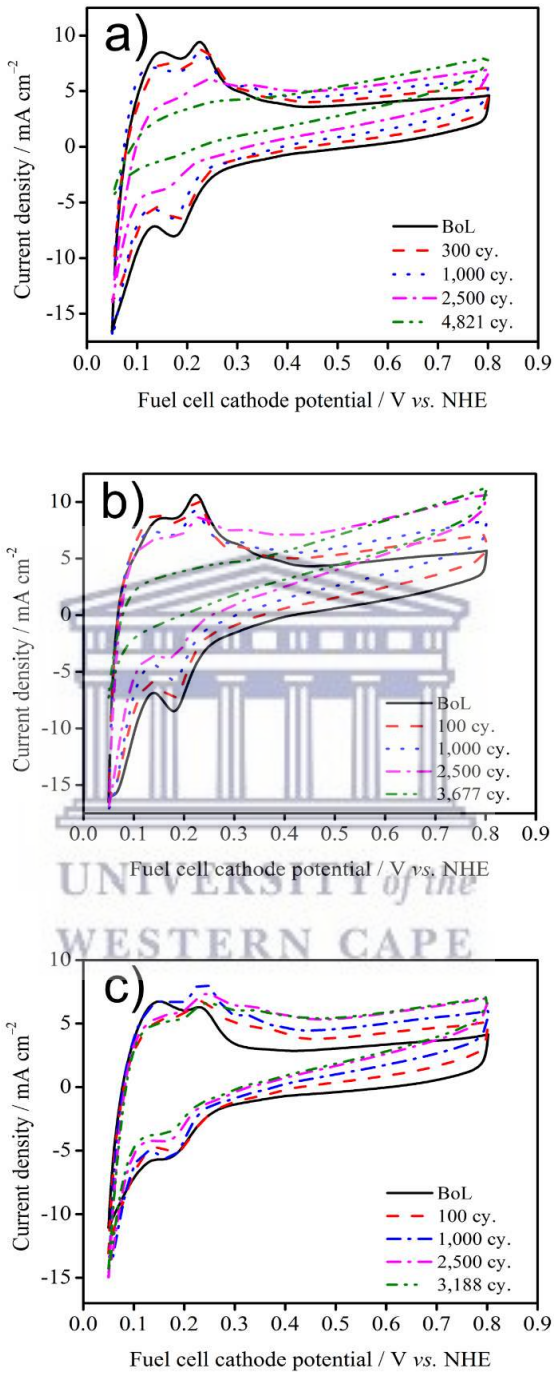

Figure 4-36 CV of HT-PEMFC obtained at room temperature after BoL, 100, 1000, 2500 cycles and EoT with a) multiple serpentine, b) segmented serpentine, c) straight and parallel flow field design on cathode side. The CV for fuel cell with multiple serpentine is recorded after 300 cycles and not after 100 cycles. The number of potential cycles (cy.) are indicated in the figure.

The ECSA responsible for electrochemical reaction decreases with potential cycling as in Figure 4-37. This could be due to Pt crystal growth. The ECSA loss is reported to be a

major degradation observed in ref. [42]. Thinning of catalyst layer, Pt agglomeration and carbon corrosion are some of the mechanisms contributing to catalyst surface area loss. It should be noted that the active area obtained is not real area of HT-MEA but more or less the progress/trend over AST period. The PA in HT-MEA, partially dissociates into PO_4^{3-} anions which strongly adsorb to platinum particles thereby hindering the ORR. The adsorption of anion depends on the HT-MEA voltage and dissociation of acid level. When the potential is swept in CV the adsorption/desorption of anions causes distortion in shape of CV curve as observed by [40] around 0.15-0.2 V.

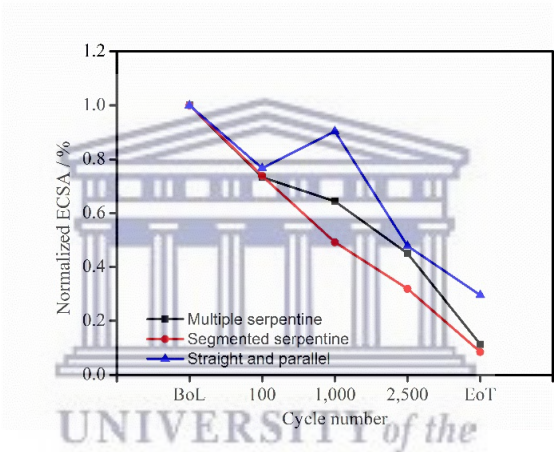

Figure 4-37 Comparison of normalized ECSA for three designs at regular intervals during AST period.

ECSA obtained at BoL are almost close to one reported by Galbiati et al. [40]. After the first 100 potential cycles the ECSA decreases by almost 25 % for segmented serpentine and straight and parallel designs whereas for the multiple serpentine it takes 300 cycles for same ECSA loss. ECSA loss in first week after the AST period is reported in literature. The ECSA loss could be attributed to the removal of loosely bound catalyst nanoparticles from the electrochemical active centers during initial operation of MEA [43]. Thereafter ECSA starts to decrease with a steep drop with increasing number of potential cycles.

4.4.1.4 LSV

The hydrogen crossover through the membrane is measured according to procedure mentioned in section 3.4.1.4. The membrane degradation mechanisms can be studied *via* LSV method. The thinning of membrane would cause hydrogen to escape or pass

through the PBI membrane and mix with air on the cathode side directly without electrochemical reaction resulting in loss of fuel efficiency.

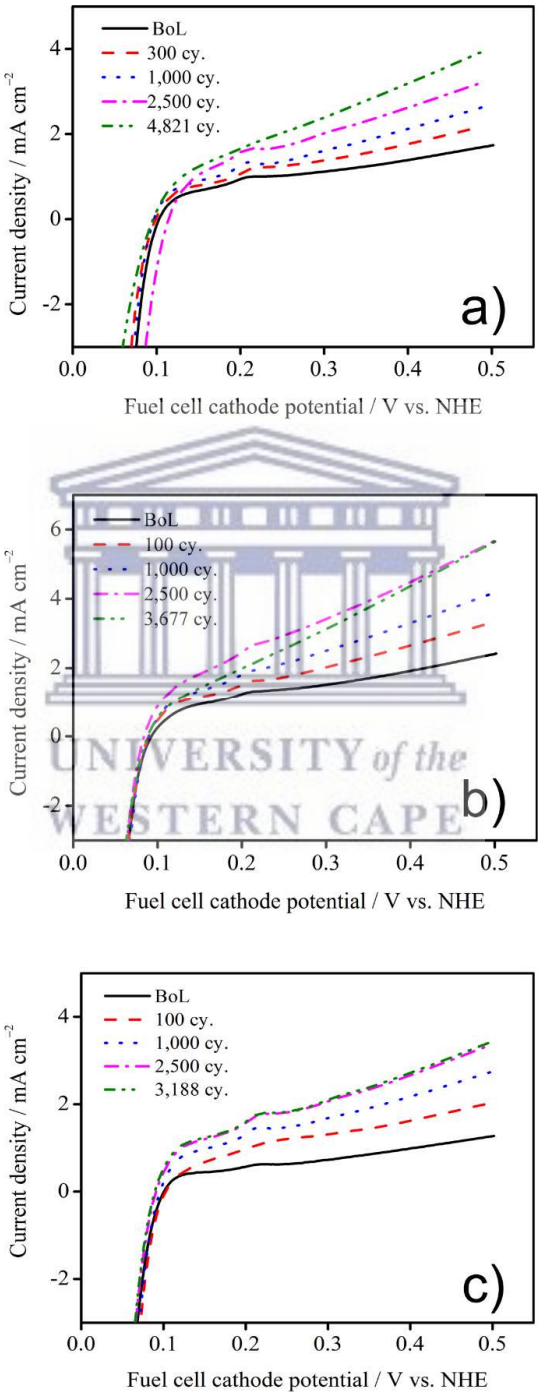

Figure 4-38 LSV of HT-PEMFC obtained after BoL, 100, 1,000, 2,500 cycles and EoT with a) multiple serpentine, b) segmented serpentine, c) straight and parallel flow field design on cathode side. The LSV for fuel cell with multiple serpentine is recorded after 300 cycles and not after 100 cycles.

Thinning or holes is associated with hydrogen crossover and mixed potential thereby decrease in cell OCV and performance losses. The results from LSV measurements are shown in Figure 4-38. The hydrogen crossover flux is calculated from Equation 3-4 of section 3.1.4.1.

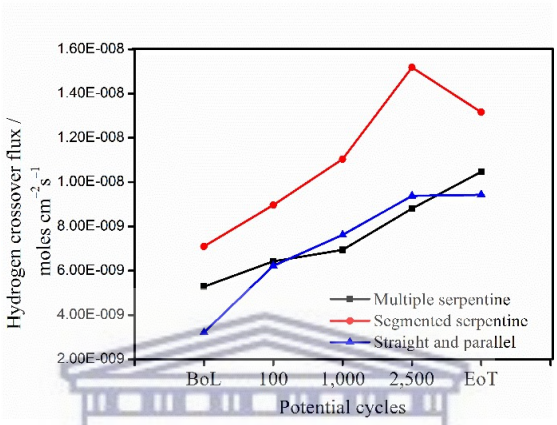

Figure 4-39 Comparison of hydrogen crossover flux for three designs at regular intervals during AST period.

A comparison of hydrogen crossover flux through the membrane is presented in Figure 4-39 for three designs obtained from i_{lim} of LSV curves. The i_{lim} is in the range of 0.62-2 mA cm^{-2} for multiple serpentine and straight and parallel designs. However for the segmented serpentine the crossover current observed is slightly higher from BoL which is 1.37 mA cm^{-2} and increased to 2.93 mA cm^{-2} by the end of 2500 cycles. There could be possibly membrane thinning allowing some hydrogen to pass through. The steady state current related to the hydrogen oxidation is measured as indication of the hydrogen crossover. It is obvious from the LSV curves, that the rate of crossover current increases with increasing potential cycles but within the acceptable range of 1-2 mA cm^{-2} [44]. Potential cycling could possibly result in membrane volume changes. The water generation at lower potentials and absorption by PA or membrane results in membrane swelling and at upper potential limits the water vapor is vented out creating stress on membrane. However, the observed results of hydrogen crossover due to membrane thinning is not considered as a major degradation mechanism considering stable OCV and membrane resistance throughout AST period.

4.4.2 Post-mortem analysis

4.4.2.1 ICP-OES

The water samples on cathode side have been analyzed for PA using ICP-OES. The water vapor from the cathode exhaust is condensed to room temperature and collected for detection of P and Pt to further assist in degradation characterization. Figure 4-40 presents the amount of water collected due to fuel cell reaction at the cathode side and PA calculated from the P analyzed using ICP. The total amount of water collected at the cathode is less than theoretical value which is not shown here. In this context, the water moves from cathode to anode because of concentration driven diffusion of water [45]. It can be noticed from Figure 4-40 that even though the three HT-PEMFCs are operating at same potential cycling conditions the amount of water generated at cathode exhaust is different owing to different operational hours as can be inferred from Table 4-7.

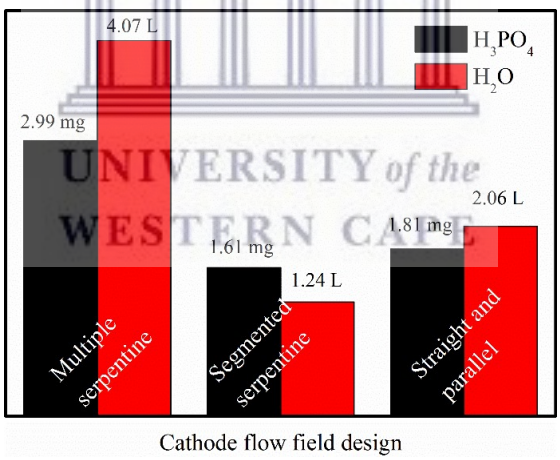

Figure 4-40 Comparison of total water collected from cathode exhaust of fuel cell during AST period for three designs along with PA loss rates.

The huge difference between multiple serpentine and other two designs is also due to water condensing methods or position of water collection bottle used. In case of multiple serpentine design the cathode exhaust was allowed to pass through in-house made condenser to obtain water condensation. The cathode exhaust of segmented and straight and parallel design cells are cooled by the in-built fuel cell test station. The PA leaching from the cathode is significantly higher which is mainly dragged out by product water *via* steam distillation process. 2.99 mg of PA is detected from multiple serpentine design after AST. A high amount of PA is expected at BoL due to redistribution of PA in

HT-MEA during activation period and also squeezing of HT-MEA between plates with applied compression forces results in loss of excess PA. The total amount of PA shown in Figure 4-40 is not the total amount lost from HT-MEA. There might be PA stuck in the gas lines and on the flow field plates. The evaporation and migration of PA in HT-PEMFCs is commonly observed. PBI membranes show electrolyte migration from cathode to anode at high current densities attributed to the high mobility of free hydrogen phosphate anions. The high PA mobility has an effect on electrolyte evaporation as it can influence the PA resupply and saturation of the electrodes and effect on fuel cell performance and life time [46]. PA loss rates may differ depending on the type of operation. Pilinski et al. reported acid loss rates of around 200 ng cm^{-2} h^{-1} under constant load of 0.3 A cm^{-2} for 500 h whereas same author reported 6300 ng cm^{-2} h^{-1} under load cycling conditions between 0.6 and 1.0 A cm^{-2} for 500 h [47]. In the present study PA loss rates of 35-48 ng cm^{-2} h^{-1} are observed and it can be confirmed that the acid loss rates are not major cause for observed performance degradation. The observed values are almost twice obtained by [48].

The concentration of Pt is also analyzed from collected water from cathode exhaust to get more information about platinum degradation and the molarity of Pt is found to be ~9 x 10^{-8} for all three designs. This is very low value suggesting Pt is not lost from fuel cells *via* condensed water because of dissolution [49]. Material characterization studies like TEM and XRD are used to study the reasons for loss in fuel cell performance due to potential cycling.

4.4.2.2 TEM

In order to obtain information about catalyst the TEM images are obtained for scraped catalyst over the anode and cathode of used HT-MEA.

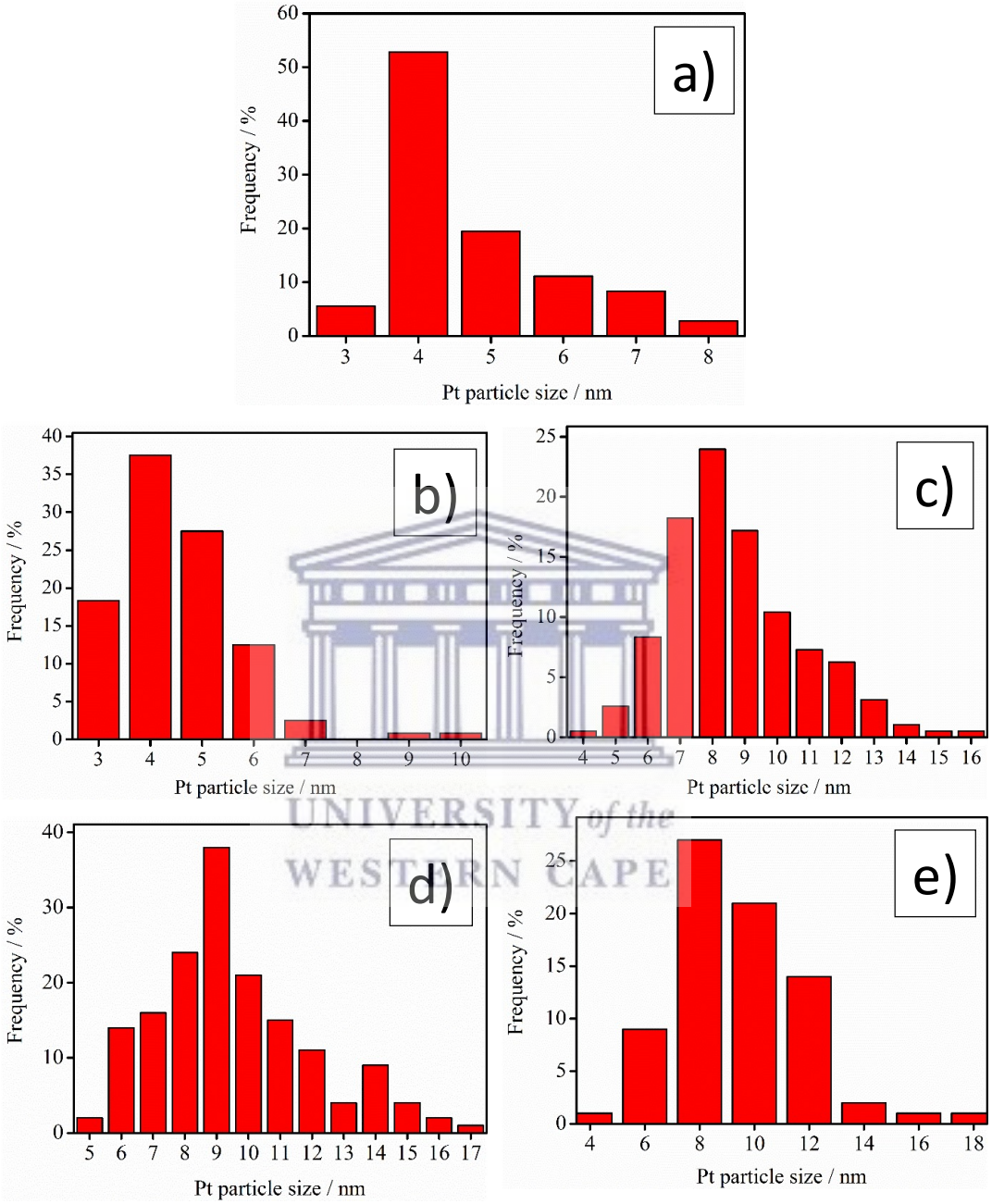

Figure 4-41 TEM Pt particle size distribution for a) fresh and used MEA with b) multiple serpentine anode c) multiple serpentine cathode d) segmented serpentine cathode e) straight and parallel cathode after potential cycling.

Using Image J software application several catalyst particles from these TEM images are processed to obtain particle size distribution. The particle size distribution diagrams for fresh and used MEA with multiple serpentine, segmented serpentine and straight and parallel design on the cathode side are shown in Figure 4-41. The ECSA loss may be

attributed to platinum particle size growth and Pt dissolution into membrane. The mean Pt particle size is 4.1 ± 1.2 nm for a fresh and unused MEA (catalyst) but for the used MEA (catalyst) after potential cycling the values are 8.2 ± 2.0, 9.0 ± 2.4 and 8.3 ± 2.3 nm for multiple serpentine, segmented cathode and straight and parallel design on the cathode respectively. The TEM images also confirm that the anode catalyst is not much affected by the potential cycling with mean Pt particle size (4.0 ± 1.1) remaining same as fresh catalyst (see Figure 4-41a and 42b). The drastic increase of Pt particle size after potential cycling AST has devastating influence on fuel cell performance.

4.4.2.3 XRD

The catalyst is characterized by XRD technique to get detailed understanding about degradation after potential cycling AST. The XRD patterns of degraded catalyst for three designs are shown in Figure 4-42. The Pt (220) diffraction peaks are used to calculate the average crystallite size from Scherrer equation and details of peak positions are given in Table 4-8. The values obtained are within the 0-150 nm validity range for Scherrer equation from FWHM (full width at half maximum).

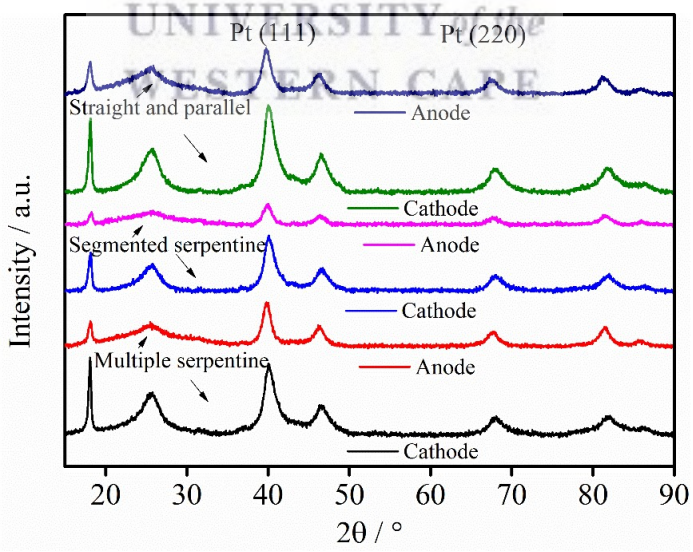

Figure 4-42 XRD of anode and cathode catalyst for MEA with multiple serpentine, segmented serpentine and straight and parallel design after potential cycling.

As it can be observed by comparing the results of both XRD and the HR-TEM images, the calculated crystallite size of the catalyst are larger than those determined from XRD. This is obvious from the fact that XRD provides information on average size of the diffracting

crystals and not particle size. It can be noticed from XRD patterns of cathode, the peaks corresponding to Pt become sharper and grow in size after the AST. This is an evidence of platinum particle growth after the degradation test. Pt particle growth is the major cause for decrease of ECSA.

Table 4-8. XRD data for cathode catalyst after potential cycling AST for MEA with three different cathode flow field designs.

Sample	**Pt (220)**	
	Peak position / 2θ °	Crystallite size (nm)
Multiple serpentine	67.6	6.0
Segmented serpentine	67.6	6.2
Straight and parallel	67.5	5.6

4.4.2.4 SEM

The MEA used for potential cycling test is analysed using SEM. The SEM images of portion of cut piece of MEA of fresh and degraded MEA for segmented serpentine and straight and parallel flow field designs is shown in Figure 4-43.

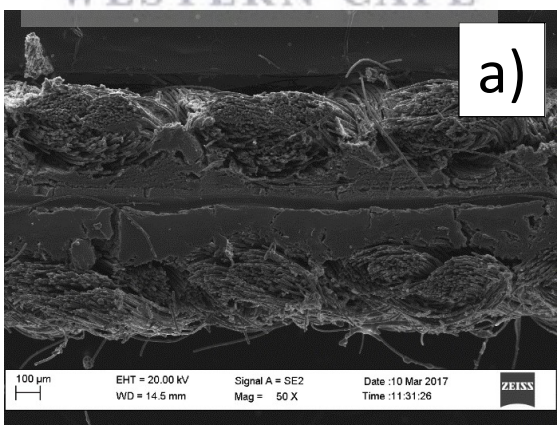

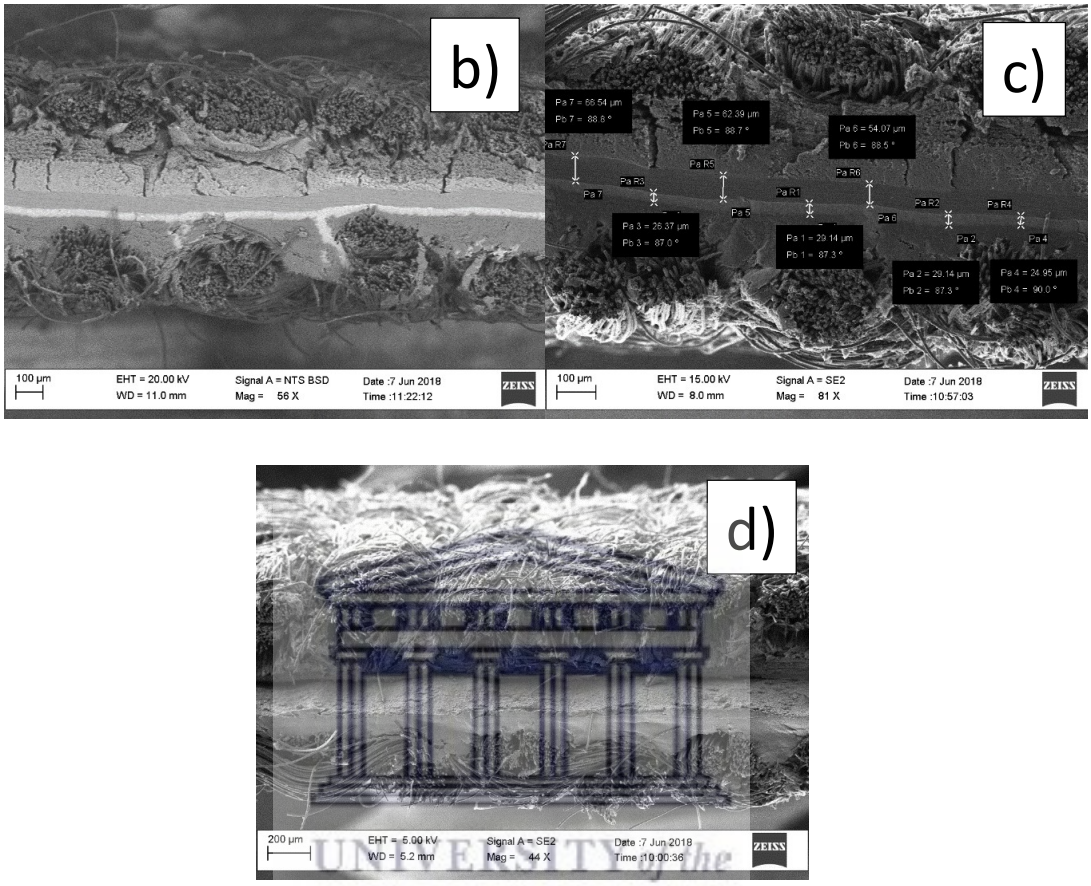

Figure 4-43 SEM images of a) fresh and used MEA with b) and c) segmented serpentine d) straight and parallel on cathode after potential cycling.

The backscattered image of segmented serpentine is shown in Figure 4-43b with all layers identified and thickness of each layer marked in Figure 4-43c. The MEA after the potential cycling test is found to be damaged as delamination of various components of MEA are observed for straight and parallel designs (Figure 4-43d).

Fuel cells experience potential cycling conditions in real time operation scenario. The lower and upper potential limits determine the extent of degradation along with frequency of cycling and wave form applied. In this context, square wave potential cycling is introduced as AST to study factors responsible for HT-MEA performance losses and catalyst degradation. Three HT-PEMFCs are assembled with 96 cm^2 electrode active area using three different cathode flow field designs. An AST testing is performed on assembled fuel cells, with potential cycling between 0.5 V and 0.9 V, 3 min each step, intended for operation of more than 2500 cycles. At 0.5 V potential, the fuel cell

operates producing water from ORR and the Pt surface is reduced from its oxide coverage. At 0.9 V, Pt oxidation and double layer current is generated. Pt oxidation and reduction takes place during each cycle resulting in ECSA loss. Flow field design type used on the cathode side has a strong influence on cell performance and degradation associated with potential cycling. The three cells with different designs lost ~61% of current density at 0.5 V by EoT of potential cycling however the number of cycles performed with multiple serpentine, segmented serpentine and straight and parallel design are 4821, 3677 and 3188 cycles respectively.

During AST testing execution diagnostic techniques are used at regular intervals to observe changes in HT-PEMFC performance. Polarisation curves reveal increasing activation losses with cycling which is also confirmed from Tafel analysis. Severe degradation is observed after 1000 cycles. Limiting current behavior is seen with progressive cycling due to degradation in cathode catalyst layer. The EIS spectra show increasing HF semi-circle with AST related to charge transfer resistance of ORR at cathode. The spectra at low frequency end remained same indicating little contribution from carbon corrosion or mass transport losses to observed performance losses. The membrane resistance is not affected by the potential cycling as the hydrogen crossover of membrane is within the acceptable range and the fact that stable OCV is observed throughout the AST period. PA loss rates from cathode exhaust are calculated and found to be a little or no contribution to observed performance degradation. CV studies show reduction of ECSA by more than 80 % at the EoT in serpentine designs. It is evident from the diagnostic studies that irrespective of design used on the cathode side, the results followed a similar trend but only with straight and parallel degrade quickly compared to multiple serpentine designs. The voltage degradation rates are 39.20, 45.68 and 59.91 $\mu V\ cycle^{-1}$ (from I-V curves at 0.5 A cm^{-2}) for multiple serpentine, segmented serpentine and straight and parallel design respectively.

Based on the study conducted herein potential cycling regime between 0.5 V and 0.9 V is highly detrimental to HT-PEMFC. The ECSA of fuel cell cathode is drastically reduced after AST period due to significant increase in platinum particle growth confirmed from post-mortem results.

4.5 Potential holding test

In this section HT-PEMFC electrode carbon corrosion under AST is studied. Carbon corrosion is influenced by temperature, RH, OCV, cell potential, start stop cycling and also fuel starvation. The influence of OCV and higher cell voltages on carbon corrosion is studied in PA doped PBI based HT-MEA of 96 cm^2 active area using test set-up mentioned in Figure 3-3 with multiple serpentine on anode and cathode according to procedure mentioned in section 3.3.3.

4.5.1 In-situ characterization

The polarisation curves and EIS measurements are performed after each applied potential and moreover during the applied potentials the cathode off-gas is continuously monitored using FT-IR to identify carbon dioxide gas.

4.5.1.1 Polarisation curves

The cell performance is measured after each applied potential stress test to investigate the effect of degradation of carbon support of cathode catalyst layer. The results of polarisation curves after each applied potential of 0.9 V, 1.0 V, 1.1 V and 1.2 V for 30 minutes in comparison to performance at BoL are shown in Figure 4-44. The performance observed at 0.9 V, 1.0 V and 1.1 V is almost similar to BoL performance obtained after the activation.

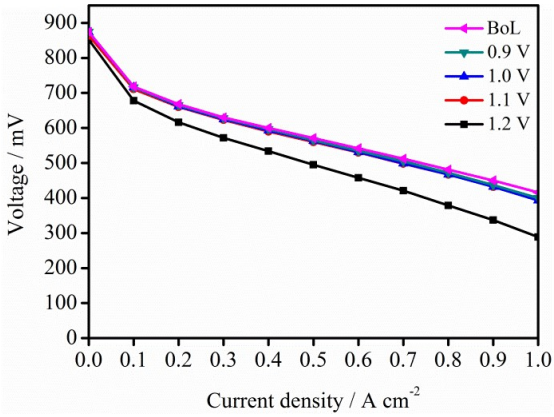

Figure 4-44. Performance curves at 160 °C after applied potential holding AST under non-humidified conditions for 30 minutes at each applied potential.

The performance obtained at 1.2 V has shown significant loss in performance by almost 30 % at 1 A cm^{-2} of current density as shown in Table 4-9 highlights the % of performance loss observed at 0.2 A cm^{-2} and 1 A cm^{-2} compared to BoL performance. This is clear evidence suggesting that high potentials can deteriorate fuel cell performance and can have a significant impact on long term durability. It can be noticed from polarisation curve that OCV is almost the same for all the degradation tests suggesting no changes in membrane resistance.

Table 4-9 Performance loss from polarisation curves at 0.2 A cm^{-2} and 1 A cm^{-2}.

Applied Potential	Voltage @ 0.2 A cm^{-2}	Performance loss / %	Voltage @ 1.0 A cm^{-2}	Performance loss / %
BOL	0.667	0	0.416	100
0.9	0.665	0.3	0.400	3.8
1.0	0.662	0.7	0.393	5.5
1.1	0.660	1.0	0.397	4.5
1.2	0.616	7.6	0.289	30.5

4.5.1.2 EIS

Electrochemical impedance spectroscopy measured before and after the degradation test. The output of EIS is plotted in Figure 4-45. Similar kind of spectra is observed in ref. [18]. Inductive behaviour is not seen at high frequencies instead capacitive behaviour is observed from the impedance spectra. The gold coated pins from impedance measuring equipment are inserted directly on to the graphite bipolar plates. The ohmic resistance at high frequency is a combination of membrane resistance and contact resistance remains almost the same before and after the applied potential stress tests. The increase in size of semicircle suggests that there is significant increase in degradation with increase in applied potential test especially at 1.2 V. The cathode polarisation losses increased with increase in applied potential. The polarisation resistance increased from 0.458 Ω cm^2 after break-in period to 0.527 Ω cm^2 after 1.2 V potential holding test. This suggests that MEA is degraded with applied potential tests.

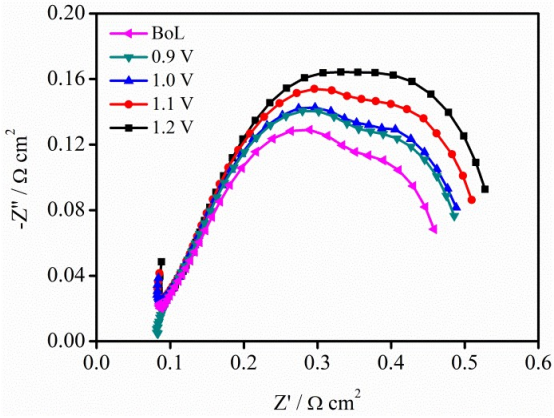

Figure 4-45 EIS spectra before and after the AST with 10 mV perturbation voltage and frequency 10 kHz to 1 Hz.

4.5.1.3 CV

Cyclic voltammograms measured at BoL and after each applied potential are illustrated in Figure 4-46. ECSA of cathode catalyst decreases after the applied potential stress tests. Cathode ECSA decreased by almost 23 % after the applied AST. This is supported from increasing diameter of semicircle of impedance spectra related to charge transfer resistance of fuel cell dominated by cathode losses. The carbon from the catalyst layer degrades when a high potential is applied resulting in agglomeration of platinum particles. Agglomeration raises the charge transfer resistance resulting in performance degradation. The increase in cathode charge transfer resistance means that polarisation losses increase with accelerated degradation test.

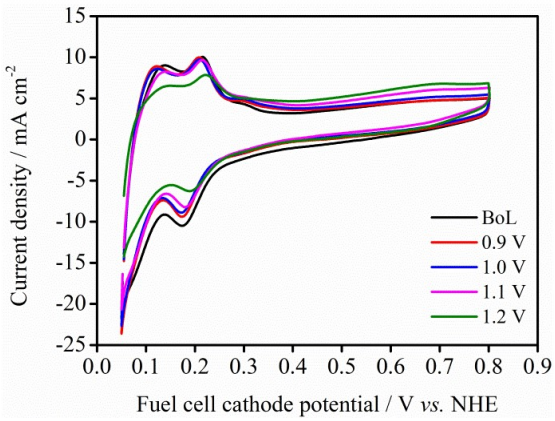

Figure 4-46 Comparison of cyclic voltammograms at BoL and after applied ASTs.

4.5.1.4 Online IR cathode off-gas analysis

Carbon in the cathode catalyst layer is lost as carbon dioxide when the HT-MEA is subjected to AST due to electrochemical oxidation. This is confirmed by monitoring the cathode exhaust using online infra-red spectroscopy. The concentration of carbon dioxide emitted from cathode during the applied potential is seen in Figure 4-47. At 0.9 V the carbon dioxide emitted is insignificant and as the voltage is further increased to 1.0 V there is slight increase in CO_2 concentration. At 1.1 V the CO_2 increases initially and then decreases slowly. At 1.2 V the carbon dioxide shoots up sharply and decreases with time and then steps down when the potential is discontinued at the end of 30 minutes. This is a typical trend observed owing to higher operating potentials and enhanced kinetics of carbon corrosion reaction at higher operating temperature [50]. Also the total amount of carbon dioxide produced after each applied potential is shown in Figure 4-48. It can be clearly seen that highest amount of carbon dioxide is produced after 1.2 V potential test. This explains why high potentials are detrimental to HT-PEMFC and fuel cell in real scenario experiences such conditions during start-up and shut-down stage.

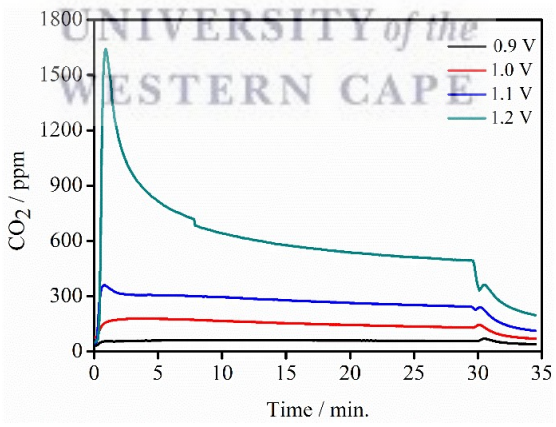

Figure 4-47 Carbon dioxide concentration from NDIR spectroscopy at 0.9 V, 1.0 V, 1.1 V and 1.2 V at 160°C.

This is in line with polarisation curves in Figure 4-44. Even though the carbon dioxide produced at 1.1 V is 5 times higher than that produced at 0.9 V, the performance change is insignificant compared to 0.9 V. This could be due to reversible degradation. With higher applied potentials, CO_2 concentration increases suggesting carbon corrosion of cathode catalyst support.

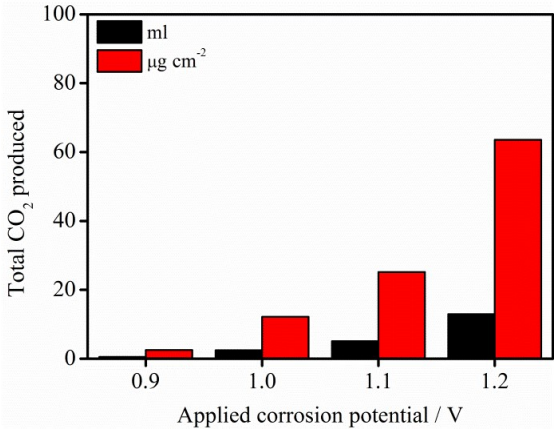

Figure 4-48 Total carbon dioxide V_{CO2} produced and mass of corroded carbon m_{cc} after applied AST.

4.5.2 Effect of relative humidity

The effect of humidifying the reactant gases on carbon corrosion at 1.2 V applied potential is shown in Figure 4-49. Dew point temperature of 60 ° C is maintained at anode and cathode to set 2% humidity. When humidity is added the CO_2 concentration increased by almost 4 times, compared to non humid gases. When water is supplied to fuel cell reactants, functional oxygen groups are generated on the carbon surface which is converted to CO_2. This results in loss of fuel cell performance as seen in Figure 4-50 which compares the performance difference with and without humidification of reactant gases. In reality there can be presence of water in reformate mixture affecting the performance due to carbon corrosion.

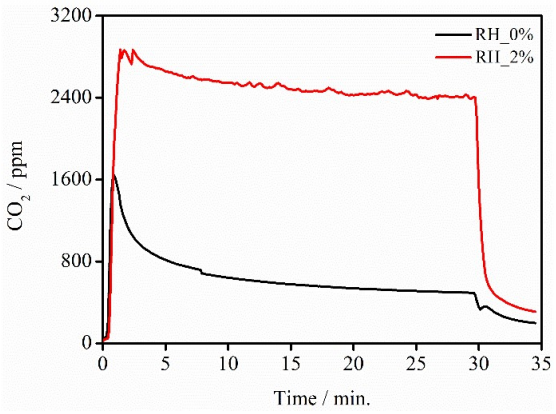

Figure 4-49 Carbon dioxide concentration from NDIR spectroscopy at 1.2 V applied potential with 0% and 2% RH.

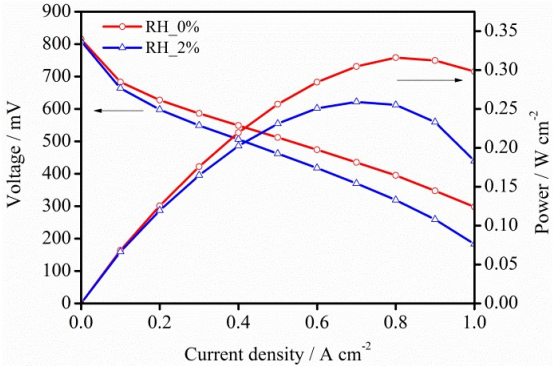

Figure 4-50 Cell performance after the accelerated stress at 1.2 V with 0% and 2% relative humidity.

4.5.3 Post-mortem TEM analysis

The TEM analysis for catalyst from fresh and used MEA is performed to investigate the cause for loss of ECSA. The platinum particle size for cathode catalyst is 3 nm for fresh MEA and 5 nm for degraded MEA. This could be the reason for the loss of ECSA of cathode. The carbon from cathode catalyst layer is lost as carbon dioxide leaving the platinum particles in loss of contact (detachment) and causing decrease in ECSA. The platinum particle size distribution plot before and after the applied potential test is shown in Figure 4-51 for fresh and used MEA.

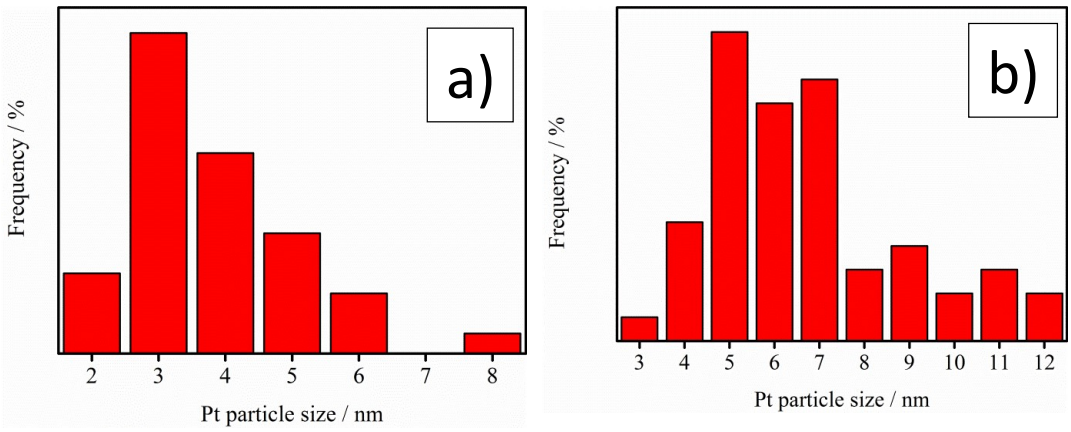

Figure 4-51 Platinum particle size distribution for cathode catalyst a) before and b) after the ASTs.

In summary, the effect of high potentials on cell performance is studied by applying constant high potential for 30 minutes and measuring the degradation. Severe degradation is observed at 1.2 V applied potential confirmed from polarisation curves.

The increase in charge transfer resistance and decrease in the ECSA suggests that the main reason for performance degradation during the applied potential is due to degradation of the carbon support at cathode catalyst layer. The carbon in the catalyst support is electrochemically oxidized to CO_2 causing agglomeration of platinum particles. The presence of CO_2 in cathode exhaust gas is confirmed.

The carbon corrosion is assessed using IR spectroscopy by detecting the carbon dioxide gas in cathode exhaust during 30 minutes operation at AST conditions. 63.55 $\mu g.cm^{-2}$ of carbon is lost as carbon dioxide after the 1.2 V potential test. In-situ performance deterioration is observed using electrochemical methods like polarisation curves, electrochemical impedance spectroscopy (EIS), and cyclic voltammetry (CV). Impedance studies showed no change in membrane resistance whereas cathode polarisation losses increased after the AST. TEM analysis shows that the platinum particle size is increased after the operation at 1.2 V potential test. The ECSA of HT-MEA decreased over the time due to operation at various AST conditions which affected the fuel cell performance. The ECSA decreased from 20.06 to 15.43 $m^2 g^{-1}$ of Pt after the potential holding AST.

References

[1] Y. Rahim, H. Janßen, and W. Lehnert, "Characterizing membrane electrode assemblies for high temperature polymer electrolyte membrane fuel cells using design of experiments," *Int. J. Hydrogen Energy*, vol. 42, no. 2, pp. 1189–1202, 2017.

[2] M. G. Waller, M. R. Walluk, and T. A. Trabold, "Performance of high temperature PEM fuel cell materials. Part 1: Effects of temperature, pressure and anode dilution," *Int. J. Hydrogen Energy*, vol. 41, no. 4, pp. 2944–2954, 2016.

[3] J. Zhang, Y. Tang, C. Song, and J. Zhang, "Polybenzimidazole-membrane-based PEM fuel cell in the temperature range of 120-200^{o} C," *J. Power Sources*, vol. 172, pp. 163–171, 2007.

[4] S. Galbiati, A. Baricci, A. Casalegno, and R. Marchesi, "Sensitivity analysis of a polybenzimidazole-based polymer fuel cell and insight into the effect of humidificatio," *Int. J. energy Res.*, vol. 38, no. 6, pp. 780–790, 2014.

[5] H. Janßen, J. Supra, L. Lüke, W. Lehnert, and D. Stolten, "Development of HT-PEFC stacks in the kW range," *Int. J. Hydrogen Energy*, vol. 38, no. 11, pp. 4705–4713, 2013.

[6] F. Zhou, S. J. Andreasen, S. K. Kær, and D. Yu, "Analysis of accelerated degradation of a HT-PEM fuel cell caused by cell reversal in fuel starvation condition," *Int. J. Hydrogen Energy*, vol. 40, no. 6, pp. 2833–2839, 2015.

[7] F. Zhou, S. Simon Araya, I. Florentina Grigoras, S. Juhl Andreasen, and S. K. Kær, "Performance Degradation Tests of Phosphoric Acid Doped Polybenzimidazole Membrane Based High Temperature Polymer Electrolyte Membrane Fuel Cells," *J. Fuel Cell Sci. Technol.*, vol. 12, no. 2, p. 021002, 2015.

[8] H. Janßen, L. Lüke, W. Lehnert, and D. Stolten, "Setup and experimental validation of a 5 kW HT-PEFC stack," *Int. J. Hydrogen Energy*, vol. 42, no. 16, pp. 11596–

11604, 2017.

[9] R. Radu, N. Zuliani, and R. Taccani, “Design and Experimental Characterization of a High-Temperature Proton Exchange Membrane Fuel Cell Stack,” *J. Fuel Cell Sci. Technol.*, vol. 8, no. 5, p. 051007, 2011.

[10] K. Oh and H. Ju, “Temperature dependence of CO poisoning in high-temperature proton exchange membrane fuel cells with phosphoric acid-doped polybenzimidazole membranes,” *Int. J. Hydrogen Energy*, vol. 40, no. 24, pp. 7743–7753, 2015.

[11] Q. Li, R. He, J. Gao, J. O. Jensen, and N. J. Bjerrum, “The CO Poisoning Effect in PEMFCs Operational at Temperatures up to 200 ° C,” *J. Electrochem. Soc.*, pp. 1599–1605, 2003.

[12] S. Kaserer, K. M. Caldwell, D. E. Ramaker, and C. Roth, “Analyzing the Influence of H 3 PO 4 as Catalyst Poison in High Temperature PEM Fuel Cells Using in-operando X-ray Absorption Spectroscopy,” *J. Phys. Chem. C*, vol. 117, no. 12, pp. 6210–6217, 2013.

[13] G. Elden, M. Çelik, G. Genç, and H. Yapıcı, “The effects of temperature on transport phenomena in phosphoric acid doped polybenzimidazole polymer electrolyte membrane fuel cell,” *Energy*, vol. 103, pp. 772–783, 2016.

[14] D. G. Caglayan, B. Sezgin, Y. Devrim, and I. Eroglu, “Three-dimensional modeling of a high temperature polymer electrolyte membrane fuel cell at different operation temperatures,” *Int. J. Hydrogen Energy*, vol. 41, no. 23, pp. 10060–10070, 2016.

[15] N. H. Jalani *et al.*, “Performance analysis and impedance spectral signatures of high temperature PBI-phosphoric acid gel membrane fuel cells,” *J. Power Sources*, vol. 160, no. 2 SPEC. ISS., pp. 1096–1103, 2006.

[16] J. Hu, H. Zhang, Y. Zhai, G. Liu, J. Hu, and B. Yi, “Performance degradation studies on PBI/H_3PO_4 high temperature PEMFC and one-dimensional numerical analysis,”

Electrochim. Acta, vol. 52, no. 2, pp. 394–401, 2006.

[17] C.-Y. Chen and W.-H. Lai, "Effects of temperature and humidity on the cell performance and resistance of a phosphoric acid doped polybenzimidazole fuel cell," *J. Power Sources*, vol. 195, pp. 7152–7159, 2010.

[18] S. J. Andreasen, J. L. Jespersen, E. Schaltz, and S. K. Kær, "Characterisation and modelling of a high temperature PEM fuel cell stack using electrochemical impedance spectroscopy," *Fuel Cells*, vol. 9, no. 4, pp. 463–473, 2009.

[19] M. Mamlouk and K. Scott, "Analysis of high temperature polymer electrolyte membrane fuel cell electrodes using electrochemical impedance spectroscopy," *Electrochim. Acta*, vol. 56, no. 16, pp. 5493–5512, 2011.

[20] I. A. Schneider, S. A. Freunberger, D. Kramer, A. Wokaun, and G. G. Scherer, "Oscillations in Gas Channels Part I . The Forgotten Player in Impedance Spectroscopy in PEFCs," *J. Electrochem. Soc.*, vol. 154, no. 4, pp. B383–B388, 2007.

[21] S. Authayanun, K. Im-orb, and A. Arpornwichanop, "A review of the development of high temperature proton exchange membrane fuel cells," *Chinese J. Catal.*, vol. 36, no. 4, pp. 473–483, 2015.

[22] Y. Zhu, W. H. Zhu, and B. J. Tatarchuk, "Performance comparison between high temperature and traditional proton exchange membrane fuel cell stacks using electrochemical impedance spectroscopy," *J. Power Sources*, vol. 256, pp. 250–257, 2014.

[23] S. J. Andreasen, J. R. Vang, and S. K. Kær, "High temperature PEM fuel cell performance characterisation with CO and CO_2 using electrochemical impedance spectroscopy," *Int. J. Hydrogen Energy*, vol. 36, no. 16, pp. 9815–9830, 2011.

[24] J. L. Jespersen, E. Schaltz, and S. K. Kær, "Electrochemical characterization of a polybenzimidazole-based high temperature proton exchange membrane unit cell," *J. Power Sources*, vol. 191, no. 2, pp. 289–296, 2009.

[25] W. Lehnert, K. Wippermann, C. Wannek, and D. Stolten, "Cell Resistances of

ABPBI-Based HT-PEFC-MEAs: Time De-pendence and Influence of Operating Parameters," *World Hydrog. Energy Conf.*, vol. 78, 2010.

[26] K. Wippermann, C. Wannek, H.-F. Oetjen, J. Mergel, and W. Lehnert, "Cell resistances of poly (2,5-benzimidazole) -based high temperature polymer membrane fuel cell membrane electrode assemblies : Time dependence and influence of operating parameters," *J. Power Sources*, vol. 195, pp. 2806–2809, 2010.

[27] M. K. Daletou, M. Geormezi, E. Vogli, G. A. Voyiatzis, and S. G. Neophytides, "The interaction of H_3PO_4 and steam with PBI and TPS polymeric membranes. A TGA and Raman study," *J. Mater. Chem. A*, vol. 2, pp. 1117–1127, 2014.

[28] A. Schenk, "Platinum-cobalt catalysts for the oxygen reduction reaction in high temperature proton exchange membrane fuel cells- Long term behavior under ex-situ and in-situ conditions," *J. Power Sources*, vol. 266, pp. 313–322, 2014.

[29] J. Hu, H. Zhang, Y. Zhai, G. Liu, and B. Yi, "500 h Continuous aging life test on PBI/H_3PO_4 high-temperature PEMFC," *Int. J. Hydrogen Energy*, vol. 31, no. 13, pp. 1855–1862, 2006.

[30] Y. Zhai, H. Zhang, D. Xing, and Z. G. Shao, "The stability of Pt/C catalyst in H_3PO_4/PBI PEMFC during high temperature life test," *J. Power Sources*, vol. 164, pp. 126–133, 2007.

[31] R. Kerr *et al.*, "Lifetime and degradation of high temperature PEM membrane electrode assemblies," *Int. J. Hydrogen Energy*, vol. 40, no. 46, pp. 16860–16866, 2015.

[32] G. Liu, H. Zhang, J. Hu, Y. Zhai, D. Xu, and Z. gang Shao, "Studies of performance degradation of a high temperature PEMFC based on H_3PO_4-doped PBI," *J. Power Sources*, vol. 162, no. 1, pp. 547–552, 2006.

[33] C. Siegel, G. Bandlamudi, and A. Heinzel, "Modeling Polybenzimidazole / Phosphoric Acid Membrane Behaviour in a HTPEM Fuel Cell," *Comsol Conf.*, 2008.

[34] C. Siegel, G. Bandlamudi, and A. Heinzel, “Systematic characterization of a PBI/H_3PO_4 sol-gel membrane - Modeling and simulation,” *J. Power Sources*, vol. 196, no. 5, pp. 2735–2749, 2011.

[35] G. Bandlamudi, C. Siegel, C. Heßke, and A. Heinzel, “Fluid Flow and Current Density Distribution in Large-Area HT PEMFCs,” *Comsol*, 2011.

[36] C. Siegel, G. Bandlamudi, N. Van Der Schoot, and A. Heinzel, “Large Scale 3D Flow Distribution Analysis in HTPEM Fuel Cells,” *Excerpt from Proc. COMSOL Conf. 2009*, no. 1, 2009.

[37] A. D. Modestov, M. R. Tarasevich, V. Y. Filimonov, and N. M. Zagudaeva, “Degradation of high temperature MEA with PBI-H_3PO_4 membrane in a life test,” *Electrochim. Acta*, vol. 54, no. 27, pp. 7121–7127, 2009.

[38] J. Kim, M. Kim, B. G. Lee, and Y. J. Sohn, “Durability of high temperature polymer electrolyte membrane fuel cells in daily based start/stop operation mode using reformed gas,” *Int. J. Hydrogen Energy*, vol. 40, no. 24, pp. 7769–7776, 2015.

[39] A. Kannan, J. Kaczerowski, A. Kabza, and J. Scholta, “Operation Strategies Based on Carbon Corrosion and Lifetime Investigations for High Temperature Polymer Electrolyte Membrane Fuel Cell Stacks,” *Fuel Cells*, no. 0, pp. 1–12, 2018.

[40] S. Galbiati, A. Baricci, A. Casalegno, and R. Marchesi, “Degradation in phosphoric acid doped polymer fuel cells: A 6000 h parametric investigation,” *Int. J. Hydrogen Energy*, vol. 38, no. 15, pp. 6469–6480, 2013.

[41] J. R. Kim, J. S. Yi, and T. W. Song, “Investigation of degradation mechanisms of a high-temperature polymer-electrolyte-membrane fuel cell stack by electrochemical impedance spectroscopy,” *J. Power Sources*, vol. 220, pp. 54–64, 2012.

[42] T. Søndergaard *et al.*, “Catalyst Degradation Under Potential Cycling as an Accelerated Stress Test for PBI-Based High-Temperature PEM Fuel Cells — Effect of Humidification,” *Electrocatalysis*, vol. 9, no. 3, pp. 302–313, 2017.

[43] D. Schonvogel, M. Rastedt, P. Wagner, M. Wark, and A. Dyck, “Impact of Accelerated Stress Tests on High Temperature PEMFC Degradation,” *Fuel Cells*, vol. 16, no. 4, pp. 480–489, 2016.

[44] C. Wang *et al.*, “Recent progress on the key materials and components for proton exchange membrane fuel cells in vehicle applications,” *Energies*, vol. 9, no. 603, pp. 1–39, 2016.

[45] F. Javier Pinar, M. Rastedt, N. Pilinski, and P. Wagner, “Effect of idling temperature on high temperature polymer electrolyte membrane fuel cell degradation under simulated start/stop cycling conditions,” *Int. J. Hydrogen Energy*, vol. 41, no. 42, pp. 19463–19474, 2016.

[46] S. H. Eberhardt, T. Lochner, F. N. Büchi, and T. J. Schmidt, “Correlating Electrolyte Inventory and Lifetime of HT-PEFC by Accelerated Stress Testing,” *J. Electrochem. Soc.*, vol. 162, no. 12, pp. F1367–F1372, 2015.

[47] N. Pilinski, M. Rastedt, and P. Wagner, “Investigation of phosphoric acid distribution in PBI based HT-PEM fuel cells,” *ECS Trans.*, vol. 69, no. 17, pp. 323–335, 2015.

[48] S. Yu, L. Xiao, and B. C. Benicewicz, “Durability studies of PBI-based high temperature PEMFCs,” *Fuel Cells*, vol. 8, no. 3–4, pp. 165–174, 2008.

[49] M. Uchimura, S. Sugawara, Y. Suzuki, J. Zhang, and S. S. Kocha, “Electrocatalyst Durability under Simulated Automotive Drive Cycles,” *ECS Trans.*, vol. 16, no. 2, pp. 225–234, 2008.

[50] H.-S. Oh, J.-H. Lee, and H. Kim, “Electrochemical carbon corrosion in high temperature proton exchange membrane fuel cells,” *Int. J. Hydrogen Energy*, vol. 37, no. 14, pp. 10844–10849, 2012.

5 Conclusions

The durability and degradation mechanisms of phosphoric acid doped PBI based HT-PEMFC are studied. Steady-state operation and potential cycling tests are performed to assess the stability of HT-PEM fuel cell with three different cathode flow field designs. Additionally, the effect of potential holding on fuel cell performance is evaluated. The HT-PEMFC is characterized using I-V curves, EIS, CV and LSV. The cell performance deterioration mechanisms as a result of steady-state and AST conditions are investigated based on the chronological changes in the cell performance, internal resistance and structural changes using TEM, SEM and XRD techniques.

5.1 Conclusion

The aim of this work is to investigate the influence of three different cathode flow field designs on the performance, long term stability and degradation mechanisms of BASF Celtec®-P2100 HT-PEM fuel cell of 96 cm^2 geometrical active area. The flow fields under investigation are the multiple serpentine, segmented serpentine and straight and parallel design.

- The effect of anode and cathode stoichiometry along with the influence of operating temperature on the performance of fuel cell with multiple serpentine on anode and cathode is investigated. Increasing the anode stoichiometry (1 to 2.0) has negligible influence on the performance of fuel cell with only slight change at higher current densities > 0.9 A cm^{-2}. The cathode stoichiometry (2 to 5) has significant effect on polarisation curves. The effect is more pronounced from current densities > 0.4 A cm^{-2}. However, the cathode stoichiometry has little influence with current densities < 0.2 A cm^{-2}. Increasing the cathode air stoichiometry increase the oxygen partial pressure causing improvements in thermodynamics and kinetics of fuel cell reactions. The temperature (130 to 160^oC) has positive effect on performance and power density and this is due to the ionic conductivity of the phosphoric acid doped PBI membrane is a function of temperature. The higher operating temperature of the fuel cell leads to larger

exchange current density which in turn reduces the activation losses. An increase in temperature is expected to reduce the activation and mass transport losses through an increase in catalytic activity.

- The current study highlights the use of straight and parallel design on cathode flow plate to achieve performance on par with multiple serpentine design and possibly operation with low pressure drop and uniform current distribution. Even though the degradation rates achieved in this study are quite high compared to literature the continuous (without shut-down) and uninterrupted (limited characterization studies) operation at slightly high reactant stoichiometry will guarantee low degradation rates with multiple serpentine and straight and parallel designs. This work will help to design and develop flow fields for enhanced performance of HT-PEMFC over long term operation. Under tested conditions the straight and parallel design can be used as an alternative to serpentine designs to achieve better performance over long term operation possibly with low pressure drop and uniform current distribution. The charge transfer resistance and performance losses increase within 500 h of operation time. The results of long term stability tests confirm that the cathode side flow-field layout is one major optimization parameter in order to increase the performance and equally distribute the oxygen and maintain uniform current density distribution (gradient).
- The square wave potential cycling is introduced as AST to study factors responsible for HT-MEA performance losses and catalyst degradation. In reality, fuel cells experience potential cycling conditions in real time operation scenario. The lower and upper potential limits determine the extent of degradation along with frequency of cycling and wave form applied. The potential cycling between 0.5 V and 0.9 V with 3 min each step, intended for operation of more than 2500 cycles is performed on fuel cell with three different cathode flow field designs. Flow field design type used on the cathode side has a strong influence on fuel cell performance and degradation associated with potential cycling. The three cells with different designs lost ~61% of current density at 0.5 V by EoT of potential cycling however the number of cycles performed with multiple serpentine, segmented serpentine and straight and parallel design are 4821, 3677 and 3188

cycles respectively. The I-V curves reveal increasing activation losses with cycling. Severe degradation is observed after 1000 cycles. Limiting current behavior is seen with progressive cycling due to degradation in cathode catalyst layer. The EIS spectra show increasing charge transfer resistance of ORR at cathode. The membrane resistance is not affected by the potential cycling as the hydrogen crossover of membrane is within the acceptable range and the fact that stable OCV is observed throughout the AST period. PA loss rates from cathode exhaust are calculated and found to be a little or no contribution to observed performance degradation. CV studies show reduction of ECSA by more than 80 % at the EoT in serpentine designs. It is evident from the diagnostic studies that irrespective of design used on the cathode side, the results followed a similar trend but only with straight and parallel degrade quickly compared to both serpentine designs. The voltage degradation rates are 39.20, 45.68 and 59.91 µV cycle^{-1} (based on I-V curves at 0.5 A cm^{-2}) for multiple serpentine, segmented serpentine and straight and parallel design respectively.

- The effect of high potentials on cell performance is studied by applying constant potentials 0.9, 1.0, 1.1 and 1.2 V for 30 minutes and measuring the degradation. Severe degradation is observed at 1.2 V applied potential confirmed from polarisation curves. The increase in charge transfer resistance and decrease in the ECSA suggests that the main reason for performance degradation during the applied potential is due to degradation of the carbon support at cathode catalyst layer. The carbon in the catalyst support is electrochemically oxidized to CO_2 causing agglomeration of platinum particles. The presence of CO_2 in cathode exhaust gas is confirmation of the carbon corrosion assessed using FT-IR by detecting the CO_2 in cathode exhaust during 30 minutes operation at AST conditions. 63.55 µg.cm^{-2} of carbon is lost as carbon dioxide after the 1.2 V potential test. Impedance studies showed no change in membrane resistance whereas cathode polarisation losses increased after the AST. TEM analysis shows that the platinum particle size is increased after the operation at 1.2 V potential test. The ECSA decreased from 20.06 to 15.43 m^2 g^{-1} of Pt after the potential holding AST.

The ECSA in this studies is much lower than that observed for Nafion® based fuel cells. The catalyst in HT-PEMFC is affected by the strong adsorption of PO_4^{3-} anions onto the active sites of catalysts in phosphoric acid and this is responsible for the observed lower ECSA of phosphoric acid doped PBI based HT-PEMFC. The diffraction peaks of Pt (220) for MEA operated under long term stability and potential cycling AST grow sharper compared to broad peaks for fresh MEA. This behaviour is more pronounced on cathode than on anode suggesting that the cathode is more affected under investigated test conditions and major cause for loss of ECSA.

Overall it can be concluded that straight parallel designs can be used as alternative to serpentine designs when better performance is required under steady-state conditions and under potential cycling conditions multiple serpentine design is favoured.

5.2 Future work

Flow field design play major role in distribution of reactants and products on the surface of electrode and overall performance of the fuel cell. When scaled up to stack level and for commercial application the flow field design factor plays crucial role in heat dissipation, product water removal and minimised parasitic losses from BoP and lower pressure drop. It would be interesting to study the current density distribution maps of each flow field design at different current densities and reactant flow rates. Also the results obtained can be used to compare with computer simulation of flow fields under similar operating conditions.

Appendix

A-1 Properties of Schunk Grade FU 4369HT for HT-PEMFC.

Application	Standard grade for machined prototype and molded plates HT-PEM
Heat Deflection Temperature	210°C
Glass Transition Temperature	190°C
Hardness HRB10/40	100
Flexural Strength	40 MPa
Density	1.90 g cm^{-3}
Water Absorption	0.15 %
Minimum Web Thickness	0.9 mm
Thermal Conductivity	55 w $m^{-1}K^{-1}$

A-2 Design specifications of multiple serpentine flow field geometry.

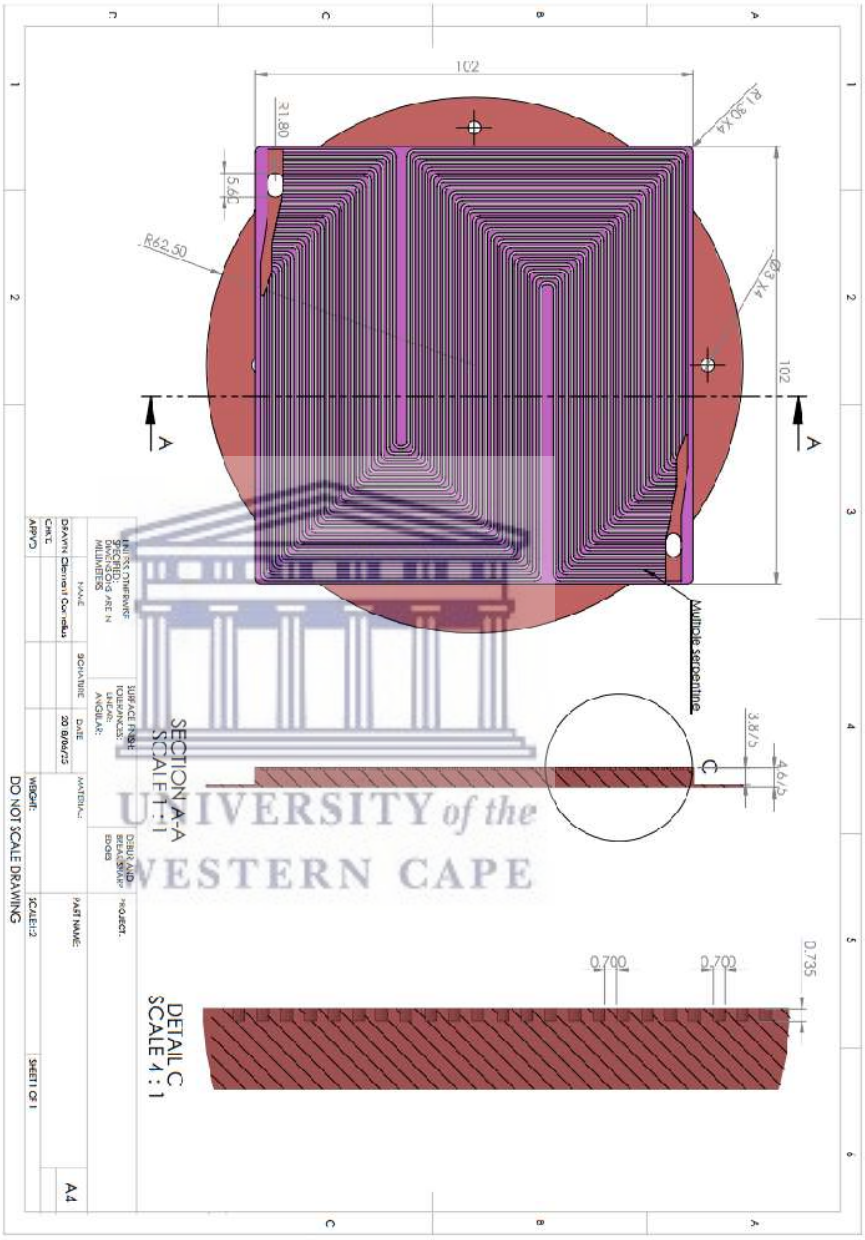

A-3 Design specifications of segmented serpentine flow field geometry.

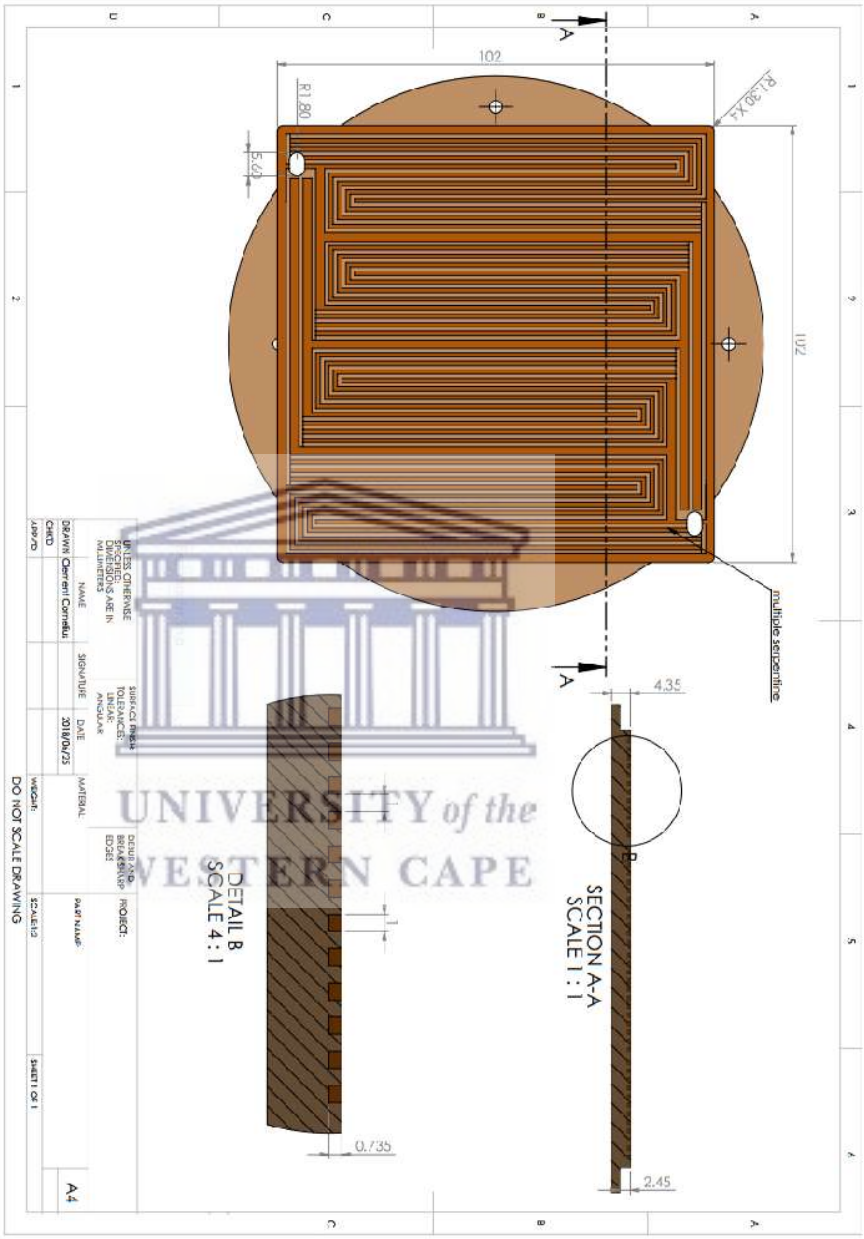

A-4 Design specifications of straight and parallel flow field geometry.

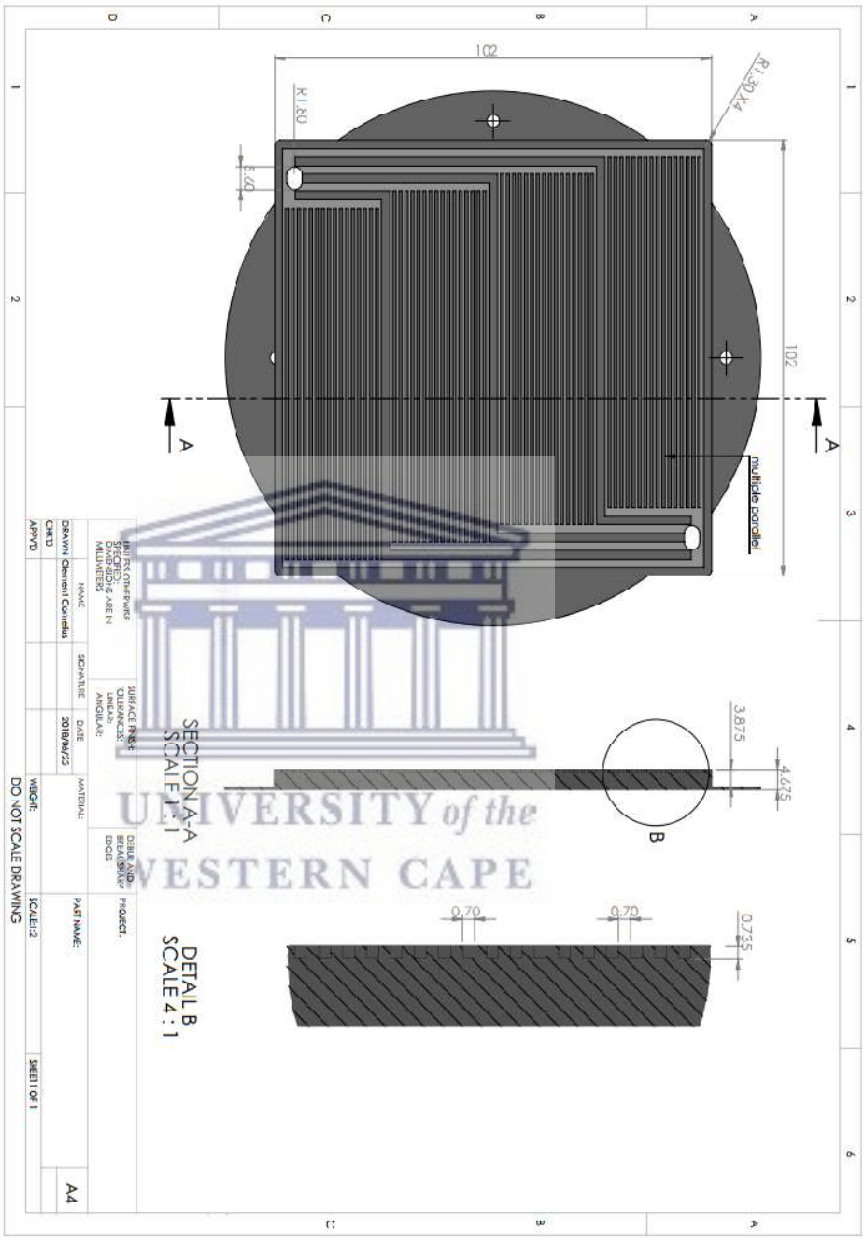

A-5 Flow chart showing the start-up procedure of PBI based HT-PEMFC.

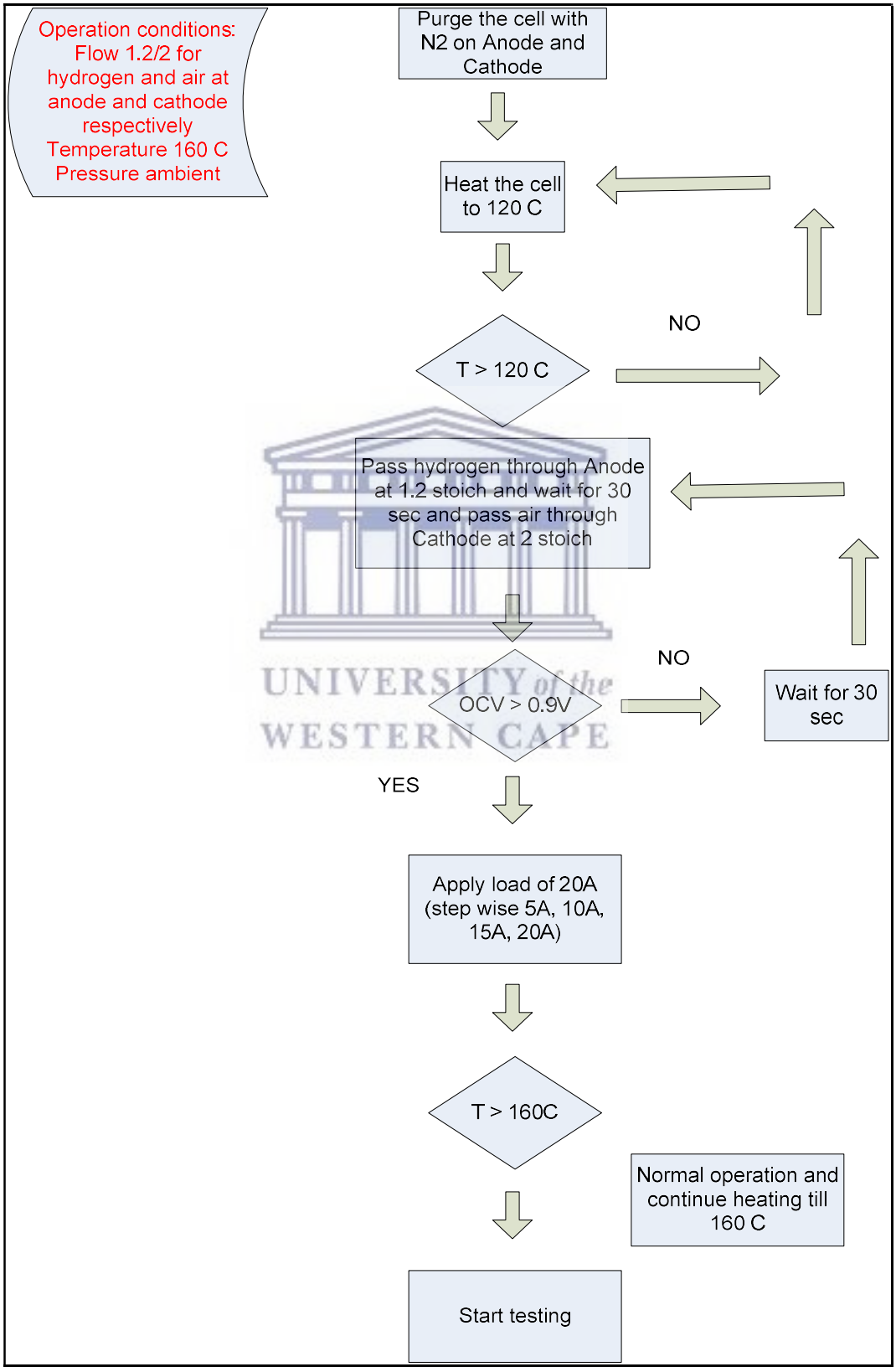

A-6 Flow chart showing the potential cycling test procedure and conditions.

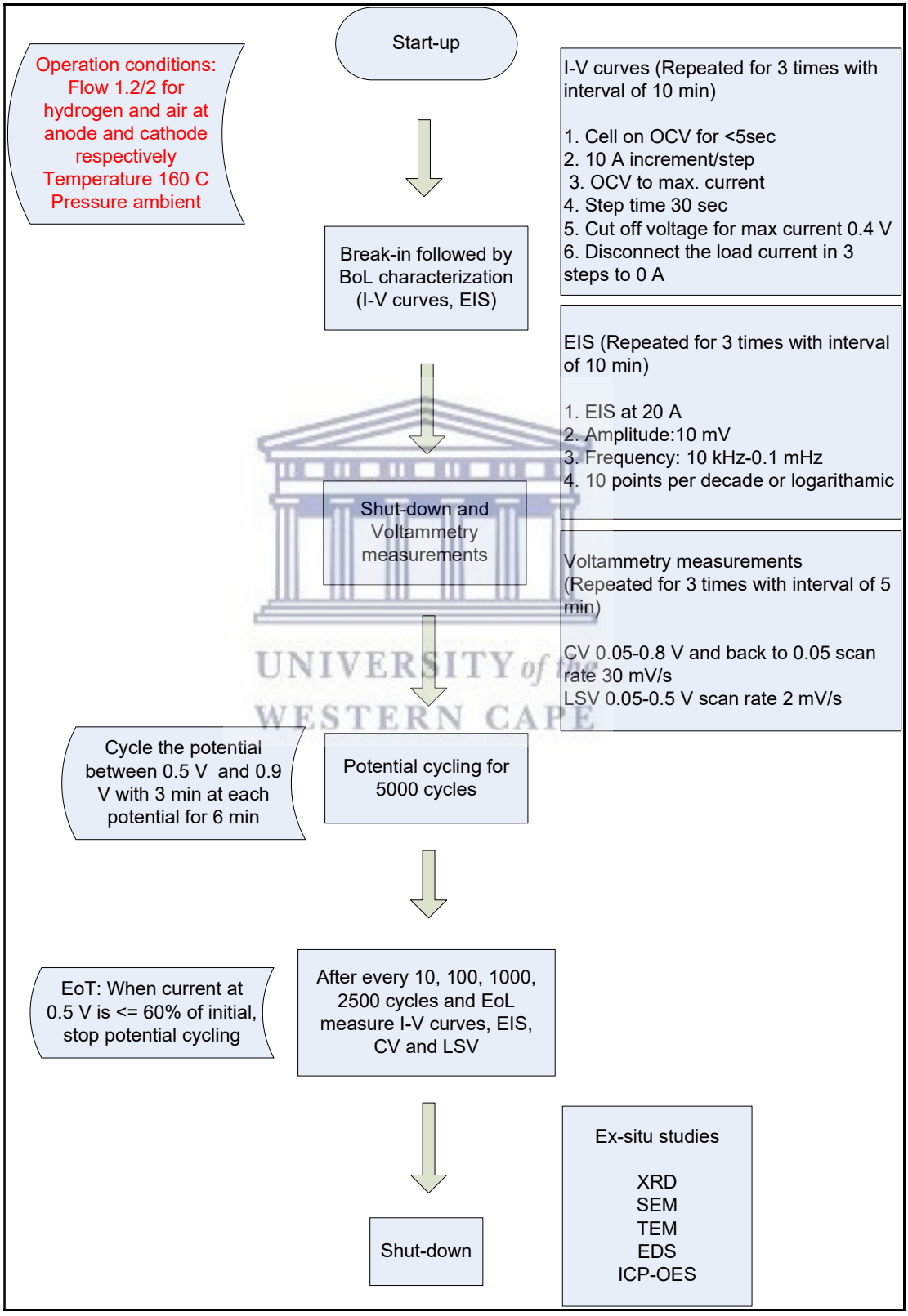

A-7 Flow chart showing the potential hold test procedure and operational conditions.

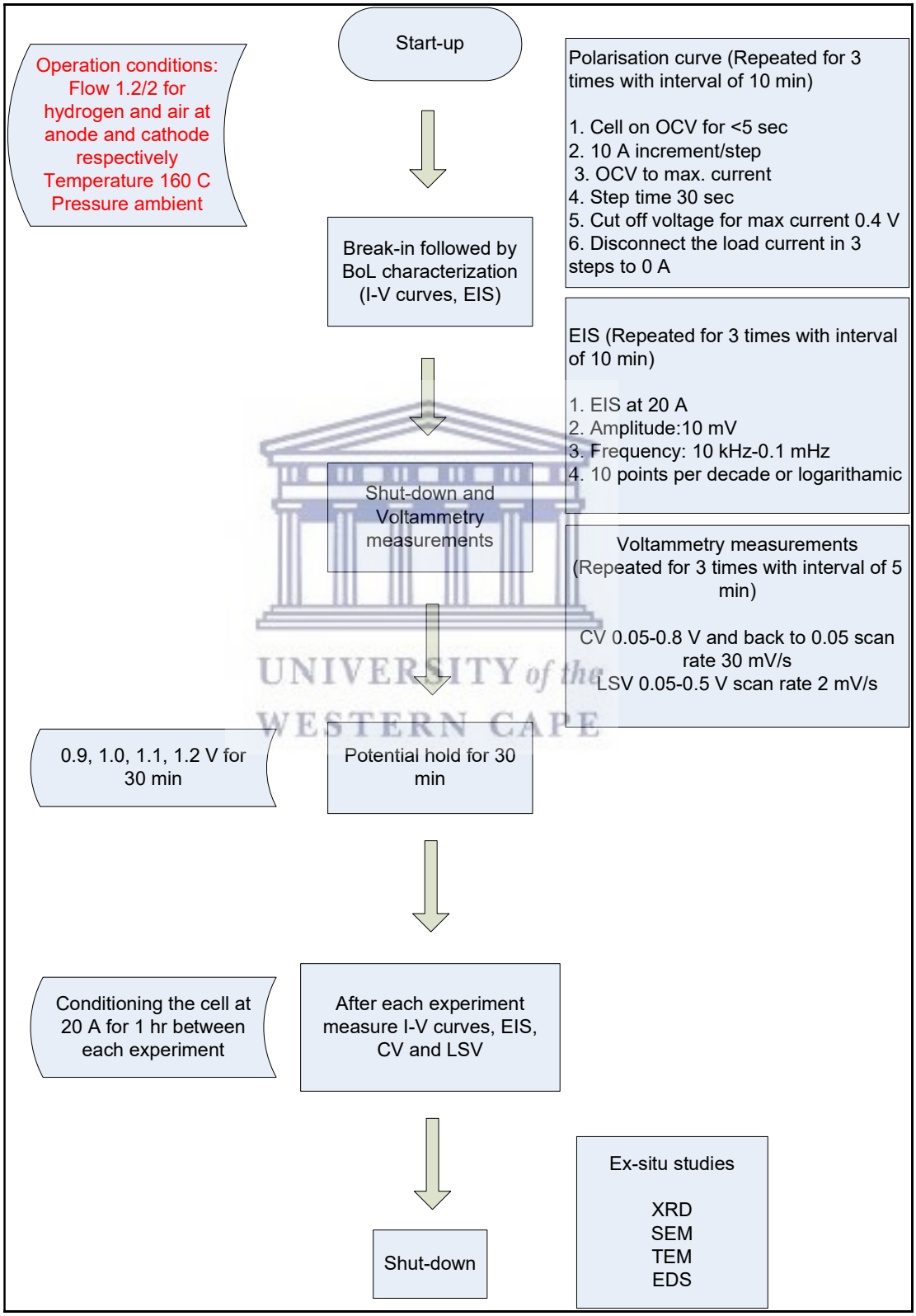

Publications list

Conference presentations

1. **Effect of Accelerated Stress Testing on High Temperature Proton Exchange Membrane Fuel Cell,** 232nd ECS Meeting, National Harbour, MD, USA, October 4th 2017.
2. **Study on Electrode Carbon Corrosion of High Temperature Proton Exchange Membrane Fuel Cell,** 1st Africa Energy Materials Conference, CSIR International Conventional Centre, Pretoria, South Africa, March 21st 2017.

Poster presentations

1. **The performance and lon-term stability of High Temperature PEM fuel cells,** 30TH IPHE Steering committee Meeting Dec 4-7, 2018, Pretoria, South Africa.
2. **Characterization of HT-PEMFCs with Three Different Flow Field Designs**, Technical University of Graz, Austria, August 31st , 2016.

Articles

1. V. Bandlamudi, P. Bujlo, C. Sita, S. Pasupathi, Study on Electrode Carbon Corrosion of High Temperature Proton Exchange Membrane Fuel Cell, **Materials Today: Proceedings 5 (2018) 10602–10610.**
2. The Effect of Potential Cycling on High Temperature PEM Fuel Cells with Different Flow Field Designs **(draft submitted to FuelCells Journal).**